Prediction of tissue outcome after experimental stroke using MRI-based algorithms

Mark J.R.J. Bouts

Colophon

Design & Lay-out: Mark Bouts
Printed by: Print service Ede B.V.

Bouts, M.J.R.J.
Prediction of tissue outcome after experimental stroke using MRI-based algorithms

PhD thesis, Utrecht University - met een samenvatting in het Nederlands
ISBN: 978-90-393-5955-6

The research described in this thesis was conducted at the Department of Biomedical Imaging and Spectroscopy (BMRIS) of the Image Sciences Institute (ISI), University Medical Center Utrecht (Utrecht, The Netherlands). The research in this thesis was supported by the Netherlands Heart Foundation (2005B156), the European Union's Seventh Framework Programme (FP7/2007-2013) under grant agreements n° 201024 and n° 202213 (European Stroke Network), the National Institutes of Health (R01NS041285, R01NS59775, R012NS063925, NCRR [P41RR14075]), the American Heart Association, and the Royal Netherlands Academy of Arts and Sciences.

Prediction of tissue outcome after experimental stroke using MRI-based algorithms

Voorspelling van hersenschade na een experimentele beroerte met op MRI gebaseerde algoritmes

(met een samenvatting in het Nederlands)

Proefschrift

ter verkrijging van de graad doctor aan de Universiteit Utrecht
op gezag van de rector magnificus, prof. dr. G.J. van der Zwaan,
ingevolge het besluit van het college voor promoties
in het openbaar te verdedigen
op dinsdag 7 mei 2013 des middags te 2.30 uur

door

Mark Jacobus Rosalie Joseph Bouts
geboren op 13 januari 1982 te Geleen

Promotor: Prof. dr. ir. M.A. Viergever

Co-promotor: Dr. R.M. Dijkhuizen

Financial support by the Dutch Heart Foundation and the Röntgen Stichting for the publication of this thesis is gratefully acknowledged.

voor pap en mam

Table of Contents

1

General introduction

Ischemic stroke with annually about 5.4 million fatalities world-wide is the fourth leading cause of death. Yet even more patients are left physically or mentally disabled imposing a huge impact on modern society requesting highly specialized and dedicated care from both specialists and family alike. (Lopez and Mathers, 2006) Cerebral ischemia is defined as a significant disturbance of the blood supply to the brain causing a depletion of nutritional delivery, particularly oxygen and glucose, subsequently triggering a cascade of biochemical and metabolic changes which may ultimately lead to neuronal cell death and functional impairment. (Dirnagl et al., 1999; Heiss, 2010) Although recent advancements in stroke treatment have increased the likelihood of favorable outcome considerably, many patients are still denied potentially profitable treatment. (Heiss, 2010)

Ischemic stroke

In ischemic stroke blood flow disturbances often originate from an embolism physically obstructing a cerebral artery or arteriole causing a critical reduction of blood flow to specific parts of the brain. Current treatment guidelines aim at removing this blood clot, thus effectively reinstating the blood flow to the ischemic tissue. Currently, the only effective and clinically approved thrombolytic treatment is based on the administration of recombinant tissue plasminogen activator (rt-PA). However in order to be effective and clinically save, administration of this drug is currently restricted to a time-window of at most 4.5 hours after stroke onset. (Hacke et al., 2008; Wardlaw et al., 2012) Beyond this time-window thrombolytic therapy may be accompanied by risk factors which outweigh the potential benefit of thrombolysis, such as increased risk of reperfusion-related injuries (e.g. blood-brain barrier breakdown, secondary edema), and development of secondary, intracerebral hemorrhage: i.e. hemorrhagic transformation. (Dijkhuizen et al., 2001; Fiehler et al., 2005; Wardlaw et al., 2012) rt-PA itself may furthermore act as a catalyst potentially promoting neurovascular cell death, blood-brain barrier leakage, edema, and hemorrhage (Wang et al., 2004 ;Rosell et al., 2008). Nevertheless when successful, thrombolysis substantially increases the likelihood of good clinical outcome. (Hacke et al., 2008; Wardlaw et al., 2012)

Under the current guidelines it is estimated that less than 5% of all stroke patients would be eligible for thrombolysis. Those excluded are mostly due to late arrival at the hospital. (Hacke et al., 2008) However, it has been argued that expressing potential benefit based on a strict time-oriented manner may be an ill-posed concept and unnecessarily excludes patients that may have benefitted from thrombolytic therapy (Fiehler et al., 2004; Copen et al., 2009; Wardlaw et al., 2012). Especially with evidence that certain patients may respond favorably even well beyond the time-window of 4.5 hours

(Marchal et al., 1996; Hacke et al., 1999; Janjua, 2012; Thomalla et al., 2006; Wardlaw et al., 2012). As a result the need for more individualized stroke treatment decision-making has become more important. This includes the need for establishing reliable methods to non-invasively identify the amount of tissue that may respond favorably to thrombolysis.

Penumbra

Three important concepts in ischemic stroke are the ischemic core, the ischemic penumbra, and the oligemic tissue. The ischemic core is defined as that part of critically hypoperfused tissue that is irreversibly damaged. Surrounding this ischemic core is the ischemic penumbra. The ischemic penumbra is defined as tissue with critically reduced perfusion that - when perfusion is not re-established within a limited period of time - eventually will progress to irreversibly damaged tissue. (Astrup et al., 1981; Moustafa and Baron, 2008; Heiss, 2010) Oligemic tissue is the tissue with moderately reduced blood flow that is not at risk of infarction. (Furlan et al., 1996) The slow progressive recruitment of penumbral tissue 'at risk' into the ischemic core is closely related to the severity and duration of hypoperfusion.

The central nervous system is a highly energy demanding organ that needs sufficient and constant blood flow to maintain its functional tasks. Most of this energy is utilized for the maintenance of membrane function, particularly by preserving ionic homeostasis, and the neuronal propagation of information throughout the brain. This demand may vary over different brain regions dependent on the specific demands. (Heiss, 2010) Prone to the level of hypoperfusion, neurological deficits may arise which gradually increase as flow levels drop. (Astrup et al., 1981; Jones et al., 1981; Moustafa and Baron, 2008) Severely hypoperfused regions, typically with flow levels below 8- 12 mL/100g/min, rapidly progress to an irreversibly damaged state, characterized by low cerebral blood volume, ion pump failure, and energy breakdown. Whereas in regions with less severe hypoperfusion - regions with flow levels around 15 to 25 mL/100g/min and characterized by reduced electrical functioning but preserved morphological integrity, as well as preserved or even increased energy (/oxygen) demand and cerebral blood volume ('misery perfusion') (Moustafa and Baron, 2008) – this progression to an irreversibly damaged state is less immediate and may stretch over a longer period of time. Nevertheless, without salvation penumbral tissue will ultimately become irreversibly damaged. Importantly, this opens up opportunities for interventional therapy. Yet, the length and viability levels of this window of therapeutic opportunity are strongly affected by multiple factors, including the level of vulnerability of the affected tissue (Kirino et al., 1984; Klatzo, 1987), the quality of blood supply from the collateral circulation (Liebeskind, 2003), the increased energy demand as a result of spreading tissue

depolarizations (Hossmann, 1996), history of previous strokes or transient ischemic attacks (Dirnagl et al., 2003; Wegener et al., 2004), co-morbidities (e.g. hypertension or hyperglycemia), and age. (Vora et al., 2011) This effectively limits the time-window for thrombolytic therapy to at most several hours after stroke onset. (Heiss, 2010)

Secondary injury

Thrombolytic therapy aims at re-establishing perfusion to the ischemic tissue. However, the role of reperfusion is ambiguous. Effectively it terminates the ischemic state; however it may also instigate further tissue damage resulting from the reperfusion, i.e. reperfusion injury, or promote development of delayed secondary hemorrhage, i.e. hemorrhagic transformation (HT).

Reperfusion injury can be characterized by an inflammatory cascade that includes along with an excess production of oxygen free radicals (Chan, 2001), an increased cytokine release(Lee et al., 2000; Zoppo et al., 1998), endothelium activation, leukocyte recruitment, and the formation of edema (Klatzo, 1987; Girn et al., 2007; Pan et al., 2007), processes all directly or indirectly related to the integrity of the *blood-brain barrier*. The blood-brain barrier offers a segregating layer between the circulating blood and the extracellular fluid of the central nervous system, and aims at maintaining a delicate homeostatic balance between the blood and tissue in the brain. The blood-brain barrier complex consists of interendothelial tight junctions of capillary and postcapillary venules bounded by the basal lamina and encompassed by the endfeet of astrocytes. (Gregoire, 1989) A unique feature of the BBB, mainly controlled by the capillary endothelium, is its regularizing capacity of solute entry and transit of substances to and from the plasma. (Ding et al., 2006a)

Immediately after vessel occlusion the focal ischemia induces a multitude of processes that directly affect the integrity of the blood-brain barrier. Dependent on the duration and severity of ischemia changes in permeability of the blood-brain barrier may be biphasic or continuous. (Klatzo, 1987) Nevertheless, ultimately with progression of the ischemic injury, necrosis of endothelial cells, and separation of the tight junctions, the regulatory function of the blood-brain barrier cannot be safeguarded anymore causing a flux of fluid and macromolecules (both toxic and non-toxic) along osmotic gradients from intracellular to extracellular spaces. (Klatzo, 1987) Consequent fluid accumulation in the extracellular space, i.e. vasogenic edema, causes increased tissue pressure. A process that may be aggravated when prolonged ischemia causes extracellular compartments to disintegrate, driving osmotic gradients, or when untimely restored blood flow replenishes proteins and water, increasing brain water content. The resulting increased tissue pressure can cause overall swelling of brain tissue that could potentially cause secondary ischemia further exacerbating tissue injury. (Ito et al., 1979)

The blood-brain barrier also plays a pivotal role in the development of intracerebral

hemorrhage. Hemorrhagic transformation, fundamentally a secondary bleeding into the ischemic tissue, occurs after an increase of permeability of the blood-brain barrier. The extravasation of blood into the affected region induces an inflammatory response that may further compromise the integrity of neuronal, glial, vascular and extracellular tissue components. (Wang et al., 2004 ;Rosell et al., 2008). This response can even be enhanced by the administration rt-PA for fibrinolysis. In fact, even within a time-window of less than 3 hours after stroke onset, administration of rt-PA may increase the risk of hemorrhage by an odds ratio of 4.55 (95% confidence interval: 2.92-7.09) by triggering metalloproteinases after stimulation of the plasminogen-plasmin system. (Dijkhuizen et al., 2001; Wang et al., 2004; Rosell et al., 2008; Wardlaw et al., 2012) Hemorrhagic transformation may lead to increased morbidity and mortality, therefore warranting careful considerations of the potential benefits of thrombolysis. (Fiorelli et al., 1999; Larrue et al., 2001)

Magnetic resonance imaging

Accurate assessment and prediction of a patient's condition is crucial to support treatment decision-making where potential benefits should outweigh potential hazards. Non-invasive methods, such as neuroimaging, have become indispensable tools to diagnose tissue status and aid in treatment decision-making. Especially the use of magnetic resonance imaging (MRI), which allows measurement of multiple (early) biomarkers of ischemic stroke, might provide crucial insights to support treatment selection. (Wintermark et al., 2008)

Magnetic resonance imaging utilizes the natural abundance of protons and its intrinsic magnetic properties for the generation of signals that reflect the properties and state of the underlying tissue; signals that can be employed for the construction of anatomical as well as functional images. This selective sensitivity has proven to be very useful for the study of stroke. (Dijkhuizen and Nicolay, 2003)

T_1, T_2 and T_2 imaging*

MRI contrast arising from conventional MR sequences as proton-density, T_1, T_2, T_2* allow for tissue damage assessment during various stages of stroke. (Knight et al., 1994; Li et al., 2000) Considered as useful tools for the detection of ischemia-induced lesions, changes in T_1 and T_2 predominantly arise from the displacement and accumulation of tissue water associated with vasogenic edema. (Dijkhuizen and Nicolay, 2003) The utility of T_1 and T_2 contrast therefore seems to particularly lie in detection of ischemic lesions at the more later (subacute to chronic) stages after stroke. (Dijkhuizen and Nicolay, 2003) Progression of T_2 prolongation and (transient) renormalization of the T_2 at later time-points may inform on changes in tissue status as the infarction develops.

(Knight et al., 1994; Wegener et al., 2006) The utility of T_2*-weighted signal contrast particularly lies in the detection of (micro-)bleedings where deposits of hemosiderin cause local field distortions that shorten T_2*. (Kato et al., 2002) These deposits can be the result of minor blood leakage through damaged blood vessels and have shown to be a predisposing factor for coagulant therapy. (Gorter, 1999; Kwa et al., 1998)

Although some experimental stroke studies (using high-field MRI) reported on an early T_1 change prior to BBB disruption - with sudden changes in flow (Calamante et al., 1999) or early molecular processes involved in endothelial dysfunction as plausible causes (Kaur et al., 2009) – utility of T_1 contrast in early diagnosis of stroke and subsequent monitoring of disease progression particularly lies in the assessment of blood-brain barrier integrity with use of paramagnetic contrast agents. Blood-brain barrier opening and vasogenic edema exacerbate ischemic injury and may contribute to reperfusion injury (see above). Via the use of specialized gadolinium (Gd) chelate-based contrast agents, changes in the blood-brain barrier permeability can be visualized. Tissue accumulation of paramagnetic contrast agent by leakage over the blood-brain barrier, shortens local T_1, giving rise to an increase of T_1-weighted signal. Early enhancements of T_1-weighted signal within brain parenchyma after stroke have been found to correlate well with areas which subsequently develop hemorrhagic transformation (Knight et al., 1998; Dijkhuizen et al., 2001; Neumann-Haefelin et al., 2002; Ding et al., 2006a; Hjort et al., 2008). Under the assumption that the change of R_1 ($1/T_1$) is linearly proportional to a change in tissue concentration of the contrast agent, the amount of leakage can be quantified based on dynamic contrast-enhanced MRI (DCE-MRI). In DCE-MRI serial measurements are used to measure change of Gd-concentration in tissue over time. (Sourbron, 2010) Specialized tracer kinetic theory based one- or multi-compartment models (see (Sourbron, 2010; Sourbron and Buckley, 2012) for review) or model-independent graphical representations, as for instance Patlak-plots (Patlak and Blasberg, 1985; Patlak et al., 1983; Cao et al., 2005; Ewing et al., 2003), allow for the calculation of parameters that represent the extravascular/extracellular volume (V_p) and the blood-to-brain transfer constant (K_i). The latter contains information about plasma flow and the tracer's extraction fraction in relation to the capillary network's permeability-surface area product. (Ewing et al., 2003; Jiang et al., 2012) Experiments with ^{14}C-sucrose have shown a good correlation between the vascular leakage, as assessed with a Patlak graphical model, and the leakage of gold-standard ^{14}C-sucrose, as assessed with post-mortem quantitative autoradiography. (Ewing et al., 2003) Furthermore, Patlak-model derived K_i and V_p measurements from DCE-MRI data were found to correlate well with fibrin leakage indicative of BBB disruption (Jiang et al., 2005), and gross and microscopic hemorrhages when measured at 24 hours post-onset. (Ding et al., 2006a)

Diffusion imaging

Ever since its first application in the early 1990's, diffusion-weighted imaging (DWI) has become one of the workhorses in stroke diagnosis (Moseley et al., 1990; Verheul et al., 1992; Warach et al., 1992). Where a clear change in T_2 is not observed until 2 hours after stroke onset, diffusion-weighted MRI is highly sensitive for detecting acute ischemic distress enabling visualization as early as 3-11 minutes after stroke (Li et al., 1998; Hjort et al., 2005a). It is assumed that this early change in contrast reflects cytotoxic edema - the edematous phase which precedes vasogenic edema and is characterized by intracellular water accumulation with preserved tissue integrity (Klatzo, 1987) - and arises from a net displacement of free water from extracellular to intracellular compartments due to ionic pump failure. The resultant increase in intracellular water volume fraction, reduction of extracellular space tortuosity and increase in intracellular viscosity have all been suggested as factors that reduce the diffusion capabilities of tissue water, which can be observed as a a hyperintensity on diffusion weighted imaging (DWI) or a reduction in apparent diffusion coefficient (ADC). (Moseley et al., 1990; Sevick et al., 1992; Verheul et al., 1992; Warach et al., 1992)

Diffusion-weighted imaging exploits the inherent sensitivity of MRI to motion. Self-diffusion, the process of random motion of molecules in water propagated by endemic thermal energy (i.e. Brownian motion), is expressed as a constant isotropic net displacement of a solute in a limited period of time. (Einstein, 1905) However in biological tissues, semipermeable membranes and organelles strongly attenuate this displacement constant of water, or diffusion coefficient, making direct measurement of the displacement unfeasible. It is therefore expressed as the Apparent Diffusion Coefficient (ADC). In DWI, diffusion-sensitized gradients measure the displacement of water through the magnetic field. The resulting signal change can be utilized to calculate quantitative representation of ADC (mm^2/s) either by voxel-wise linearly fitting the log-transformed signal ratio expressed by the Stesjkal-Tanner equation (Stejskal and Tanner, 1965), or by measuring the displacement of water in multiple directions (at least 6) from which a symmetric 3x3 matrix can be constructed, a technique also known as diffusion tensor imaging (DTI). By means of eigenvalue decomposition, ADC maps can be derived by averaging the sum of the diagonal eigenvalues (i.e. trace) of the matrix. (Basser et al., 1994) Furthermore this approach informs on the directionality of the displacement expressed by the fractional anisotropy (FA) (see for review (Basser et al., 1994)).
Early stroke studies heralded DWI as a highly sensitive method for imaging cerebral ischemia in the hyperacute stages of stroke. (Moseley et al., 1990; Bihan et al., 1992; Warach et al., 1992). Soon followed by observations in both preclinical as clinical studies that linked acute diffusion abnormality to infarcted tissue at follow-up based on a good

volumetric correlation, even speculating on a close relation of DWI abnormality with the ischemic core. (Minematsu et al., 1992; Verheul et al., 1992; Warach et al., 1995) Furthermore, severe ADC reductions or large volumes of DWI abnormality (100 mL) may hold a malignant profile, identifying patients likely to have poor outcome and high potential of developing hemorrhagic transformation. These patients should thus be excluded from thrombolytic treatment. (Selim et al., 2002; Albers et al., 2006; Mlynash et al., 2011) However, this claim is questioned with reports on reversal of the diffusion abnormality after reperfusion with tissue salvage within the initial DWI lesion. (Minematsu et al., 1992; Kidwell et al., 2000; Fiehler et al., 2004; Olivot et al., 2009a) Further studies tried to elucidate the specificity of DWI in predicting the ischemic core and found that the number of false positive acute DWI lesions could be observed on average in 24% of the cases. (Kranz and Eastwood, 2009) MR/PET studies supported this by showing that the DWI lesion not only contained ischemic core tissue, but also substantial proportions of the penumbra even in areas with low values of ADC. (Guadagno et al., 2004) This raises questions on the applicability of set thresholds for estimating irreversible injury. (Fiehler et al., 2004; Guadagno et al., 2004; Sobesky et al., 2005) DWI reversibility is difficult to predict and subsequent tissue salvage is not guaranteed. Longitudinal experimental MRI studies with subsequent histological assessment in rats even revealed recurrence of diffusion abnormality with subsequent secondary damage. (Dijkhuizen et al., 1998a; Li et al., 1999; Neumann-Haefelin et al., 2000) Debates on the specificity of the diffusion abnormality for detecting irreversibly damaged tissue remain open-ended. (Campbell et al., 2012) All in all, diffusion-weighted imaging may be regarded as a marker for tissue infarction with a high sensitivity but at most moderate specificity. (Schellinger et al., 2010; Sobesky, 2012)

Diffusion imaging may also play a role in tracing back stroke onset times. As time progresses ADC signal changes due to morphological changes of the underlying cell structures. After decrease in the initial hours of stroke, the ADC slowly changes to pseudo-normal values (pseudo-normalization) caused by a slow resolution of cytotoxic edema, loss in cell membrane integrity and vasogenic edema. As tissue damage progresses, increased extracellular water levels and tissue cavitation cause the ADC signal to further increase. The rate of these changes depend on many determinants among others: species, type of stroke, tissue type, reperfusion time, and age. (Warach et al., 1995; Welch et al., 1995; Liu et al., 2007).

Angiography

Magnetic resonance angiography (MRA) allows for the visualization of large arteries in the brain. The most popular technique utilizes endogenous contrast by measuring inflow of blood with unsaturated MR signal, into a saturated imaging plane. By constantly

applying radiofrequency pulses within a limited repetition time, the stationary tissue slowly becomes saturated expressed by reduced MR signal. With supply of fresh blood without signal saturation into the imaging plane, an increased signal intensity from inflowing blood compared to the stationary tissue can be detected. (Reese et al., 1999) This fast gradient echo-based time-of-flight (TOF) MRA technique can be employed to visualize the vessels of the circle of Willis. Occlusions – partial or complete - in sections of the circle of Willis can be identified as signal voids which may be useful in rapidly identifying arterial obstruction. However, since MRA is sensitized to specifically higher flow values it may overestimate the degree of arterial obstruction. (De Silva et al., 2010) Furthermore, it seems hampered by low sensitivity in the more distal parts of the vascular supply. (Reese et al., 1999)

Perfusion imaging

Where MRA allows for imaging of flow in the macroscopic vessels, perfusion-weighted imaging allows for imaging of microvasular hemodynamics and therefore provides a highly sensitive tool for detecting areas with impaired (micro-)perfusion.
Perfusion-weighted MRI involves the acquisition of contrast-induced signal changes resulting from the passage of intravascular contrast agent through the imaging plane (Østergaard, 2004; Copen et al., 2011) These signal changes either originate from an endogenous or exogenous contrast agent. In arterial spin labeling (ASL), focused radio-frequency pulses magnetically label arterial blood before it enters the imaging plane. With earlier acquired baseline images as reference, subsequent T_1-weighted acquisitions allow for the estimation of cerebral blood flow based on the label-induced signal attenuations. (Williams et al., 1992) ASL allows for perfusion imaging with no potentially adverse effects of exogenous contrast agent and unlimited repetitive imaging possibilities. However, especially in stroke imaging, ASL is hampered by its lack of sensitivity in low flow areas (e.g. white matter or ischemic areas), its sensitivity to patient motion, its relatively low signal-to-noise ratio, and relatively long acquisition times. Therefore, perfusion imaging after clinical stroke mostly utilizes dynamic susceptibility contrast-enhanced MRI (DSC-MRI) or "bolus-tracking" MRI. DSC-MRI dynamically tracks the first passage of a rapidly injected bolus of paramagnetic gadolinium (Gd) chelate. The passage of the contrast agent induces susceptibility distortions which can be measured with T_2 (spin echo-based) or T_2*-weighted (gradient echo-based) MRI.

Similar to DCE-MRI used for quantification of BBB leakage (see above), DSC-MRI uses tracer kinetic theory to describe the hemodynamic condition of the underlying tissue. Assuming a linear relationship between contrast agent concentration and ΔR_2 or ΔR_2*, the change in concentration over time during passage of a bolus of contrast agent can be characterized by concentration-time curves. (Rosen et al., 1990) With

a residue function being the fraction of tracer in the perfused tissue, and an arterial input function representing the delivery of contrast agent to the observed tissue, these concentration-time curves can be defined as a convolution of the arterial input function with the residue function scaled by the rate at which the bolus travels, i.e. the cerebral blood flow. Although an ever growing list of possible modeling approaches ranging from model-free (Thompson et al., 1964; Østergaard et al., 1996), model-dependent (Østergaard, 2004; Mouridsen et al., 2006), or more statistical approaches (Vonken et al., 2000) has been suggested for estimation of the residue function (Knutsson et al., 2010), the most popular and most robust approach remains singular value decomposition (Østergaard et al., 1996), and then especially the tracer arrival time-insensitive block-circulant deconvolution approach. (Wu et al., 2003; Christensen et al., 2009). This approach decomposes the concentration-time curve based on the measured signal and a provided arterial input function, resulting in an estimate of the residue function. The residue function allows for the calculation of local CBF and CBV as the height of and area under the residue curve, respectively. Furthermore, characteristics on bolus arrival can be obtained from T_{max}, representing the time to maximum concentration, and mean transit time, the time the tracer spends in the tissue of interest, usually calculated as the CBV/CBF ratio.

Ever since early animal experiments revealed a dependence of initial ischemic damage on the extent of reduced flow (Jones et al., 1981), CBF-based viability thresholds to identify tissue at risk have been extensively investigated with moderate success. Although appealing, the application of flow thresholds for identification of core versus salvageable tissue is very cumbersome and quite often includes oligemic tissue. CBF – and its thresholds for irreversible damage –may vary greatly depending on many factors including age, tissue type (white matter vs gray matter), and duration of ischemia. (Warach, 2001 ;Moustafa and Baron, 2008; Christensen et al., 2009) Furthermore, CBF derived from DSC-MRI are currently semi-quantitative at most, as quantification of flow values is still very challenging and shares high attention in current research. (see for review (Calamante et al., 2006; Knutsson et al., 2010))

In contrast, CBV has received relatively little attention as a potential marker for tissue outcome. As part of the compensatory mechanism to maintain blood supply to the ischemic tissue, CBV has often been studied in relation to CBF. Acutely hypoperfused areas characterized by low CBF are often accompanied by compensatorily increased local CBV. However when local CBV levels cannot be maintained, CBF further drops and tissue function rapidly degenerates with irreversible injury as a consequence. (Copen et al., 2011) Areas with very low CBV (<2.5% of normal values) may even be predictive of development of hemorrhagic transformation. (Alsop et al., 2005; Campbell et al., 2010a) Areas where CBV can be maintained or even increased, i.e. areas with a

flow-volume mismatch (low CBF with normal or increased CBV), may reflect tissue at risk but where progression to infarction may be averted. (Hamberg et al., 1996; Dijkhuizen et al., 1997)
The CBV/CBF ratio, i.e. MTT, along with T_{max} have been heralded as useful and sensitive markers for identifying tissue at risk. (Christensen et al., 2009; Wu et al., 2011) Mapping of these parameters allows straightforward recognition and delineation of hypoperfused areas. Mainy because of little contrast difference between white and gray matter and because intensities are naturally scaled by the repetition time used for imaging. (Zaro-Weber et al., 2010; Wu et al., 2011; Fisher and Bastan, 2012; Sobesky, 2012) T_{max} also informs on bolus dispersion, expressed by larger transit time, and bolus delay, thus providing useful information on potential alternative (collateral) blood supply. (Liebeskind, 2003; Christensen et al., 2009) These pathways may sustain tissue integrity for a longer period of time, but may not be sufficient to prevent irreversible damage at later time-points, therefore warranting treatment. (Liebeskind, 2003; Bang et al., 2008) **Despite its potential to delineate tissue tissue at risk, consensus on thresh**olds to delineate hypoperfused areas that predict infarct progression and/or positive response to therapy has not been achieved. (Kane et al., 2007a; Zaro-Weber et al., 2010)

Figure 1.1 summarizes the above described MR imaging techniques and their utility in ischemic stroke. Parametric maps of two rats with right-sided middle cerebral artery occlusion, acquired within 2 hours after onset, indicate acute tissue lesions. Subsequent MRI after 7 days depicts tissue infarction, tissue salvage (upper row), or hemorrhagic transformation (bottom row).

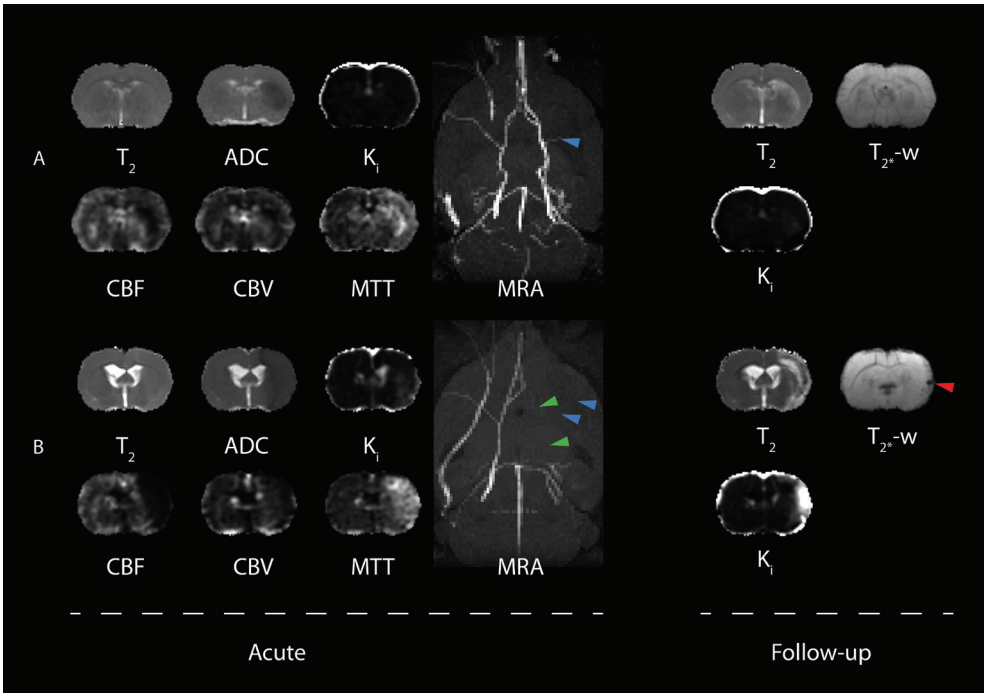

Figure 1.1. *Example images of coronal slices of a rat brain from two rt-PA-treated rats after right-sided middle cerebral artery occlusion with subsequent tissue salvage (A) or hemorrhagic transformation (B). Acute (2 hours post-stroke; before treatment) maps indicate tissue lesion with reduced apparent diffusion coefficient (ADC; hypointensity), reduced cerebral blood flow (CBF) and cerebral blood volume (CBV), and prolonged mean transit time (MTT; hyperintensity). T_2 maps indicate no apparent abnormal tissue. Magnetic resonance angiography (MRA) clearly shows reduced flow in the ipsilateral middle cerebral artery (A & B, blue arrows) and internal carotid artery (B, green arrows). K_i maps, indicative of blood-brain barrier permeability, reveal minor K_i increase in animal B but not in animal A. In contrast to animal B, a mismatch between the ADC and MTT abnormal volume, i.e. perfusion-diffusion mismatch, can be observed for animal A signifying tissue potentially salvageable by thrombolytic therapy. Subsequent follow-up imaging (7 days post-stroke; post treatment) reveals tissue injury reflected by prolonged T_2 (hyperintensity). Prevention of lesion progression was confirmed in animal A with final tissue lesion size being smaller than the volume of acute perfusion abnormality. Substantial K_i increase and hypointense regions on T_2*-weighted images in animal B reflect disruption of blood-brain barrier integrity and hemorrhagic transformation in the temporal cortex (red arrow).*

Perfusion-diffusion mismatch

Estimating tissue salvageability is a key aspect in the prediction of tissue outcome after stroke. The amount of salvageable tissue determines treatment potential. At the advent of diffusion-weighted imaging being sensitive for the detection of irreversible tissue damage and perfusion-weighted imaging being sensitive for the detection of hemodynamic disturbances, it was observed that acute DWI-derived lesion volumes were smaller compared to those derived with PWI. (Knight et al., 1994; Baird et al., 1997) It was therefore speculated that this non-overlapping region or perfusion-diffusion mismatch may hold tissue amenable for treatment, i.e. the ischemic penumbra. It has been proposed that this mismatch may be used as a surrogate marker for detection of tissue at risk even well beyond the time-window of 3 to 4.5 hours. Some studies even report on observed PWI/DWI mismatches as late as 12-24 hours post onset (Copen et al., 2009). Effectively the perfusion-diffusion mismatch may function as the more preferred 'tissue clock' rather than the currently applied 'wall clock'. (Wu et al., 2011) Large phase II clinical trials as Echoplanar Imaging Thrombolytic Evaluation Trial (EPITHET) or Diffusion and Perfusion Imaging Evaluation For Understanding Stroke Evolution (DEFUSE) have shown patients with PWI/DWI mismatch to profit more from thrombolysis at 3-6 hours after stroke onset than those without (Albers et al., 2006; Nagakane et al., 2010), whereas other trials that explicitly used the PWI/DWI mismatch for patient recruitment (Desmoteplase in acute ischemic stroke (DIAS) and Desmoteplase for Acute Ischemic Stroke (DEDAS)) failed to observe an obvious beneficial effect. This discrepancy is likely to arise from clear differences in thresholding standards and definitions of mismatch.

In essence the perfusion-diffusion mismatch holds two important challenges (Kidwell et al., 2003):

1. The diffusion-weighted abnormality may (temporarily) reverse after restoring blood flow with areas of subsequent tissue salvage (See above)

2. Perfusion-weighted abnormal regions overestimate the region at risk including penumbral tissue and benign oligemia.

Particularly, definitions of perfusion thresholds are considered most problematic. Despite rigorous attempts for validation, clear thresholding standards seem heavily dependent on the perfusion parameter used. (Kane et al., 2007a) Although recent studies showed highest potential for T_{max} or MTT, clear and fixed threshold values are still disputed. (Sobesky et al., 2004; Christensen et al., 2009; Olivot et al., 2009b; Zaro-Weber et al., 2010)

Without clear acquisition and image post-processing standards the quality of this approach may remain insufficiently reliable. (Kane et al., 2007b; Campbell et al., 2010a; Sobesky, 2012) Furthermore, the mismatch concept does not consider other important aspects that determine outcome. Infarct location, existence or absences of collateral flow, the site of large vessel occlusion, to name of few, are all important aspects - which particularly in longer time-windows beyond 4.5 hours - may hold key information on the success of thrombolysis. (Ma et al., 2009; Harrer, 2010; Sobesky, 2012)

Some alternatives to the perfusion-diffusion mismatch have been suggested. Alternatives that circumvent the need for perfusion-weighted imaging: the clinical-diffusion mismatch and the MRA-diffusion mismatch. The clinical-diffusion mismatch combines clinical assessment scoring with the initial diffusion weighted volume and is suggested as an alternative approach to select patients that may benefit from thrombolysis. A clinical-diffusion mismatch operates under the assumption that patients with a diffusion-weighted imaging lesion volume of ≤25mL and a score of ≥ 8 on the national institutes of health stroke scale (NIHSS) have a higher probability of infarct growth and early neurologic deterioration. These patients would therefore benefit most from thrombolytic therapy. Although, appealing this approach seems not able to compete with the specificity and sensitivity of the perfusion-diffusion mismatch method. (Dávalos et al., 2004; Ebinger et al., 2009)
The MRA-diffusion mismatch is another alternative that reduces flow information to the presence or absence of large vessel occlusions in the area of the circle of Willis in combination with a limited diffusion-weighted lesion volume of at most 25mL. (Lansberg et al., 2008) The MRA-diffusion mismatch utilizes the fact that diffusion lesion volume size depends on the site of vessel occlusion. Particularly occlusions in the internal carotid artery and the proximal (M1) branch of the middle cerebral artery have been associated with substantial infarct growth and poor outcome at later time-points. (Fiehler et al., 2005; Saarinen et al., 2012) Although, thrombolysis of these regions may be challenging, successful thrombolysis does increase the probability of good outcome. (De Silva et al., 2010; Deguchi et al., 2012) This approach has shown great promise in identifying patients with high risk of infarct growth as time progresses, and showed good correlation with perfusion-diffusion mismatch based predictions. (Deguchi et al., 2011) *Nevertheless, this approach raises concerns on the sensitivity towards more distal vessel occlusions, and does not account for regional perfusion and the presence of collateral flow. (Sobesky, 2012) These concerns require further research to establish the significance of the MRA-diffusion mismatch (see Chapter 3).*

Multiparametric voxel-wise prediction

While qualitative assessment of the tissue at risk of infarction by means of mismatch analysis may hold clinical potential in decision-making, quantitative assessment may further extend utility in both clinical and preclinical stroke research. The definition of proper thresholds for the determination of tissue at risk of infarction has proven to be very challenging due to a complex interplay of different hemodynamic and metabolic processes. It has therefore been speculated that this complex relationship, as captured with multiple MR indices, may be better apprehended by combining these on a voxel-wise basis. These multiparametric voxel-wise methods utilize historically acquired data and allow for the classification of different tissue types by integrating important aspects of tissue viability as time, hemodynamic status, tissue status, and intervention within a single quantitative index. (Warach, 2001; Østergaard et al., 2009; Wu et al., 2010)

Multiparametric methods combine intensity values of multiple MRI indices (M) in a single vector ($x_j=<x_i,..,x_M>$) and on a voxel-wise basis relate them to a specific tissue type (Y_j, e.g. core or penumbral tissue). The resulting tissue theme maps offer a simplified representation of the underlying tissue status. The relation between the input vector and tissue type can be expressed based on a linear or non-linear function which coefficients are optimized either by supervised or non-supervised learning. Supervised learning is used for predicting a specific tissue class based on newly introduced samples (e.g. the probability of infarct). In this approach input vector examples along with their corresponding target tissue vectors (e.g. infarct versus non-infarct) are provided in order to optimize (or 'train') a set of coefficients. These coefficients can subsequently be used for estimating tissue class likelihood of newly introduced input vectors. Unsupervised learning aims to group all those input vectors which carry great similarity within the presented data without the actual tissue class being known. These grouped or clustered input vectors may then represent a specific tissue class. Many different methods are described (see for review (Bishop, 2007; Hastie et al., 2009)), here I briefly present a subselection of those considered useful for the rest of this thesis.

Unsupervised clustering methods may provide an unbiased means for prediction of tissue fate and therapeutic efficacy monitoring. (Ding et al., 2004; Shen et al., 2004a) *K*-means clustering, a method that aims at minimizing intra-cluster dispersion of the *K* selected clusters, offers a multiparametric approach that was shown to more reliably identify ischemic tissue based on structural, diffusion, and perfusion data together, than when these MRI indices were used separately. (Carano et al., 2000) However, *K*-means clustering asks for *a priori* decisions on the number of clusters, potentially obscuring subtle variations in stroke development which may aid in elucidating stroke progression

or treatment efficacy monitoring. (Nagesh et al., 1998) Therefore an extended variant of *K*-means clustering was employed that circumvents the need for *a priori* selection of the number of clusters: iterative self-organizing data analysis (ISODATA). (Ball and Hall, 1965) ISODATA dynamically adjusts the number of clusters by iteratively splitting or merging clusters implicitly maximizing inter-cluster distances with concurrent minimization of intra-cluster dispersion. ISODATA showed good correlation between abnormal tissue clusters and subsequent tissue injury in histologically validated experiments in rats (Jacobs et al., 2000, 2001a; Soltanian-Zadeh et al., 2003), and in humans where abnormal tissue clusters at different stages after stroke corresponded well with subsequent infarction at follow-up (Soltanian-Zadeh et al., 2007) or neurological outcome. (Jacobs et al., 2001a; Mitsias et al., 2002) Furthermore, ISODATA clustering contributed to the identification of multiple tissues with ischemic injury, including penumbral tissue, tissue with increased blood-brain barrier permeability, and tissue with increased responsiveness to treatment, that may not be simply detected using analysis of each MR parameter separately. (Nagesh et al., 1998; Jacobs et al., 2001b; Li et al., 2005; Mitsias et al., 2002; Soltanian-Zadeh et al., 2007) *However, although ISODATA and other clustering techniques might enable prediction of tissue infarction, these techniques are limited by providing discrete classes of grouped voxels based on similarity estimates without knowledge of the underlying pathophysiology. Interpretation of the underlying pathophysiology of different classes may become cumbersome when the number of classes increases; when classes are based on a large number of MRI indices; or when temporal relations need to be defined (Shen et al., 2004b) (see Chapter 2).*

Supervised approaches estimate on a voxel-wise basis a specific tissue class with prior knowledge on the underlying pathophysiology. Early predictive algorithms employed 2-dimensional histograms that functioned as look-up tables to categorize tissue progression ranging from normal to necrosis based on ADC and T_2 data (Welch et al., 1995), or ADC and CBF. (Shen and Duong, 2008) Although easy to apply and interpret these models did not provide easy means to incorporate more than two or three MRI indices. Predictive algorithms have the added benefit for estimating a likelihood or probability of voxels belonging to a specific (tissue) class. This probability estimate thus effectively provides a single quantitative index which can easily be interpreted irrespective of the MRI indices used. (Østergaard et al., 2009; Wu et al., 2010) In stroke research different MRI-based predictive algorithms have been proposed for predicting the probability of tissue infarction ($P_{infarct}=P(infarct|x_1,..,x_m)$). A generalized linear model (GLM) that combined T_2, diffusion, and perfusion MRI indices, successfully utilized this approach to give voxel-wise estimates of the probability of tissue progressing to infarction. (Wu et al., 2001) Furthermore, subsequent analysis revealed heterogeneity in the assigned infarct probabilities holding potential for discriminating tissue regions likely

to respond favorably to thrombolytic therapy. (Wu et al., 2006, 2007) *These predictive algorithms may therefore not only contribute to determination of tissue infarction, but may also elucidate or contribute to better understanding of potential effects of treatment-induced changes (see Chapter 4). These predictive algorithms may especially provide valuable therapeutic guidance when treatment-induced changes could result in further exacerbating tissue injury, as with hemorrhagic transformation (see Chapter 5).*

Figure 1.2 illustrates supervised multiparametric prediction modeling with a generalized linear model based on three parametric maps (ADC, CBF, and MTT). For model training (left panel), acutely acquired parametric maps are correlated on a voxel-wise basis to subsequent presence of tissue infarction on follow-up images. This process is repeated for all voxels from all animals available for training. Subsequently the GLM algorithm estimates a hyperplane that separates the infarcted from the non-infarcted voxels. Infarction risk of a newly introduced subject can subsequently be calculated by estimating the distribution pattern of the newly introduced voxel combinations in relation to the separating plane (right panel).

GLM, however, assumes a linear relation between the MRI parameters and the actual outcome, which may not be always correct. Both low and high ADC values have for instance been found predictive of tissue infarction. (Sorensen et al., 1999a) Similar observations were made for CBV. **(Sorensen et al., 1999b) Hence, it has been specu**lated that algorithms describing a non-linear relation between the acute parameters and eventual tissue outcome may hold more benefit over linear approaches. Therefore more complex predictive algorithms have been suggested as k-NN (Gottrup et al., 2005), support vector machines (Huang et al., 2011), or artificial neural networks (Huang et al., 2010 ; Bagher-Ebadian et al., 2011), that all showed good accuracy in predicting the extent of tissue infarction. *Although, promising these approaches lack direct comparison to appreciate their potential benefit for predicting tissue outcome as well as their benefit to interpretation of stroke progression (see Chapter 4).*

To conclude, multiparametric MRI offers a versatile tool that holds unique potential for the identification and subsequent monitoring of tissue at risk of infarction, and potentially also hemorrhagic transformation. Although clear practical threshold values are still unsecure and many patients remain withheld from potentially viable treatment, the use of concepts as the perfusion-diffusion mismatch has opened up opportunities for patients for whom treatment would previously be denied. Particularly the development of voxel-wise approaches, which allow for the integration of different aspects of stroke pathology within a single index, may alleviate the necessity for clear thresholding standards, and in the end offer better support in individual clinical decision-making or treatment efficacy monitoring.

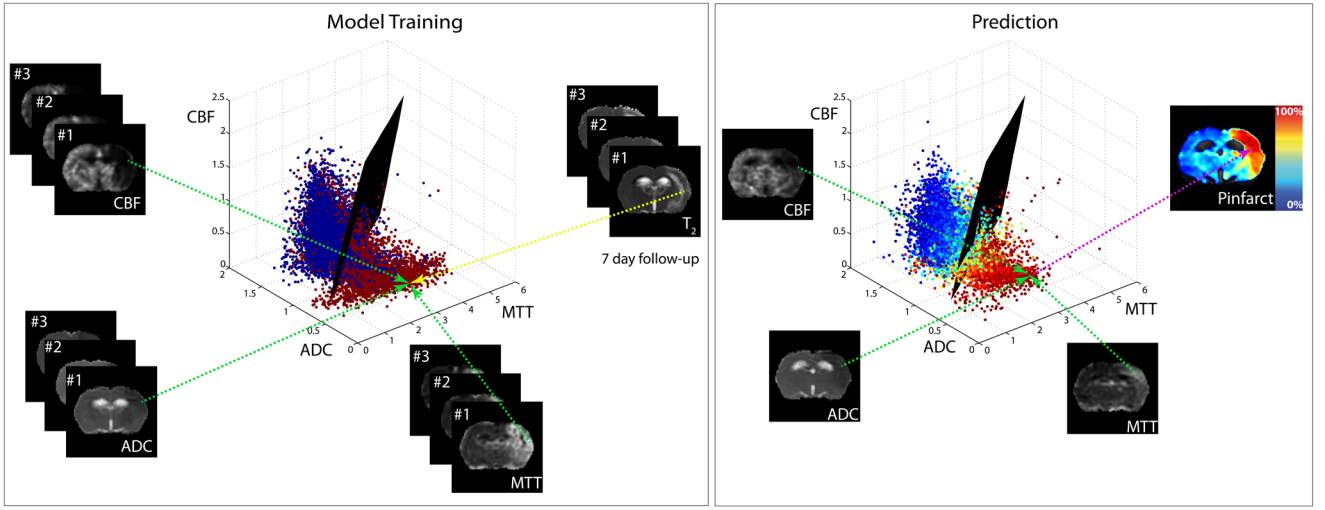

Figure 1.2. *Multiparametric MRI-based prediction models utilize voxel-wise combinations of multiple originally acquired MR images in correspondence with subsequent follow-up imaging to determine tissue fate from newly introduced samples. During model training (left) acutely acquired multiparametric imaging data (e.g. ADC, CBF, and MTT maps) are voxel-wise related to tissue outcome (i.e. infarcted (red) or non-infarcted tissue (blue)) derived from follow-up images to record tissue outcome. Subsequently a prediction algorithm (e.g. generalized linear model) estimates a separating plane that aims to isolate infarcted from non-infarcted tissue voxels. In tissue outcome prediction of a new subject, the distribution pattern of the newly introduced voxel-wise combinations relative to the separating plane is used to estimate infarction risk ($P_{infarct}$; right). Note, that while increasing the number of MRI parameters for tissue fate determination increases model-complexity, it does not contribute to increased diagnostic complexity, because a single index is provided as output measure.*

Animal models

With the availability of various ischemic stroke models in different animal species and strains, animal experiments provide well-controllable, repeatable and translational means for detailed assessment of stroke progression and treatment monitoring with the opportunity of direct post mortem histological validation. (Liu et al., 2009) Rats and mice are by far the most used animal species in stroke research, because of their low costs, genetic homogeneity, and comparable cerebral organization to that of humans. Many focal stroke models have been described in literature, all mimicking different aspects of stroke (see for review (Liu et al., 2009)). Three different approaches may be of special interest. These involve occlusion of the middle cerebral artery (MCA), either by means of an intraluminal thread (Longa et al., 1989; De Crespigny et al., 2005), or by means of an autologous or homologous blood clot. (Zhang et al., 1997) The intraluminal thread can be permanently left in place, effectively mimicking a worst-case scenario in which reperfusion is not established, or the catheter can be removed to allow reperfusion after a defined period of time. The use of an autologous blood embolus in effect better replicates the human-like thromboembolic stroke than the intraluminal thread models. Furthermore this model allows for subsequent thrombolysis by treatment with rt-PA, but reperfusion onset times may vary significantly. (Liu et al., 2009) With longer presence of a perfusion-diffusion mismatch compared to intraluminal thread models, the embolic stroke model may be better suited for testing tissue salvageability. (Henninger et al., 2006)

The development of hemorrhagic transformation poses a potential threat for thrombolytic treatment, which is strongly associated with factors that affect endothelial structure and function, such as hypertension. Chronic hypertension has been associated with poorer prognosis after stroke (Vora et al., 2011), with increased likelihood of development of hemorrhagic transformation. (Dijkhuizen et al., 2001) Experimental stroke in spontaneously hypertensive rats may therefore provide a useful tool to assess hemorrhagic transformation and to identify early predictive biomarkers.

Despite their importance in experimental stroke research, there are intrinsic differences in stroke evolution between lissencephalic rodents and gyrencephalic humans. (Tagaya et al., 1997) Stroke evolution in non-human primates is more comparable to that of humans. (Liu et al., 2007; Fisher et al., 2009) However due to ethical issues and high costs, experiments on primates are conducted to a limited extent and in limited numbers. Nevertheless studying disease progression in these animals can provide unique and valuable information on stroke pathophysiology and clinical monitoring tools. (Liu et al., 2007)

Aims of the thesis

Cerebral ischemia involves a highly complex pathophysiology. Every step in the progression of ischemic injury is determined by interplay of many factors including time from onset, hemodynamics, and the underlying tissue characteristics. An important aspect in individualized stroke patient management is to determine the potential benefits and risks of therapeutic intervention. Evidently this involves the identification and subsequent monitoring of ongoing pathophysiological changes after acute stroke. MRI as a versatile tool allows for longitudinal and concurrent assessment of different pathophysiologic aspects of the post-stroke development process. MRI-based approaches as described above all seem to contribute to improvement of individualized decision-making. However, although previous merit has been found with volumetric analysis methods for tissue outcome prediction, these methods may be compromised by lack of processing standards and may potentially obscure heterogeneity of the underlying tissue. It has therefore been speculated that voxel-wise methods that combine different aspects of stroke within a single index may overcome particular issues and may hold more potential for prediction of tissue outcome after stroke. The main objective of this thesis was to elucidate the potential of voxel-based models for prediction of tissue outcome after stroke. To that aim, various voxel-based statistical models were evaluated in their potential for tissue progression monitoring and tissue outcome prediction, based on serially acquired multiparametric MRI data in experimental animal models of stroke.

In **Chapter 2** we aimed to identify unique spatiotemporal magnetic resonance imaging (MRI) patterns in macaque brain at acute, subacute, and chronic stages after experimental stroke. To that aim we employed a modified ISODATA algorithm to evaluate T_2 and diffusion changes after permanent and 3-hour transient MCA occlusion. The identified spatiotemporal profiles were subsequently correlated to histologic features on post mortem brain sections.

Chapter 3 combined magnetic resonance angiography and diffusion MR imaging to determine the efficacy of the MRA-Diffusion mismatch to identify tissue responsive to therapeutic intervention. Our objective was to elucidate the influence of the vascular occlusion site on acute diffusion- and perfusion-derived lesion volumes, and to determine the presence or absence of a MRA-diffusion mismatch in normo- and hypertensive rats with embolic large vessel occlusions.

In **Chapter 4** maps of T_2, diffusion, and perfusion were combined to determine the ability of infarct prediction algorithms to explicitly depict affected tissue amenable for treatment, i.e. the salvageable tissue. To that aim five predictive algorithms (Generalized Linear Model, Generalized Additive Model, Support Vector Machine, Adaptive Boosting and Random Forest) were tested in intraluminal thread and embolic rat stroke models. The first part of this study assessed the efficacy of each algorithm in identifying tissue at risk of infarction. The second part aimed at clarifying the potency of each of these algorithms to delineate acute cerebral ischemic tissue that can recover upon reperfusion.

Benefit from thrombolytic therapy may be abrogated by hemorrhagic transformation. Timely identification of tissue at increased risk of hemorrhagic transformation forms a crucial part in treatment decision-making. The goal of **Chapter 5** was to determine the potency of voxel-wise prediction methods in identifying tissue at increased risk of hemorrhagic transformation after cerebral ischemia-reperfusion injury in spontaneously hypertensive rats. Therefore MRI informing on the brain's structural, diffusion, perfusion, and blood-brain barrier status were combined in two types of predictive algorithms to determine their efficacy in identifying ischemic tissue that displayed hemorrhagic transformation at follow-up.

In **Chapter 6**, findings described in Chapters 2-5 are discussed, and pitfalls and future directions are outlined.

2

Distinct spatiotemporal patterns of changes after stroke in non-human primates using MRI-based cerebral tissue classification

Mark. J. R. J. Bouts[1,2],Susan. V. Westmoreland[3],
Alex J. de Crespigny[1],Yutong Liu[1,4] ,Mark Vangel[1],
Rick M. Dijkhuizen[2], Ona Wu[1], and Helen E. D'Arceuil[1]

[1]Athinoula A. Martinos Center for Biomedical Imaging,
Department of Radiology, Massachusetts General Hospital,
Charlestown, MA, United States.
[2]Biomedical MR Imaging & Spectroscopy Group, Image Sciences Institute,
University Medical Center Utrecht,
Utrecht, The Netherlands.
[3]New England Primate Research Center, Pathology,
Southborough, MA, United States.
[4]Department of Radiology, The University of Nebraska Medical Center,
Omaha, NE, United States.

Submitted for publication

Abstract

An improved iterative self-organizing data-analysis (ISODATA) algorithm was used to spatially and temporally map ischemic tissue changes, on a voxel-by-voxel basis, within the brains of macaques that were subjected to middle cerebral artery occlusion (MCAo). Aims of this study were three-fold: (1) to determine unique temporal magnetic resonance imaging (MRI) patterns at the acute, subacute and chronic stages after experimental stroke by combining quantitative T_2 and diffusion MRI indices, (2) to evaluate temporal differences in these parameters between transient (n=2) and permanent (n=2) MCAo, and (3) to correlate histopathology findings in the chronic stroke period to the acute and subacute MRI derived tissue signatures.

ISODATA was used to combine T_2, apparent diffusion coefficient (ADC), and fractional anisotropy (FA) maps across seven successive timepoints. Analysis revealed five temporal MRI patterns or 'Signatures', that were substantially different from the normal tissue pattern ($P<0.001$). These signatures each represented regions with different histopathology, and their distribution differed significantly between permanent and transient MCAo models ($P<0.001$). Two signatures identified areas of progressive injury marked by severe necrosis and the presence of gitter cells. Another signature identified less severe but pronounced neuronal and axonal degeneration, while the other signatures depicted tissue remodeling with vascular proliferation and astrogliosis. These results demonstrate the potential of temporally and spatially combined voxel-based methods to generate tissue signatures that correlate with distinct histopathological features. Identification of ischemic MRI signatures that signal a specific tissue fate may aid in assessing and monitoring the efficacy of novel pharmaceutical treatments for stroke in a pre-clinical setting. Additionally, these MRI-based techniques can be readily applied in a clinical setting opening up opportunities for identification of salvageable tissue with the ability to monitor processes of recovery and rehabilitation.

Introduction

Diffusion-weighted imaging (DWI) is sensitive for the early detection of ischemic tissue injury due to stroke, with changes being visible as early as 11 minutes post-onset (Siemonsen et al., 2012). However, ischemic DWI changes have been shown to reverse post-recanalization (Fiehler et al., 2002; Kidwell et al., 2000), with secondary injury observed in some cases (Dijkhuizen et al., 1998a; Fiehler et al., 2002; Kidwell et al., 2002; Li et al., 1999). Greater understanding of the temporal evolution of DWI under conditions of ischemia and reperfusion is therefore important for accurate diagnosis and management of stroke patients. Serial MRI studies performed in experimental rat stroke models have shown that the spatiotemporal progression of tissue injury after focal ischemia is heterogeneous and differs between animals that reperfuse and those that do not (Shen et al., 2004b). However, because rodents have intrinsically different stroke evolution patterns than primates (Tagaya et al., 1997), it has been suggested that serial studies using gyrencephalic primates potentially provide more representative insight into lesion evolution in human stroke (Fisher et al., 2009).

A previous study on post-stroke changes in T_2 and diffusion tensor imaging (DTI) parameters indeed found that lesion evolution after permanent and transient stroke in cynomologous macaques is more consistent with changes observed in human stroke patients, compared to rodent stroke models (Liu et al., 2007). In that study, differences in lesion evolution were studied using volume-of-interest analysis. However, volumetric analysis may introduce bias from regional tissue averaging, potentially obscuring local temporal variations in lesion development (Nagesh et al., 1998; Jacobs et al., 2000; Liu et al., 2007). Several studies have demonstrated that voxel-based cluster analysis can provide improved insights into the local characteristics of regional tissue changes after stroke (Welch et al., 1995; Nagesh et al., 1998; Carano et al., 2000; Jacobs et al., 2000 ; Ding et al., 2004). Iterative self-organizing-data analysis (ISODATA) circumvents the need for substantial user-interaction and *a priori* knowledge on the cluster distribution by introducing a number of splitting and merging steps based on inter- and intra-cluster dispersion and compactness (Nagesh et al., 1998; Jacobs et al., 2000). Studies have demonstrated the capability of ISODATA to depict lesions with a high correlation to radiological outcomes in human stroke as well as histological outcome in rodent stroke models (Ding et al., 2004; Jacobs et al., 2001a; Shen et al., 2004b). Yet, ISODATA has not been applied to a non-human primate model of stroke where histological tissue outcome can confirm the identified tissue remodeling. The current study investigated the evolutionary changes of diffusion and T_2 MRI indices after stroke in cynomologous macaques using ISODATA analysis. The first goal of this study was to identify unique temporal patterns in the acute, subacute, and chronic stages after stroke by combining

quantitative T_2 and diffusion MRI measures on a voxel-wise basis. The second part focused on characterizing spatial and temporal differences in DTI parameters between macaques with transient versus permanent MCA occlusion. The final part of this study was aimed at correlating histologically evaluated tissue fate with the MRI determined tissue signatures.

Materials and methods

Acute stroke model

All animal procedures were approved by the Subcommittee for Research Animal Care of our institution (IACUC) and the National Institutes of Health Guide for the Care and Use of Laboratory Animals. Seven adult male macaques (Macacca fasicularis, 7.7±1.2 kg, 6 to 12 years old) were subjected to focal cerebral ischemia. Ischemia was induced by obstruction of the M1 branch of the middle cerebral artery (MCA) either by injection of a small volume of cyanoacrylate mimicking a permanent MCA occlusion (MCAo) (n=2), or by insertion of a micro infusion catheter. The catheter was subsequently removed after 3 hours to effect reperfusion for a transient MCA occlusion model (n=5). Details of the surgical procedures have been previously described (D'Arceuil et al., 2006). Briefly, animals were sedated with diazepam (1 mL) then anesthesia was induced with atropine (0.04 mg/kg, i.m.) and ketamine (10 mg/kg, i.m.) and maintained with either with isoflurane (2-3%) in a 80/20 air/oxygen mixture or propofol (300 µg/kg per hour, i.v.) and remifentanil (0.1 µg/kg per hour, i.v.). Animals were mechanically ventilated with a 20% oxygen in air mixture, to maintain tidal CO_2 between 30 to 40 mm Hg, and physiological signs were monitored continuously.

MRI

Immediately after MCA occlusion serial MRI measurements were performed. All MRI data were acquired on a 1.5 T MRI-scanner (GE Signa). Diffusion tensor MRI (monopolar single-shot echo planar imaging, repetition time (TR) / echo time (TE) 8400/65.9 ms, 128 × 128 matrix, number of scans (NEX) 1, b-values of 0 and 1000 s/mm^2, 6 directions, field-of-view (FOV) 200x200x3 mm^3) , and dual echo T_2-weighted MRI (fast spin echo, TR/TE1/TE2 4200/10.7/95.9 ms, echo train length 16, 512 × 512, NEX 2, FOV 200x200x2 mm^3; 0.5 mm slice gap) were acquired up to six hours after stroke-onset according to imaging protocols previously described (De Crespigny et al., 2005). ADC-trace and FA maps were calculated on a voxel-by-voxel basis from the diffusion tensor imaging datasets (MRVision, Winchester, MA, USA); T_2 maps were calculated from the T_2-weighted images. Serial changes of the trace of the apparent diffusion coefficient

(ADC), T_2, and fractional anisotropy (FA) of the whole stroke lesions in these animals have been reported previously (Liu et al., 2007).

Data analysis

Pre-processing

Serial T_2-maps and diffusion-weighted images were spatially aligned to the b_0 image of the first time-point (1 hour post MCAo) using a two-step co-registration procedure. In the first step global alignment was achieved using a full affine, mutual information based registration procedure (MNI, Autoreg) (Collins et al., 1994). In the second step, ventricular distortions and mid-line shifts were largely compensated for using a mutual information based B-splines approach, for which the resulting deformation field was filtered to restrict the deformation in particular volumes of interest (Staring et al., 2007; Klein et al., 2010). For this study, the area identified as lesion (see below) was allowed to deform under rigid restrictions, whereas the surrounding areas were allowed to deform more freely. This prevented the lesion area from locally expanding or compressing, reducing co-registration induced artifacts.

Before cluster analysis, signal from surrounding muscle and skull tissue was removed from the MR images using the Oxford University Brain extraction toolkit (FSL BET) (Smith, 2002). Datasets were then normalized to the mean parenchymal values of the contra-lesional hemisphere. Tissue with ADC values above $1.2x10^{-3}$ mm^2/s at the first timepoint, mostly arising from CSF and larger vessels (Shen et al., 2004b, 2005), were excluded. The resulting segmentation served as a mask for further analysis.

ISODATA cluster analysis

Temporal ischemic lesion evolution was assessed using a modified iterative self-organizing data analysis (ISODATA) approach (Nagesh et al., 1998; Jacobs et al., 2000). ISODATA, an unsupervised segmentation algorithm, determines the number of clusters (K) based on the underlying data rather than by prior definition of the expected number of clusters. A detailed description of the original algorithm can be found elsewhere (Jacobs et al., 2001a). ISODATA was modified by including spatial contiguity constraints to reduce ISODATA's sensitivity to noise and outliers (Shen et al., 2004b). Spatial contiguity was employed by calculating for each image voxel the local neighborhood intensity homogeneity weighted by the distance of the neighboring voxels to the voxel in the center (Cai et al., 2007). These linear weighted images allowed for regularization of spurious outliers thereby reducing its influence on ISODATA.

ISODATA was individually applied to each animal's MRI dataset by creating for each voxel (*v*) a (*t* x *f*) dimensional feature vector; where *t* represents the number of included time points and *f* the number of features per time point. These voxel vectors were used in ISODATA to produce a normalized ISODATA map representing temporal tissue outcome.

The modified ISODATA can be summarized in the following 8 steps (see also Figure 2.1):

1. Calculation and initialization of the regularization parameters: Distance values less than a pre-specified inter-cluster boundary (Φ_C) or larger than a defined intra-cluster compactness threshold (Φ_S) will cause clusters either to be merged or split. Values for Φ_C were derived by calculating the Mahalanobis distance between contra-lesional white matter (WM) and grey matter (GM) (Jacobs et al., 2001b; Shen et al., 2004b). Φ_S was obtained by calculating the standard deviation of WM signal values over all datasets within each animal. The minimum number of voxels in one cluster was defined as Φ_N. An initial guess of the number of clusters (k) was necessary to initialize the algorithm. K defined the desired number of clusters, i.e. the resulting cluster range in which splitting and merging was allowed. Here the range was defined as $0.5*K < K < (2*K+1)$. The stopping and merging criteria were based on maximum number of iterations (*I*), convergence error threshold (ε_r), and lumping factor (L). The lumping factor specified the number of merging steps per iteration. For this study the parameters Φ_N,k,K *I*, ε_r, and L were empirically derived and set to: 100, 6, 8, 100, 0.0001, and 1, respectively, to ensure convergence of the algorithm.

2. Selection of the initial cluster means: The initial cluster means (μ_j) were selected by using a semi-randomized approach where the new cluster mean was chosen to be proportional to a randomly selected fraction of the total distance to all the previously selected cluster means (Arthur and Vassilvitskii, 2007).

3. Assignment of voxels to clusters: Voxels were assigned to the clusters where the Mahalonobis distance to the centroid was shortest.

4. Cluster pruning: Clusters with less than Φ_N voxels were discarded and their voxels were redistributed over the remaining clusters based on distance.

5. Calculation of intra- (D_{intra}) and inter-cluster (D_{inter}) Mahalanobis distances of the remaining clusters: D_{intra} is calculated as the average Mahalanobis distance

between voxel vectors and the cluster mean:

$$D_{intra} = \frac{1}{N_j} \sum_{i=1}^{N_j} \sqrt{(v_i - \mu_j)^T S^{-1}} (v_i - \mu_j)$$

With N_j the number samples and v_i the i^{th} vector of the j^{th} cluster: μ_j. S is the covariance matrix.

D_{inter} is calculated as the Mahalanobis distance between two cluster centers (μ_i, μ_j):

$$D_{inter} = \sqrt{(\mu_i - \mu_j)^T S^{-1}} (\mu_i - \mu_j)$$

6. Splitting or merging of clusters: Clusters were split or merged based on intra- and inter-cluster distances, and cluster means recalculated.

7. Stopping rule: Steps 3–6 were repeated until the convergence error was less than ε_r or the maximum number of iterations had been reached.

8. Post processing steps: pruning and cluster normalization steps are being conducted to improve interpretability of the derived clusters.

For each animal the calculated ISODATA maps were pruned using Coefficient of Variance (CoV) analysis. CoV pruning was conducted to reduce the influence of small noisy fluctuations in MR indices over time. In CoV, the ratio between a cluster's temporal standard deviation and its corresponding mean gives a measure of dispersion. A cluster with dispersion larger than 0.05 was considered abnormal; clusters with less dispersion were merged into the normal tissue cluster. In the end, ISODATA maps were standardized by assigning the cluster of cerebrospinal fluid (CSF) to 100 and the cluster of contra-lateral white matter to 1. The remaining clusters were assigned normalized cluster values between 1 and 100 depending on the difference of each cluster's mean centroid and those of the CSF or contra-lateral white matter (Soltanian-Zadeh et al., 2003).

For group comparisons, global evolution profiles or signatures were obtained by binning signatures according to their normalized values. Values below 5 or above 95 were considered normal or CSF respectively. Remaining signatures were binned in steps of 10. Values deviating no more than 5 from a multiple of 10 ($x-5 < x < x+5$; $x = \{10, 20, .., 90\}$) were binned as one signature.

Relative ADC (rADC), FA (rFA) and T_2 (rT_2) maps were calculated by dividing each map by its mean contralateral hemispheric value. Temporal patterns of relative values for each of the global signatures were examined and compared.

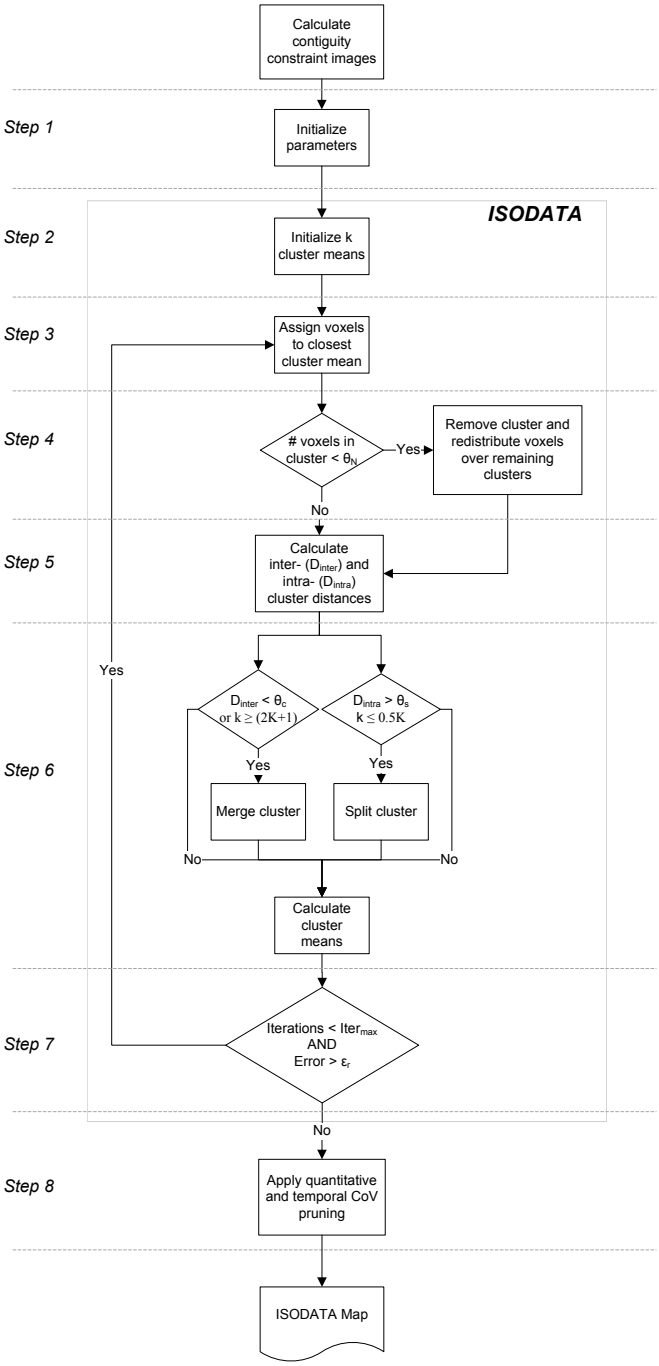

Figure 2.1. *Flowchart of the 8 step clustering procedure for the modified ISODATA*

Statistical analysis

At each timepoint, lesion volumes were manually outlined on ADC maps for the acute timepoints (<6 hours), or on T_2 maps for the subacute through chronic timepoints by two experienced researchers. Both researchers were blinded to the ISODATA results. Volumes of abnormal tissue signatures as indicated by ISODATA were obtained after excluding normal (<5) and CSF tissue (>95) from the ISODATA maps.
Four tissue classes were operationally defined as: '*Core*', '*Growth*', '*Recovery*', or '*Edema*'. The manually outlined 1 hour ADC lesion was used to define *Core* voxels. Voxels that were abnormal on the 17-day T_2 data, but normal on the acute ADC data were defined as a lesion *Growth* region. Voxels with abnormal values in the acute stage, but normal at 17 days, were marked as lesion *Recovery* regions. Areas of *Edema* were defined as regions that appeared abnormal at the time-point of maximum T_2 lesion volume ('*Maximal Lesion*'), but were normal at both acute and chronic time points (Figure 2.2). All remaining voxels were classified as normal tissue.

Wilcoxon signed-rank sum test was used to test CoV value differences. Distribution of tissue signatures in *Core*, *Growth*, *Recovery*, and *Edema* tissue classes were compared using Pearson's chi-square test. Linear regression analysis was used to determine differences between temporal signatures. Values are reported as mean±sd unless otherwise noted. $P<0.05$ was considered significantly different.

Histological Brain Tissue Preparation and Analysis Methods

Animals were euthanized by an intravenous overdose of sodium pentobarbital at 30 days post stroke onset with the exception of one animal that was sacrificed earlier (17 days). Brains were immediately removed and fixed with 10% formalin followed by gross sectioning of the brains into 2.5 mm blocks, to closely match the MRI slice thickness and orientation. Coronal blocks were embedded in paraffin and consecutively sectioned into 6 μm thick slices from the cut face through the entire lesion area. Successive slices were routinely stained with hematoxylin and eosin (H&E) and luxol fast blue (LFB). Stained consecutive sections were scanned (Epson ® Perfection 3170 Photo Scanner Epson America, Miami FL), and pictures were digitally stored. A template of the brain showing the boundaries of the affected regions and the outline of the brain was manually traced on the pictured sections. The stained sections were examined and rated by an experienced primate neuropathologist (S.W.). Additionally, corresponding histological tissue features were identified for abnormal areas identified by ISODATA clustering on MRI slices.

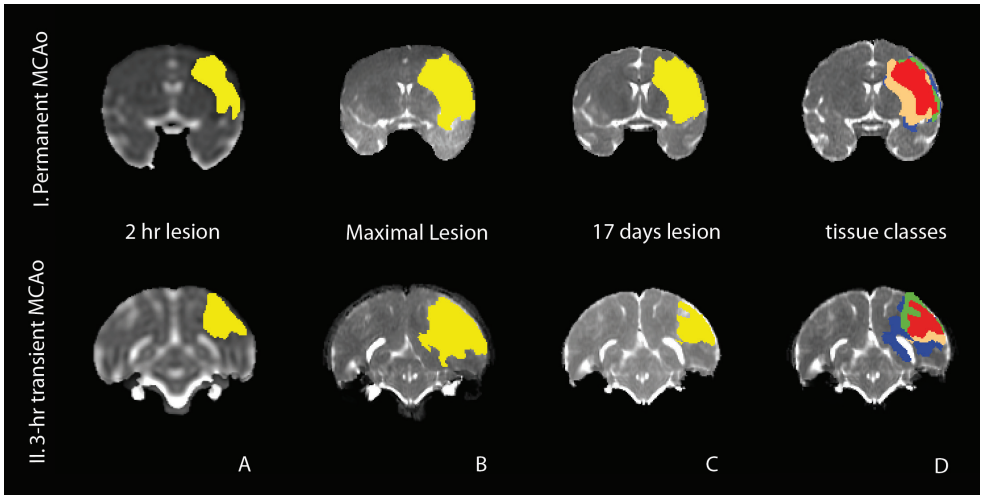

Figure 2.2. *Temporal-evolution maps (coronal view) from the brains of two macaques that were subjected to (I) permanent or (II) 3 hour transient MCAo. Manually outlined regions-of-interests of ADC-derived lesion volume at 2 hours (I.A and II.A); T_2-derived lesion at 72 (I.B) or 144 hours (II.B); and T_2-derived lesion at 408 hours (I.C and II.C) follow-up, subdivided in four operationally defined tissue classes (I.D and I.D). Voxels that were abnormal acutely (A) and at follow-up (C) represented Core (D: red); voxels abnormal at follow-up (C), but normal at the acute stage (A) were considered Growth areas (D: copper); voxels abnormal in the acute stage (A), but normal at 17 days follow-up (C) represented Recovery regions (D.I: green); and voxels transiently abnormal at the time-point with maximum lesion volume (B), but normal at acute (A) and chronic (C) stages were considered areas of Edema (D: blue)*

Results

Stroke Model

Seven macaques were earmarked for this study but datasets from only four animals were analyzed with ISODATA. Three animals from the transient MCA-occlusion group were excluded: one animal due to incomplete occlusion; data from the second animal was severely contaminated with eddy-current artifacts that could not be corrected and therefore this dataset was unsuitable for voxel-wise analysis; a third animal was excluded because data at the hyperacute timepoint was not acquired due to MR scanner equipment problems. For the remaining animals, serial DTI and T_2 studies were used for ISODATA analysis from data collected at approximately 1 hour (1.33±0.30 hours), 2 hours (2.41±0.44 hours), 3 hours (3.04±0.44 hours), 24 hours (23.34±1.57 hours), 72 hours (70.26±1.54 hours), 144 hours (142.18±1.83 hours), and 240 hours (232.22±9.92 hours) after stroke onset. These time points were selected since DTI datasets were available for all animals. For "final" lesion volumes, the 17-day (406.98±2.31 hours) T_2 maps were used. One animal (M3802) died before the 17-day follow up (day 11); in that

case the 240 hours data was used instead.

Tissue Classifications

The distribution of voxels between *Core*, *Growth*, *Recovery* and *Edema* tissue classifications was significantly different between permanent and transient MCAo groups ($P < 0.001$) (Figure 2.3). In the permanent MCAo group, 48% of the abnormal tissue voxels were assigned to the lesion *Core*, whereas in the transient MCAo group this was 14% ($P=0.07$). In the latter group, the lesion volume was dominated by *Edema*, with 58% of the voxels, which was significantly more compared to 12% in the permanent MCA occlusion group ($P=0.002$). Regions of *Growth* were somewhat larger in the permanent than in the transient MCAo group: 35% versus 14% ($P=0.1$), respectively, whereas *Recovery* volumes were significantly larger in the transient MCAo group (14% as compared to 5% in the permanent MCAo group; $P=0.02$).

ISODATA-based Tissue Signatures

For ISODATA, Φ_C and Φ_s were set to 0.98 ± 0.34 and 0.52 ± 0.03, respectively; this resulted in 12 to 17 clusters per animal. Subsequent thresholding and CoV pruning reduced the number of clusters to 2 to 6 per animal. The CoV of normal tissue was significantly lower than that of selected abnormal tissue (0.0060 ± 0.11 vs. 0.18 ± 0.46, $P<0.01$). Table 2.1 shows the lesion volumes for the 4 animals across time along with the ISODATA volumes.

Figure 2.4 shows examples of acute (1 h) and 240 hour MRI datasets (a-d) from an animal (M103) with a permanent MCA occlusion (I) and an animal with a 3 hour transient MCA occlusion (I: M403). ADC (Figure 2.4a), FA (Figure 2.4b), and T_2 (Figure 2.4c, d) maps were combined over the 7 different time points resulting in a 7x3-dimensional matrix. This matrix was used in the modified ISODATA method producing normalized ISODATA maps (Figure 2.4e). In these maps, dark colors represent normal tissue and brighter colors abnormal tissue. The resulting cluster patterns of each animal were pooled to create six signatures with significantly different temporal patterns ($P<0.01$) (Figures 2.4f and 2.5). One signature was consistent with normal tissue while the other five indicated varying degrees of tissue abnormalilty. There was significant ventricular distortion in the contra-lateral hemisphere of the brain of one animal (M3802) from the permanent occlusion group. Voxels in the ipsi-lateral hemisphere were assigned lower values than voxels within the distortion, therefore this hemisphere was excluded from analysis by using a manually derived upper threshold (cluster value > 54). Signature I was the result of pooling clusters 5-15, Signature II from clusters 25-35, Signature III from clusters 35-45, Signature IV from clusters 45-55, and Signature V from clusters 55-65. There were no more clusters with values higher than 65. Signature N was

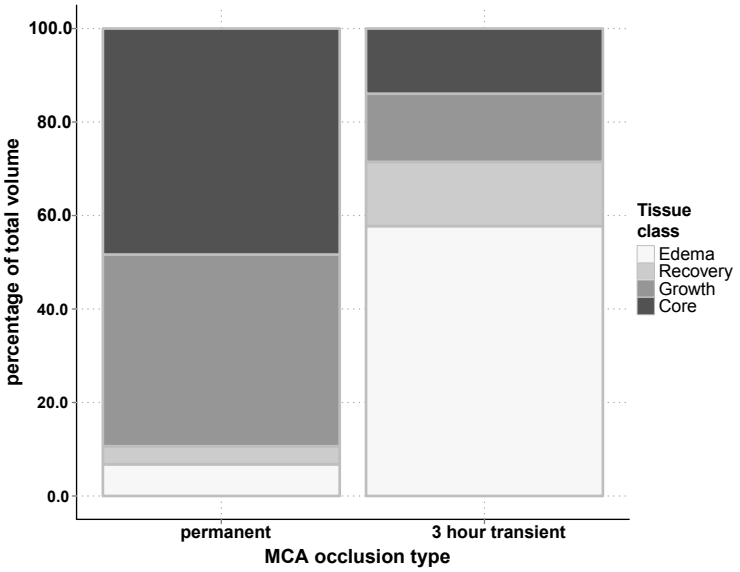

Figure 2.3. *Percentage distribution of four defined tissue classes with respect to the total lesion volume of the permanent and 3 hour transient MCA occlusion group. In the permanent occlusion group Core was the predominant lesion tissue classification accounting for 48 % of the total abnormal area. 41% of the voxels were initially normal but were abnormal at 17 days (Growth). Recovery and Edema areas only contributed slightly to the final lesion volume, 4% and 7% respectively. For the transient MCA-occlusion group, Edema was the predominant component, constituting 58% of the lesion voxels, significantly more than in the permanent MCA-occlusion group (P=0.002). Similar holds to true for Recovery (P=0.02), which was together with Core and Growth more equally distributed, where each made up 14% of the total abnormal tissue voxels.*

Table 2.1. Abnormal tissue (lesion) volumes from 1 hour (acute) up to 408 hours (chronic) after stroke onset, and ISODATA assigned abnormal tissue volumes in the four macaques.

	Permanent MCAo		3 hour transient MCAo	
	M103	M3802	M403	M303
1 hours	2.32	5.39	1.51	0.15
24 hours	2.52	9.43	3.25	0.16
72 hours	**3.87**	**10.06**	3.38	**0.18**
144 hours	3.74	9.80	**5.52**	0.16
240 hours	3.46	9.72	2.23	-**
408 hours	2.21	-*	1.65	0.05
ISODATA	3.23	9.95	5.51	0.15

Volumes are expressed in mL. Bold numbers indicate largest tissue lesion volumes ('Maximal Lesion'). *Died before 17-day follow-up; 10-day follow-up used instead. **T_2 not available.

defined as normal tissue (clusters 1-4).

The five identified abnormal signatures showed differentiation between fast rising relative rADC in the first 24 hours (Signatures I and IV) as opposed to a reduction in rADC in the first 24 hours for Signatures II, III, and V (Figure 2.5). Signatures III and V exhibited the largest rADC reduction. After 24 hours a slowly increasing trend of rADC towards pseudo-normalization was observed in Signatures II and III. Signatures I and IV showed a slow descent, whereas Signature V showed a progressive increase in rADC. Decreased values in acute rFA was only observed for Signature V. However, all signatures showed a decreasing trend in rFA, which normalized for Signatures V and IV from 144 to 240 hours. This normalizing trend could also be noted for rT_2. For Signatures I, III, and IV, a subacute increase in rT_2 was followed by a gradual decrease from 144 hours until 240 hours. The rate of increase in rT_2 was steeper for Signature IV after 3 hours compared to the other signatures. rT_2 for Signature I was almost normal values by 240 h. Signature II showed progressive increase in rT_2. Signature III showed progressive increase in rT_2, until stabilizing at 72 h.

The distribution of the six ISODATA signatures were significantly different among the four tissue classes for both transient and permanent MCAo groups ($P<0.001$) (Figure 2.6). Signature distributions were also found to differ significantly by occlusion type ($P<0.001$). Signatures II and III were predominantly identified in the permanent MCAo group while Signatures IV and V were identified in the transient MCAo group. In one animal (M403), Signature I was found almost exclusively in areas of Edema (98.8%), with some voxels in regions of Growth (0.1%) and Recovery (1.1%). In contrast to transient MCAo animals, Signature IV was found only in one permanent MCAo animal, again predominantly in regions of Edema (46%), and to lesser extent in regions of Core (23%), Growth (20%) and Recovery (12%) (Figure 2.7).

Histological Features

H&E and LFB-stained brain sections from all cases were analyzed with particular attention given to regions identified by Signatures I through V. Brain lesion characteristics from each available signature area from the four macaques are summarized in Table 2.2. Histopathological alterations in the brain included extensive necrosis with brain tissue loss and cavitation; axonal swelling; astrogliosis; edema and spongiosis; vascular proliferation; and infiltration of foamy macrophages or gitter cells with phagocytized necrotic debris. In the permanent MCAo animals, Signature II was primarily found in gray matter areas (central, supra marginal and temporal gyri) and corresponded to the most severe lesions with areas of extensive necrosis, tissue loss, dead neurons, and gitter cells (Figure 2.8.I). Signature III was detected solely in permanent MCAo animals

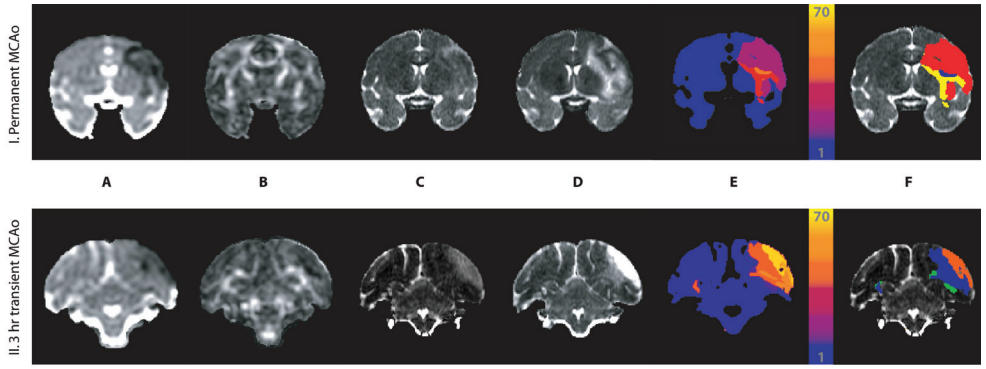

Figure 2.4. *Set of coronal brain slices from macaques after permanent (I) or 3 hour transient MCAo (II). Quantitative ADC (A), FA (B), and T_2 (C) maps at 3 hours after stroke induction, and 10-day follow-up T_2 maps (D) are shown. For each animal the quantitative maps from 1 hour up to 10 days after stroke onset were combined and clustered using a modified ISODATA approach resulting in a normalized (1-100) ISODATA-map (E). ISODATA-maps indicating abnormal tissue were obtained after thresholding the normalized maps between abnormal values (above 5 and below 95) and normal values. Binning of the signatures resulted in five abnormal signatures (F). Color coding: Green: Signature I; Red: Signature II; Yellow: Signature III; Blue: Signature IV; Orange: Signature V. For visualization purposes ISODATA-maps were scaled between 1 and 70. Normalized values were never larger than 70 since CSF was excluded from the analysis.*

in areas of white matter (external capsule, and precentral and temporal white matter) and gray-white matter junction (parietal and temporal cortices). These regions showed areas of neuronal injury with features of degenerating neurons and axons, but absence of gitter cells. Parietal temporal white matter was also affected in Signatures IV and V defined volumes. Signature IV corresponded to a prominent border region between infarcted and surviving tissue with vascular proliferation, spongiosis, and astrogliosis. These histological changes were found in both permanent and transient MCAo animals. Astrogliosis along with some neuronal mineralization and edema were also observed in Signature I, present in only one transient MCAo animal (Figure 2.8.II).

Discussion

In this study, T_2 and diffusion (ADC, FA) MRI indices acquired at acute, subacute, and chronic stages after stroke were combined on a voxel-wise basis to identify unique spatiotemporal MRI profiles, and to determine differences in stroke evolution after permanent or transient MCAo in non-human primates. A modified ISODATA approach identified six distinct tissue signatures. One signature revealed no substantial changes in T_2, ADC, and FA over time, and was therefore assumed to represent unaffected normal tissue. The five other signatures showed substantial differences from this normal signature. These abnormal signatures exhibited differences in distribution as well as

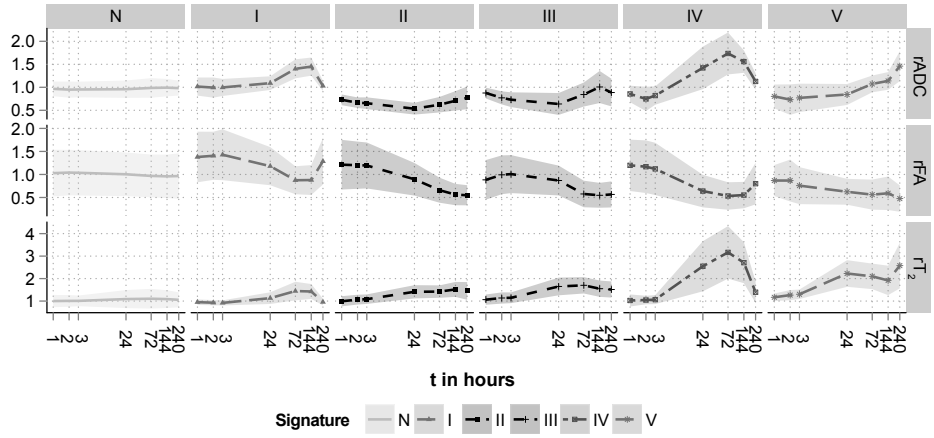

Figure 2.5. *Plots of mean ADC (a), FA (b), and T_2 (c), normalized to the mean contra-lateral values (rADC, rT_2 and rFA) and plotted against time after stroke onset. ISODATA identified one normal (N) and five abnormal signatures (I-V). Two signatures (I, IV) showed a sharp increase of rADC from initially decreased values which slowly decreased towards normal values around 240 hours post-stroke. This pattern of initial increase and subsequent normalization is also noted for rT_2, an evolution similar to Signature V. Here, however, increased values were sustained at 240 hours post-stroke. Sustained increase in rT_2 and rADC was also present in Signatures II and III. Yet, these signatures showed a slower increase towards rADC pseudo-normalization, with values of Signature II remaining decreased at 240 hours post-stroke. rFA values were characterized by an initial increase followed by normalization (Signature I), or a progressive drop to below normal values (Signatures II and IV). Signatures III and V showed similar evolution to Signatures II and IV, but starting from initially slightly reduced values. The shaded ribbon represents the standard deviation from the mean.*

temporal profile depending on whether the occlusion was permanent or transient, the brain location, and the level of neuronal damage.

Regional analysis

A previous macaque study of relative volume evolution for transient versus permanent MCAo brains revealed changing patterns similar to those found in the present study (Liu et al., 2007). That study reported substantial variations in lesion volumes particularly around 1-6 days after stroke. The smaller subset of animals in our ISODATA voxel-based study revealed that the largest lesion sizes were detectable at 3 or 6 days after stroke based on the ADC or T_2-based manual volumetric analysis. Subdivision of these MRI-based abnormal volumes in four different tissue classifications identified most severe neuronal damage in the permanent MCAo group with large areas of *Core* and *Growth* tissue, which were smaller in the transient MCAo group. This latter group held less severe neuronal damage with larger areas of *Recovery* and *Edema*. Yet, histological assessment revealed different stages of tissue remodeling in these tissue classes which

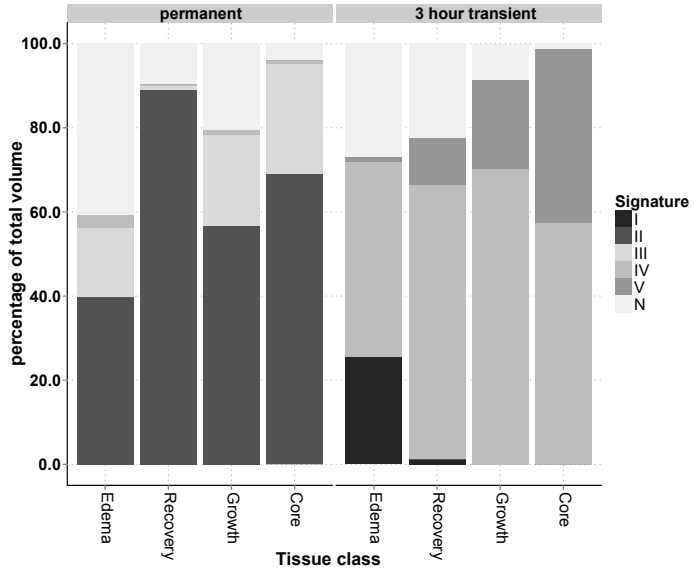

Figure 2.6. *Percentage distribution of the temporal tissue signatures over four tissue classifications. The tissue classes were subdivided in multiple signatures. In the permanent MCAo group most of the tissue classes were made up out of Signatures II and III. In the transient MCAo group Signature IV mostly made up the tissue classes.*

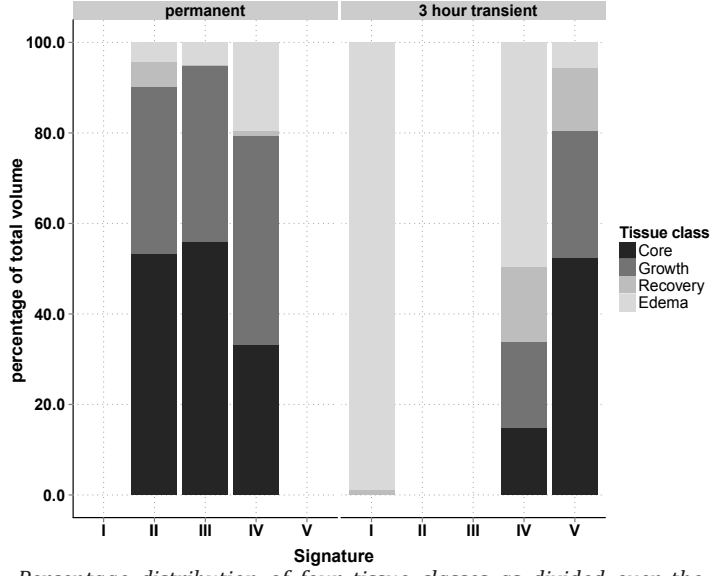

Figure 2.7. *Percentage distribution of four tissue classes as divided over the five abnormal signatures. The signatures were distributed differently over both MCAo groups (P<0.001). Signatures II and III mostly dominated Core and Growth volumes in the permanent MCAo group. In the transient MCAo group this was observed for Signature V. Where in the permanent MCAo group Signature IV covered 20% of the Edema area, this coverage was larger in the transient MCAo group (46%). Nevertheless, Signature I corresponded mostly with the Edema type in the transient MCAo group (99%).*

Table 2.2: Histological characteristics of the brains of the four macaques

	Permanent MCAo		3 hour transient MCAo	
	M103	M3802	M303	M403
I	NA	NA	NA	edema, spongiosis, astrocytosis, mineralization
II	marked necrosis with dead neurons, tissue loss with gitter cells	marked necrosis with dead neurons, tissue loss with gitter cells	NA	NA
III	degenerate neurons, degenerate axons (spheroids)	degenerate neurons, degenerate axons (spheroids)	NA	NA
IV	spongiosis, vacuolation, astrogliosis, vascular proliferation	NA	NA	spongiosis, vacuolation, astrogliosis, vascular proliferation
V	NA	NA	edema, necrosis, gitter cells	edema, necrosis, gitter cells

NA: not applicable

was also exhibited by the ISODATA derived tissue signatures.

In the light of ongoing debates on the utility of single acute MRI parameters such as T_2 (Wegener et al., 2006; Siemonsen et al., 2009, 2012), ADC (Li et al., 2000, 2002; Kaur et al., 2009), or FA (Bhagat et al., 2006; Pitkonen et al., 2012) for predicting tissue infarction, the merits of using complementary multiparametric MRI measures on a voxel-wise basis have been previously illustrated in rodent models (Jacobs et al., 2000, 2001a; Shen et al., 2004b; Wu et al., 2007) and in human studies (Jacobs et al., 2001b; Mitsias et al., 2002; Wu et al., 2001, 2006). Temporal tracing of tissue fate was previously accomplished either by manually connecting voxels over multiple timepoints (Shen et al., 2004b, 2005; Shen and Duong, 2008), or by scaling each voxel's value compared to presumptive normal tissue values (Soltanian-Zadeh et al., 2003; Ding et al., 2004; Li et al., 2005). However, it may be challenging to link the result of these approaches to underlying biological processes (Shen et al., 2004b). Here a modified ISODATA approach

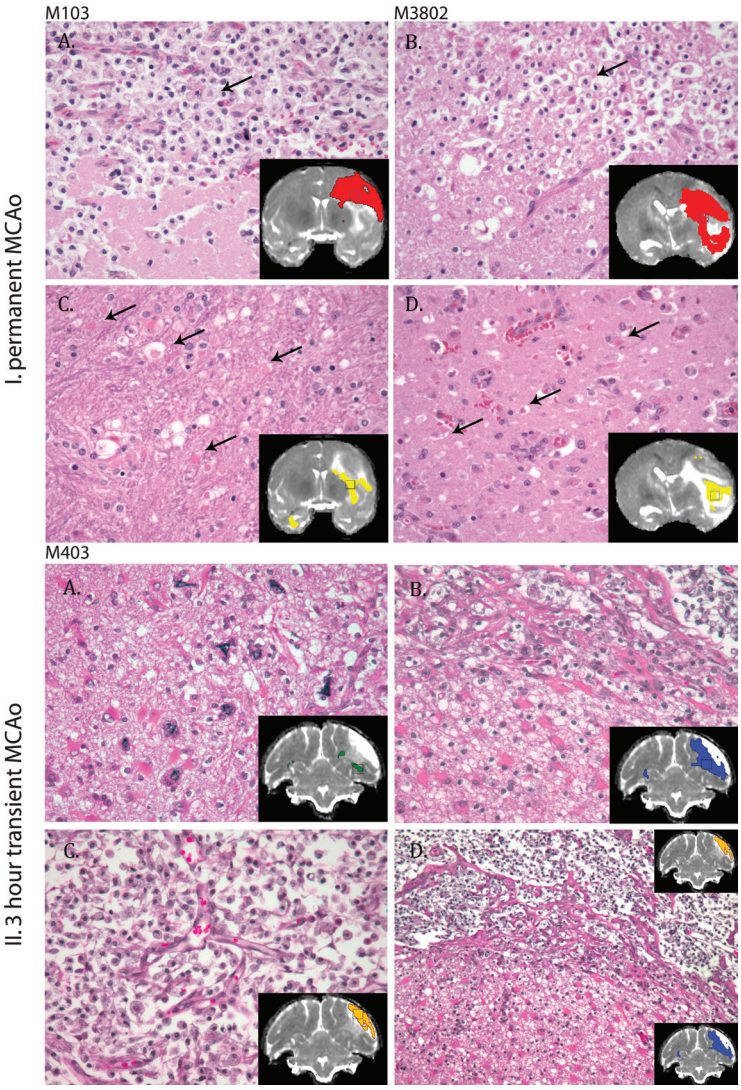

Figure 2.8. *H&E stained brain sections from animals with permanent (M103: I.A, C and M3802: I.B, D) or 3 hour transient (M403: II.A-D) MCAo. Insets display the 10-day T_2 MRI with overlays of Signatures I (green), II (red), III (yellow), IV (blue), and V (orange), and a squared box indicating the area of the microscopic fields. In permanent MCAo, most severe tissue injury was observed in Signature II regions (I.A, B) that corresponded with severe tissue necrosis and tissue loss, large amount of macrophages (gitter cells) and some remaining vasculature. Neuronal and glial injury and degeneration in the peri-lesional brain regions corresponded with Signature III, and included degenerated axons (spheroids, I.C, arrows) and hypereosinophilia of dying neurons (I.D, arrows). In transient MCAo Signature I (II.A) corresponded with areas with peri-lesional neuronal mineralization and astrogliosis. Signature IV (II.B) corresponded with brain regions with vascular proliferation, spongiosis, and marked astrogliosis. Signature V (II.C) corresponded with brain regions with necrosis and infiltration of gitter cells. The border region between Signatures IV and V is displayed in lower magnification in II.D (10 times). Original magnification 20x (I.A-D; II.A-C).*

included a spatial component that allows for concurrent spatial and temporal modeling of the MRI parameters, followed by a temporal pruning and global merging step. CoV pruning was introduced under the assumption that stroke induced temporally evolving patterns, including patterns of unaffected tissue remaining constant, or temporally highly varying patterns representing artifactual noise (Carano et al., 2000; Li et al., 2000). Further, all the datasets were merged across animals in order to better identify tissue with common temporal profiles, based on the assumption that these areas would also exhibit similar histological outcome. One might question whether the coefficient of variance and the "intra-dataset" signature merging steps, both fully automated and parameter adjustable, may oversimplify or obscure additional tissue profiles. However, we identified biologically interpretable MRI signatures that corresponded with specific features of tissue damage as verified with histology.

Tissue signatures

Differences in temporal evolution of signatures classified as abnormal may be exploited to differentiate the varying degree of neuronal damage (Zhang et al., 1994; Knight et al., 1994; Carano et al., 2000; Wegener et al., 2006; Liu et al., 2007; Siemonsen et al., 2009; Pitkonen et al., 2012; Hui et al., 2012). The most severe damage, characterized by a substantial amount of tissue necrosis and the presence of gitter cells, was assigned to Signatures II and V – signatures representing acutely decreased ADC combined with normal T_2, followed by progressively increased ADC and T_2 during the subacute and chronic stages of stroke. Yet, the temporal profiles of these two signatures showed different timings. In Signature V (limited to the transient MCAo group), ADC renormalization and T_2 increase started within 24 hours, i.e. almost immediately after reperfusion (at 3 hours), whereas in Signature II (found only in permanent MCAo group) these processes were observed after 24 hours. ADC normalization may be instigated by reperfusion. Reperfusion reinstates energy metabolism and ion-pump function effecting permanent or transient reversal of ADC (Li et al., 2000, 2002; Simard et al., 2007; Kaur et al., 2009), or alternatively aggravate blood-brain-barrier disruption resulting in an influx of extracellular water along osmotic gradients resulting in vasogenic edema (Menzies et al., 1993; Knight et al., 1994). Along with the increased T_2, the rapid increase of ADC hints toward increased vasogenic edema (Knight et al., 1994; Van Dorsten et al., 2002; Hui et al., 2012; Pitkonen et al., 2012). In addition, differences in ADC pseudo-normalization may be associated with differences in the time of maximal accumulation of neutrophils in permanent versus transient vessel occlusion (Zhang et al., 1994).

In Signature IV (found in the permanent and transient MCAo groups), increase of ADC and T_2 were prominent and initiated shortly after reperfusion followed by a gradual renormalization after 10 days. Yet, histopathology after 30 day revealed the presence of

a glial scar and the presence of tissue remodeling indicated by angiogenesis and astrogliosis. Although debates on the reliability of MRI metrics (particularly T_2 values) as surrogates for actual tissue damage are open-ended (Knight et al., 1994; Siemonsen et al., 2009, 2012)), an apparent T_2 normalization and potential subsequent re-elevation may aid in differentiating selective neuronal necrosis from pannecrotic damage (Weber et al., 2005; Wegener et al., 2006). Signature IV may therefore hold valuable information on long-term tissue remodeling and may possibly be regarded as a pre-cursor for delayed tissue damage.

Acute, increased rFA values were observed in three out of five abnormal signatures, the other signatures either were initially normal (Signature III) or slightly reduced (Signature V). Yet, increased rFA values were never observed beyond 24 hours. This observation may reflect initially preserved cytoarchitecture or increased extracellular space tortuosity as a result of cytotoxic edema that subsequently gradually decays as ischemia progresses towards tissue necrosis (Pierpaoli et al., 1993; Green et al., 2002; Munoz Maniega et al., 2004; Pitkonen et al., 2012). Further differences may be associated with different levels of cell swelling in white or gray matter structures (Knight et al., 1994; Sorensen et al., 1999a; Munoz Maniega et al., 2004; Hui et al., 2012; Pitkonen et al., 2012). In our study, differences in gray and white matter were not extensively examined, yet Signature V (reduced rFA) was primarily observed in areas of cortical gray matter. Signature III (relatively normal FA) was limited to areas of temporal white matter and external capsule. However, increased FA was observed in areas of the cortical gray matter (Signature II) as well as in temporal and parietal white matter (I, IV).

Noticeable was also the resolution of decreased FA (along with ADC and T_2) in the chronic phase after transient MCA occlusion (Signatures I and IV). While renormalization of T_2 may be associated with resolution of edema (Dijkhuizen and Nicolay, 2003), recovery and subsequent progressive increase of diffusion anisotropy has been associated with processes of remyelination (Jiang et al., 2006; Ding et al., 2008) or axonal sprouting (Jiang et al., 2006; Ding et al., 2008; Li et al., 2009). Yet, other studies speculated glial scar formation as a contributing factor to FA normalization (Wegener et al., 2006; van der Zijden et al., 2008). Signatures I and IV, marking relative normalization of the FA, were associated with areas of astrogliosis, seemingly corroborating the latter.

The limited number of animals included in this study precludes generalization of specific MRI tissue signatures heralding histological tissue damage. Nevertheless this study shows the applicability and potential of MRI-based algorithms, validated with histology, to further characterize tissue progression after stroke. The spatio-temporal assessment of different MRI parameters enabled us to distinguish distinct evolutionary tissue patterns that held specific histological outcome. In the future, this type of multiparametric MRI analysis should be validated on larger cohorts of animals to

establish robust categories of tissue signatures. It may further open opportunities for improved comprehension of treatment induced changes – for which induced changes may be represented by new and unique temporal profiles (Ding et al., 2004; Li et al., 2005, 2007) - potentially providing an additional tool to optimize the translation of experimentally obtained findings into human stroke applications.

3

Lesion development and reperfusion benefit in relation to vascular occlusion patterns after embolic stroke in rats

Mark J.R.J. Bouts[1], Ivo A.C.W. Tiebosch[1], Annette van der Toorn[1], Jeroen Hendrikse[2], and Rick M. Dijkhuizen[1]

[1] Biomedical MR Imaging & Spectroscopy Group, Image Sciences Institute, University Medical Center Utrecht, Utrecht, The Netherlands.
[2] Radiology department, University Medical Center Utrecht, Utrecht,The Netherlands.

Submitted for publication

Abstract

The site of vascular occlusion is an important factor in development of cerebral tissue damage after acute ischemic stroke, and it may also affect the likelihood of subsequent reperfusion. Our goal was to determine the relationship between flow obstruction in different segments of the Circle of Willis, and 1) the profile of acute ischemic lesions and 2) the probability of subsequent beneficial reperfusion.

Embolic stroke was induced by unilateral blood clot injection in the internal carotid artery (ICA) in normotensive (n=55) or spontaneously hypertensive (n=20) rats. MR angiography (MRA), and diffusion- (DWI) and perfusion-weighted MRI (PWI) were performed within 2 h after middle cerebral artery (MCA) occlusion to identify the vascular occlusion pattern, and associated acute cerebral tissue and perfusion lesions. MRI was repeated after 24 and 168 h to determine the predictive value of the occlusion pattern on benefit of spontaneous or thrombolysis-induced reperfusion in a subset of animals (n=13) without further lesion growth.

The extent of cortical and subcortical perfusion and diffusion abnormality was related to the pattern of flow obstruction in segments of the ICA and MCA. Hypertensive animals displayed significantly larger cortical perfusion lesions. Acute perfusion-diffusion lesion mismatches were detected in all animals that subsequently benefited from reperfusion. However, presence of an angiography-diffusion mismatch was more specific in predicting reperfusion benefit.

Combination of DWI, PWI and MRA can provide exclusive information on the impact of arterial occlusion profiles after acute ischemic stroke, which may improve prognostication and subsequent treatment decisions.

Introduction

Early assessment of cerebrovascular impairment, and prediction of outcome are crucial for adequate management and treatment of patients suffering from acute ischemic stroke. Acute magnetic resonance imaging may play a key role in early diagnosis and subsequent treatment planning. (Olivot and Marks, 2008; Wardlaw, 2010) In particular, diffusion-weighted imaging (DWI), which is a highly sensitive method to detect early ischemic tissue damage (Hjort et al., 2005a), and perfusion-weighted imaging (PWI), which enables measurement of hemodynamic disturbances, are valuable tools for acute stroke diagnosis. (Albers et al., 2006; Hacke et al., 2009; Schellinger et al., 2010) Tissue amenable for thrombolytic treatment may be identified from a volumetric mismatch between brain areas with reduced tissue diffusion and perfusion, i.e. the perfusion-diffusion mismatch. (Hacke et al., 2009) Identification of a perfusion-diffusion mismatch may aid in selecting patients who could benefit from thrombolytic therapy beyond the currently set treatment time-window of 4.5 h after stroke onset. (Marks et al., 2008; Copen et al., 2009; Lansberg et al., 2009) However, the perfusion-diffusion mismatch may also overestimate the area of tissue at risk of infarction (Kidwell et al., 2003; Sobesky et al., 2005; Davis et al., 2008) or exclude potentially salvageable tissue. (Sobesky, 2012) Moreover, lack of clear standards for image acquisition, post-processing and analysis to define the perfusion-diffusion mismatch, complicates its use as a robust measure in clinical settings.

A major factor in the development of a cerebral ischemic lesion is the location and extent of vessel occlusion. Angiography-based detection of the site of arterial flow obstruction may significantly aid in early diagnosis and treatment planning. Along these lines, the concept of a MR angiography-diffusion mismatch has recently been introduced, which indicates the presence of intracranial vessel occlusion or stenosis on MRA and a relatively small lesion on DWI. (Lansberg et al., 2008) The MR angiography-diffusion mismatch represents the tissue without diffusion abnormality within the vascular territory of the occluded artery, i.e. tissue at risk. However, it has been argued that the concept of a MR angiography-diffusion mismatch disregards the compensatory mechanisms of collateral flow from other feeding arteries (Schellinger and Köhrmann, 2008; Kim et al., 2009), since presence of adequate collateral supply may maintain perfusion distal to an occlusion site. (Liebeskind, 2003) As such, the MR angiography-diffusion mismatch may overestimate tissue at risk of infarction, which could lead to unnecessary exclusion of patients from reperfusion therapy. (De Silva et al., 2010) Clinical studies based on MRA, PWI, and DWI in acute ischemic stroke patients have described a relation between the site of arterial occlusion and the size of cerebral lesions, and speculated on the role of collateral flow. (Kim et al., 2009; Cheng et al., 2011) However the exact relation of acute

ischemic stroke mismatch patterns as detected with MR angiography, PWI and DWI, and their potential to predict recovery following reperfusion remains to be elucidated.

Therefore we designed an experimental study in which acute embolic stroke was induced in normotensive rats, and in chronically hypertensive rats with impaired collateral flow (Coyle and Heistad, 1986; Coyle, 1987) to 1) define the pattern of occlusion of segments of the Circle of Willis, as measured with MRA, and associated development of acute ischemic lesions, as measured with DWI and PWI, and 2) establish the abilities of the MR angiography-diffusion and perfusion-diffusion mismatch concepts to predict benefit from reperfusion.

Materials and methods

Experimental stroke model

All animal procedures were approved by the Utrecht University Ethical Committee on Animal Experiments. Details on the surgical procedures are described elsewhere. (Zhang et al., 1997; Tiebosch et al., 2012) Briefly, right-sided unilateral stroke was induced in normotensive male Wistar rats (normotensive group; n=82, 341±39 g) (Harlan, The Netherlands) or spontaneously hypertensive Wistar-Kyoto rats (hypertensive group; n=24, 303±21 g) (Charles River, Germany) by intracarotid injection of a homologous blood clot - obtained 24 h prior to stroke induction - near the bifurcation of the internal carotid artery (ICA) and middle cerebral artery (MCA).
A subset of animals received recombinant tissue-plasminogen activator (rt-PA (Actilyse®, Boehringer Ingelheim, Alkmaar, The Netherlands, 3.0 mg/ml)) (6 normotensive and 3 hypertensive rats) or saline (7 normotensive and 2 hypertensive rats) immediately after the first MR imaging session (see below), i.e. ca. 2 h after stroke onset.
Animals were included for this study if MRA, DWI and PWI (see below) were acquired within 2 h after stroke onset, and if acute tissue and perfusion lesion volumes were larger than 1 mm^3. For assessment of reperfusion benefit in the subset of rats that underwent follow-up MRI, we only included animals that demonstrated effective reperfusion at 24 h after stroke, defined as a CBF increase of more than 30% from the value in the acute perfusion lesion.

MR angiography and imaging

MRI was conducted on a 4.7T scanner (Varian, Palo Alto, CA, USA) immediately after stroke induction, and repeated at 24 and 168 h post-stroke onset in animals that were

treated with rt-PA or saline. During MRI, animals were continuously mechanically ventilated with 2% isoflurane in an air:O_2 (2:1) mixture. Animals were restrained in a MRI-compatible holder with earplugs and a tooth-holder. Body temperature was maintained at 37.5 ± 0.5 ˚C, and expired CO_2 levels were monitored and kept within physiological range by adjustment of ventilation parameters when necessary. A 90 mm diameter in-house developed Helmholtz volume coil was used for radiofrequency excitation, and a 25 mm diameter inductively coupled surface coil for signal reception. MRA was executed with a flow-compensated 3D time-of-flight sequence (gradient echo; repetition time (TR) 15 ms; echo time (TE) 2.66 ms; field-of-view (FOV) 32 x 32 x 32 mm3; data matrix size 128 x 128 x 128).

For all MRI acquisitions FOV was set to 32 x 32 mm^2, with 1 mm slice thickness. The MRI protocol consisted of multiple spin-echo T_2-weighted images (TR 3600 ms; TE 12-144 ms; data matrix size 256 x 128 x 19) for reconstruction of quantitative T_2 maps by non-linear least square fitting. Maps of the apparent diffusion coefficient (ADC) were calculated from diffusion-weighted 8-shot echo planar imaging (EPI; TR 3500 ms; TE 38.5 ms; b-values 0 and 1428 s/mm^2; 6 diffusion-weighted direction; data matrix size 128 x 128 x 19). Dynamic susceptibility contrast-enhanced (DSC) MRI was executed with gradient echo EPI (TR 330 ms; TE 25 ms; data matrix size 64 x 64 x 5) in combination with an intravenous bolus injection of 0.35 mmol/kg gadobutrol (Gadovist®, Schering, The Netherlands). Maps of the cerebral blood flow (CBF), cerebral blood volume (CBV), mean transit time (MTT) and bolus peak time (T_{max}) were subsequently acquired by circular deconvolution of the tissue concentration curves with an arterial reference curve obtained from the contralateral hemisphere. (Wu et al., 2003)

Image processing and analysis

For group comparisons, ADC and perfusion maps were spatially aligned to a common template acquired from six healthy rats using a non-rigid registration procedure. (Klein et al., 2010) Analysis was carried out on four consecutive slices. MRI signal from non-parenchymal tissue was removed by using a mask obtained from the brain extraction tool (BET). (Smith, 2002) CSF was identified and excluded by averaging T_2 maps from all animals and selecting T_2 values higher than the mean plus 4.5 standard deviations of T_2 in normal-appearing contralateral gray matter.

Voxels with abnormal ADC (i.e. tissue lesion) or MTT (i.e. perfusion lesion) were identified from differences of more than 2 times the standard deviation from mean contralateral tissue values. Perfusion-diffusion mismatch volume was calculated from the difference between the total volumes of ADC and MTT abnormality. Presence of a significant perfusion-diffusion mismatch was confirmed when the MTT-based perfusion lesion

Table 3.1. Vessel occlusion patterns and their incidences in normotensive and hypertensive rats after intracarotid embolic clot injection.

	Occlusion pattern			Relative incidence (%)	
Grade	ICA	MCA.M1	MCA.M2	Normotensive group	Hypertensive group
I	0	0	0	36	45
II	0	0	1	15	10
III	1	0	0	17	20
IV	0	1	0	0	0
V	0	1	1	4	5
VI	1	1	0	2	0
VII	1	0	1	9	0
VIII	1	1	1	17	20

ICA: internal carotid artery; MCA.M1: M1 branch of the middle cerebral artery; MCA.M2: M2 branch of the middle cerebral artery. Occlusion scores: 0: non-occluded; 1: occluded.

volume was 20% larger than the ADC-based tissue lesion volume.(Lansberg et al., 2008) Sites of flow obstruction were assessed on MR angiograms by an experienced observer (I.T.). Vessels were scored as '0' for presence of flow and '1' when no flow was detected. Subsequently, arterial occlusion patterns were categorized in eight different 'Occlusion Severity' grades according to occlusions of the internal carotid artery (ICA) and/or the proximal (M1) or distal (M2) branches of the MCA (Table 3.1).

A MR angiography-diffusion mismatch was defined as presence of ICA and/or MCA occlusion in combination with an ADC-based tissue lesion volume of less than 24 mm^3 (proportional to 25 ml as defined in human brain (Allen et al., 2002; Lansberg et al., 2008; Sahin et al., 2011)).
To assess the ability of identifying subjects who could benefit from reperfusion, we subdivided the subjects over four groups: animals with a mismatch that subsequently did benefit from reperfusion (TP), animals with a mismatch that subsequently did not benefit (FP); animals without mismatch that did benefit from reperfusion (FN); and animals without mismatch that did not benefit from reperfusion (TN). Subsequently values were expressed as sensitivity (TP/TP+FN), specificity (TN/FP+TN), and odds ratio (OR) of benefit of reperfusion for effectively reperfused rt-PA- and saline-treated animals with an acute perfusion-diffusion mismatch or MR angiography-diffusion mismatch.

Benefit of reperfusion was defined as absence of lesion growth beyond 10% of the acute ADC-based tissue lesion volume, as calculated from follow-up T_2 lesion volume

at post-stroke day 7. Lesions that grew more than 105% of the perfusion-diffusion mismatch volume, because of negligible acute size or secondary effects, were excluded.

Statistics

Fisher's exact test was applied to determine differences in distribution of the vessel occlusion categories. Lesion volumes were compared using a Kruskal-Wallis test, with subsequent post-hoc Mann-Whitney test with false discovery rate correction for multiple comparisons. Linear mixed effects regression was used for comparing vessel occlusion categories and corresponding lesion volumes. ORs were calculated from 2x2 tables with Haldane's correction for sparse data. All statistics were performed in R. (R Development Core, 2011)

Results

A total of 75 rats (55 normotensive and 20 hypertensive animals) fulfilled the inclusion criteria, i.e. MRA and MRI within 2 h, and acute ADC- and MTT-based lesion volumes larger than 1 mm^3. MRA, DWI and PWI data were acquired at 76±10, 54±12, and 90±11 minutes after embolic stroke induction, respectively.

Vessel occlusion grades

Figure 3.1a shows an example of an MR angiogram of a normotensive rat's Circle of Willis with absence of flow in the ipsilateral ICA as well as proximal (M1) and distal (M2) segment of the MCA acutely after intracarotid blood clot injection. Overall, eight different vessel occlusion patterns, based on flow obstruction in the ipsilateral ICA, MCA. M1 and MCA.M2, were characterized on MR angiograms (Table 3.1). In the normotensive and hypertensive groups, 36% and 45%, respectively, did not display clear vessel occlusion of the ipsilateral ICA or MCA. MRA data from all other animals demonstrated unequivocal occlusions, with largest incidence of ICA occlusion with (occlusion grade VIII) or without (occlusion grade III) complete occlusion of the MCA.

Relationship between ischemic brain lesions and vessel occlusion patterns

Figure 3.1b and 3.1c show examples of the acute tissue and perfusion lesion on ADC and MTT maps, respectively, obtained from a rat with vessel occlusion grade VIII. The topographic distribution of acute tissue and perfusion lesions depended on the vessel occlusion pattern. Figure 3.2 shows lesion incidence maps for the different occlusion grades. Occlusion grades I and III, with incomplete occlusion of the MCA, resulted in mainly subcortical lesions in normotensive animals, with additional cortical involvement in

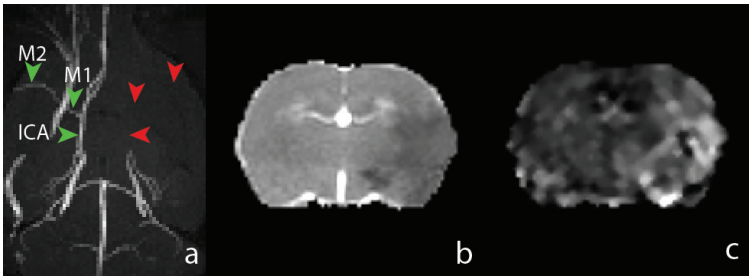

Figure 3.1. *MR angiogram (transversal maximum intensity projection) from a normotensive rat with patent ICA, and M1 and M2 segments of the MCA on the left side (green arrowheads) and flow obstruction in the right ICA, MCA.M1 and MCA.M2 (red arrowheads) (a). Corresponding ADC (b) and MTT (c) brain maps (coronal slice) show a right-sided ischemic lesion with reduced ADC and prolonged MTT in the MCA territory.*

hypertensive animals. This was also observed for single occlusion of the ICA (grade III). Occlusion grade II, which involved occlusion of the distal (M2) part of the MCA only, primarily affected cortical tissue. Occlusion of the proximal (M1) part of the MCA (grades V, VI, VII and VIII) resulted in lesions in both subcortical and cortical areas, with largest lesion volumes when flow was obstructed in ICA, MCA.M1 and MCA.M2 (occlusion grade VIII).
Quantified acute tissue and perfusion lesion volumes are shown in Figure 3.3, which demonstrated that flow obstruction involving ICA and both branches of the MCA, resulted in significantly larger acute tissue lesions as compared to occlusion patterns in which flow in the proximal part of the MCA (MCA.M1) was preserved ($P<0.05$). However, the area of hypoperfusion was not significantly different between occlusion grades.

Hypertensive animals developed larger perfusion lesion volumes than normotensive animals, with largest difference for grade II and VIII occlusions ($P<0.05$). Acute tissue diffusion lesion volumes, on the other hand, were not significantly different between hyper- and normotensive animals.
Significant differences between the individual acute perfusion and tissue lesion volumes, i.e. perfusion-diffusion mismatch, was observed for normotensive rats in occlusion grades II, III and VII, and only for hypertensive rats in occlusion grade I ($P<0.05$).

MR angiography-diffusion and perfusion-diffusion mismatches in reperfused animals

In the subset of rats that underwent follow-up MRI, reperfusion was observed in 13 animals. Follow-up T_2 lesion volumes at post-stroke day 7 were significantly smaller than acute perfusion lesion volumes, and similar in size as compared to acute diffusion lesions (Table 3.2). Benefit from reperfusion was observed in 10 of the 13

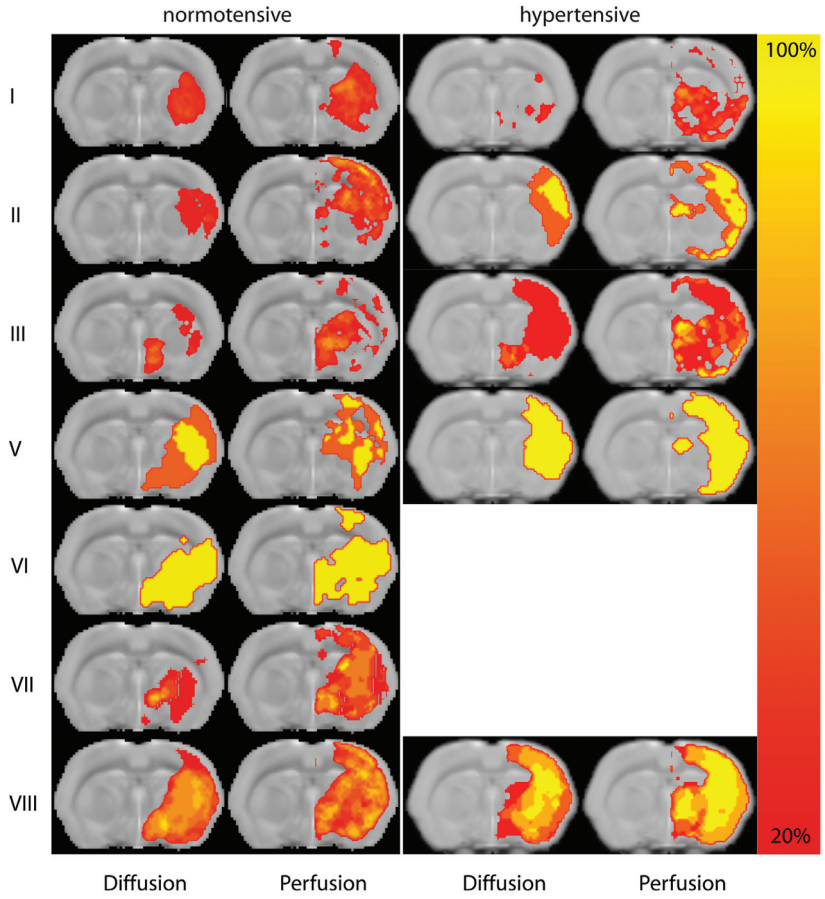

Figure 3.2. *Incidence maps of tissue diffusion and perfusion abnormality in normotensive and hypertensive rats with different arterial occlusion patterns (grade IV was not present in any of the animals). Maps of lesion incidence (% of sample size) are overlaid on a coronal slice from a T_2-weighted anatomical rat brain template.*

animals. Perfusion-diffusion mismatch was detected in all 13 animals, whereas a MR angiography-diffusion mismatch was observed in 38% of the animals. All animals with an angiography-diffusion mismatch also displayed a perfusion-diffusion mismatch. Benefit from reperfusion occurred in 10 out of 13 animals with a perfusion-diffusion mismatch (OR=2.8), and 4 out of 5 animals with an angiography-diffusion mismatch (OR=1.3). Although the sensitivity to detect reperfusion benefit was lower than that of the perfusion-diffusion mismatch (0.44 vs. 0.92), the angiography-diffusion mismatch showed significantly higher specificity (0.67 vs 0.20).

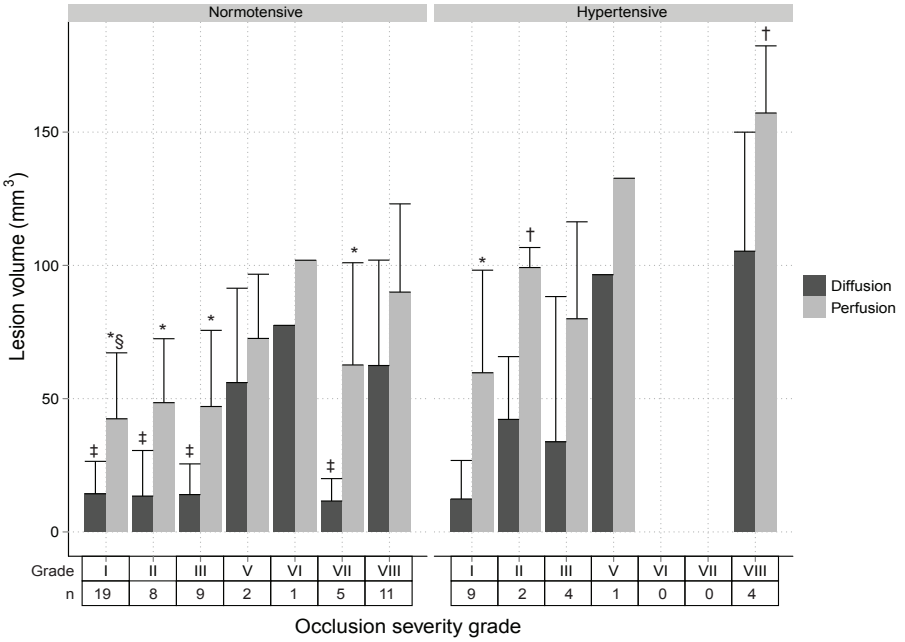

Figure 3.3. *Volume (mean + SD) of perfusion and diffusion abnormality in normotensive and hypertensive animals with different occlusion severity grades (n: number of animals). *P<0.05 versus diffusion lesion volume; †P<0.05 versus normotensive; ‡P<0.05 versus grade VIII diffusion lesion volume; §P<0.05 versus grade VIII perfusion lesion volume.*

Discussion

In this study we assessed presence or absence of vascular flow in three segments of the ICA and MCA, distinguishing eight occlusion severity grades. We found that partial or complete occlusion of the ICA with incomplete flow obstruction in the proximal segment of the MCA (M1) resulted in predominantly subcortical lesions. Occlusions of the distal (M2) segment of the MCA resulted in primarily cortical injury. Large cortical and subcortical lesions were found when flow was lost both in ICA and MCA segments. Lesion volumes were increased in hypertensive animals, which was particularly associated with a larger area of cortical hypoperfusion. Furthermore we found that a MR angiography-diffusion mismatch was more specific in predicting potential benefit from reperfusion than a perfusion-diffusion mismatch. However, in contrast to consistent presence of an acute perfusion-diffusion mismatch, not all animals with reperfusion-induced prevention of lesion enlargement displayed an angiography-diffusion mismatch acutely after stroke.

Table 3.2. Characteristics of reperfused animals with acute perfusion-diffusion and/or angiography-diffusion mismatch

	PDM	ADM
Mismatch incidence	13/13	5/13
Acute perfusion lesion (mm^3)	65.4±21.1	50.0±10.3
Acute diffusion lesion (mm^3)	23.9±19.1	12.5±7.9
Follow-up T_2 lesion (mm^3)	30.0± 31.4	12.3±10.6
Incidence of reperfusion benefit	10/13	4/5
OR (95% confidence interval)	2.7 (0.06-116.0)	1.3 (0.08-48.6)
Sensitivity	0.92	0.44
Specificity	0.20	0.67

PDM: perfusion-diffusion mismatch; ADM: MR angiography-diffusion mismatch; OR: odds ratio.

Patterns of cerebral ischemic lesions: Correlation with vascular occlusion profile

In this study we divided patterns of absence of vascular flow in the ICA and MCA in three different categories distinguishing eight occlusion severity grades. Smallest volumes of acute abnormality on DWI were noted when partial flow was present in the ipsilateral ICA and MCA, whereas larger lesion volumes were observed for higher severity categories with complete vascular occlusions. This in line with previous studies that reported large infarct lesions in tandem occlusions of the ICA and the MCA or proximal occlusions of the MCA both in rats (Overgaard et al., 2010) and patients. (Cheng et al., 2011; Saarinen et al., 2012; Seitz et al., 2009)

The area of perfusion abnormality differed less between occlusion grades, and significant perfusion-diffusion mismatch volumes were observed in occluded normotensive animals in which flow in MCA.M1 was partially preserved. This can be explained by the availability of alternative vascular routes that can compensate for the loss of flow from the main territorial artery. This compensatory flow may originate from other large vessels of the Circle of Willis, as well as leptomeningeal or extracranial arteries (Bederson et al., 1986; Liebeskind, 2003, 2005; Phan et al., 2009; Overgaard et al., 2010; Cheng et al., 2011). Occlusions of MCA.M1 were associated with relatively large lesions. Lenticulostriate arteries that originate from the proximal segment of the MCA form an important perforating end-connection to the basal ganglia and internal capsule, which receive little or no collateral blood flow. (Marinkovic et al., 1985) Consequently, occlusion of the proximal segment of the MCA is typically applied to induce large, reproducible lesions in experimental stroke models (Bederson et al., 1986; Niiro et al., 1996; Cai et al., 1998; Overgaard et al., 2010), and has been considered a trade-off point for good

outcome in clinical stroke patients. (Fiehler et al., 2005; Saarinen et al., 2012; Fiebach et al., 2012)
Rats with chronic hypertension developed larger acute ischemic lesion volumes than those with normal blood pressure. Chronic hypertension as a co-morbidity may affect small arterial and arteriolar integrity via vascular hypertrophy, endothelial dysregulation, and atherosclerosis (Intengan and Schiffrin, 2000). These vascular alterations can significantly increase sensitivity to flow reductions and may also affect compensatory flow capabilities.(Coyle et al., 1984; Coyle, 1986; Coyle and Heistad, 1986; Howells et al., 2010; Reid et al., 2012) This was reflected by a lower incidence of perfusion-diffusion mismatches for the different occlusion grades in hypertensive animals (it was only observed in animals with incomplete flow obstruction in all ICA and MCA segments). Furthermore, occlusion of the distal part of the MCA resulted in larger perfusion and tissue lesions in cortical tissue, suggestive of deficient recruitment of cortical arterial collaterals from leptomeningeal anastomoses and distal collaterals from the Circle of Willis in these animals. (Coyle, 1987)

Reperfusion benefit: angiography-diffusion mismatch versus perfusion-diffusion mismatch

The MR angiography-diffusion mismatch, defined in acute stroke patients by a relatively small lesion on DWI in combination with MRA evidence of an intracranial stenosis or occlusion, has been proposed as an alternative means to identify patients that may benefit from reperfusion (Lansberg et al., 2008). Our study in a rat embolic stroke model shows that 80% of animals with an angiography-diffusion mismatch indeed benefit from reperfusion, with an increased prediction specificity as compared to the perfusion-diffusion mismatch. Yet, some animals without an angiography-diffusion mismatch, which could be identified by presence of a perfusion-diffusion mismatch, also displayed a therapeutic effect of reperfusion. Benefit from reperfusion is not only dependent on the site and extent of vascular occlusion (Marks et al., 2008), but also depends on local microvascular patency (Wang et al., 2001) and capability to accommodate collateral flow to the affected area (Liebeskind, 2003, 2005). Collateral flow may not only prolong tissue salvageability (Fiehler et al., 2005; Sobesky, 2012), it may also improve thrombolytic efficacy by providing additional delivery routes to the site of occlusion (Cheng et al., 2011; Liebeskind, 2005). Despite the potential of the MR angiography-diffusion mismatch to aid in identifying tissue amenability to reperfusion, it does not provide direct information on local perfusion or collateral flow (Schellinger and Köhrmann, 2008; Sobesky, 2012) Additionally, MRA (especially time-of-flight MRA) has decreased sensitivity to flow in more distal parts of the arterial tree (Reese et al., 1999), which may lead to inexact assessment of the degree of arterial obstruction (De Silva et al., 2010).

Some caution in interpretation of our findings on mismatch volumes may be warranted because of the relatively small subset of animals used in this part of study. Furthermore, we applied, after proper adjustments for rat brain, thresholds that have been previously used in clinical studies to determine the tissue amenable for treatment. (Davis et al., 2008; Lansberg et al., 2008; Olivot and Marks, 2008) However, cerebral ischemia is a dynamic process in which development of penumbral tissue depends on severity and duration of ischemia. (Heiss and Rosner, 1983) Single thresholds to dichotomize tissue in normal and lesioned tissue may oversimplify the underlying complex processes on an individual basis. (Kranz and Eastwood, 2009; McCabe et al., 2009; Reid et al., 2012; Sobesky, 2012) The acute lesion on DWI is key in estimating both the perfusion-diffusion and the MR angiography-diffusion mismatch. The DWI lesion is assumed to identify the nonviable ('core') tissue. However, in line with earlier studies (Fiehler et al., 2002; Li et al., 2002), we observed partial recovery of the acute tissue lesion on DWI as compared to the actual irreversibly damaged tissue at follow-up (data not shown). Reversibility of diffusion abnormality is still a matter of debate (Campbell et al., 2012; Dijkhuizen et al., 1998b; Kranz and Eastwood, 2009; Olah et al., 2000; Pierpaoli et al., 1996), but recent MR/PET studies revealed spatial variability of the metabolic rate of oxygen within acute DWI lesions with preserved viability in some parts. (Guadagno et al., 2004; Sobesky et al., 2005) Obviously, the use of complementary information on the severity of hypoperfusion, such as measured with PWI, contributes to improved assessment of the ischemic tissue. Furthermore, voxel-based mappings, rather than regional analysis, may improve diagnostic accuracy by calculation of maps of statistical infarction probability (Wu et al., 2006) (see also Chapter 4 & 5), collateral flow index (Nicoli et al., 2012), or vascular territory. (Hendrikse et al., 2004; van Laar et al., 2008) The latter can be accomplished with MRA which would aid in outcome prediction based on the specific pattern of vascular occlusion. (Cheng et al., 2011; Menezes et al., 2007)

In conclusion, the combined use of DWI, PWI and MRA contributes to improved insights in the effect of specific arterial occlusion profiles, which together with knowledge of to the individual (collateral) blood supply, may advance outcome prediction and could improve treatment decision-making.

4

Early identification of potentially salvageable tissue with MRI-based predictive algorithms after experimental ischemic stroke

Mark J.R.J. Bouts[1], Ivo A.C.W. Tiebosch[1], Annette van der Toorn[1], Max A. Viergever[1], Ona Wu[2], and Rick M. Dijkhuizen[1]

[1] Biomedical MR Imaging & Spectroscopy Group, Image Sciences Institute, University Medical Center Utrecht, Utrecht, The Netherlands.
[2] Athinoula A. Martinos Center for Biomedical Imaging, Department of Radiology, Massachusetts General Hospital, Charlestown, MA, United States.

published in Journal of Cerebral Blood Flow and Metabolism 2013 (in press)

Abstract

Individualized stroke treatment decisions can be improved by accurate identification of the extent of salvageable tissue. MRI-based approaches, including measurement of a 'perfusion-diffusion mismatch' and calculation of infarction probability, allow assessment of tissue-at-risk, however the ability to explicitly depict potentially salvageable tissue remains uncertain.

In this study five predictive algorithms (Generalized Linear Model (GLM), Generalized Additive Model, Support Vector Machine, Adaptive Boosting and Random Forest) were tested in their potency to depict acute cerebral ischemic tissue that can recover after reperfusion. Acute T_2-, diffusion-, and perfusion-weighted MRI, and follow-up T_2 maps were collected from rats subjected to right-sided middle cerebral artery-occlusion without subsequent reperfusion, for training of algorithms (Group I), and with spontaneous (Group II) or thrombolysis-induced reperfusion (Group III), to determine infarction probability-based viability thresholds and prediction accuracies.
The infarction probability difference between irreversible – i.e. infarcted after reperfusion – and salvageable tissue injury – i.e. non-infarcted after reperfusion – was largest for GLM (20±7%) with highest accuracy of risk-based identification of acutely ischemic tissue that could recover upon subsequent reperfusion (Dice's similarity index=0.79±0.14).

Our study demonstrates that assessment of the heterogeneity of infarction probability with MRI-based algorithms enables estimation of the extent of potentially salvageable tissue after acute ischemic stroke.

Introduction

Contemporary treatment protocols for patients suffering from acute ischemic stroke ask for adequate and early identification of tissue at risk of infarction to allow for proper clinical decision-making. Current thrombolytic treatment guidelines indicate safe treatment time-windows of 3 to 4.5 hours after stroke onset. (Hacke et al., 2008) However, this time-window may be too strict in particular cases, unnecessarily excluding patients who may benefit from reperfusion therapy. (Davis et al., 2008)

Neuroimaging, particularly with magnetic resonance imaging (MRI), provides a powerful tool for characterization of acute cerebral ischemic tissue status, which can aid in treatment decision-making in individual patients. (Donnan et al., 2009) In particular, diffusion-weighted imaging (DWI), for detection of acute ischemic tissue damage (Hjort et al., 2005a), and perfusion-weighted imaging (PWI), for detection of hemodynamic disturbances (Sorensen et al., 1999b), provide sensitive and specific means for acute stroke diagnosis. Dichotomization of MRI-derived perfusion- and diffusion-based lesion volumes into overlapping and non-overlapping areas enables selection of patients with a 'perfusion-diffusion mismatch' who may be eligible for thrombolytic treatment.(Kidwell et al., 2003; Davis et al., 2008; Schellinger et al., 2010) However, lack of standard post-processing procedures and threshold values may compromise robust characterization of a 'perfusion-diffusion mismatch' (Donnan et al., 2009; Sobesky, 2012), and volumetric analysis may obscure and oversimplify the complex and heterogeneous status of the affected tissue.(Kidwell et al., 2003; Lo et al., 2005; Hjort et al., 2005b) This mismatch area may therefore overestimate the actual tissue area at risk (Sorensen et al., 1999b; Sobesky et al., 2005; Wu et al., 2006), as well as exclude injured tissue that is potentially salvageable. (Fiehler et al., 2002)

The complex relation between multiple pathophysiological factors involved in stroke lesion progression may be better caught and described using multiparametric imaging-based statistical algorithms. These algorithms allow voxel-wise integration of multiple MRI-based tissue and perfusion parameters to compute a single quantitative probabilistic index.(Wu et al., 2001; Ostergaard et al., 2009) Multiparametric algorithms can more accurately estimate risk of infarction compared with single MRI-based parameters, and show good correspondence with actual lesion outcome.(Wu et al., 2001; Huang et al., 2011) However, it is unclear whether such algorithms also enable accurate differentiation between irreversibly damaged and potentially salvageable tissue, which would significantly advance the value of this approach for selection and planning of therapeutic intervention.(Wu et al., 2006; Jonsdottir et al., 2009)

We hypothesized that acute imaging-based predicted infarction areas can be subdivided into volumes of irreversible and reversible tissue injury. Hence, we selected five well-established predictive algorithms and determined each algorithm's efficacy in 1) early detection of tissue at risk of infarction, and 2) differentiating irreversibly damaged tissue from potentially salvageable tissue, based on multiparametric MRI data after experimental stroke. To that aim, we compared early measures of infarction risk with final outcome after ischemic stroke in rats with or without subsequent reperfusion.

Materials and methods

Animal procedures

We partly included data from animals that have been previously used for another study. (Tiebosch et al., 2012) The current study provides new and original results that have not been described in our previous study. Animal procedures were conducted according to the guidelines of the European Communities Council Directive and approved by the Ethical Committee on Animal Experiments of the University Medical Center Utrecht and Utrecht University. Surgical procedures have been described in detail elsewhere. (Longa et al., 1989; Tiebosch et al., 2012) In brief, prior to surgery male Wistar rats (275-400 g, Harlan, Horst, Netherlands) received an intramuscular injection of gentamicin sulfate (5 mg/kg) as antibiotic treatment, and 2.5 mL glucose-saline solution to prevent dehydration. Subsequently animals were anesthetized by a subcutaneous injection of 0.5mL/kg fentanyl citrate (0.315 mg/mL) and fluanisone 10 mg/mL (Group I), or by mechanical ventilation with 2% isoflurane in air:O_2 (7:1) (Groups II and III). Body temperature was maintained at 37.5 (±0.5) °C with a temperature-controlled heating pad. The right carotid artery was exposed by a ventral incision in the neck. A modified catheter was advanced into the internal carotid artery, until the tip was proximal to the middle cerebral artery (MCA). Unilateral MCA occlusion was induced by insertion of an intraluminal filament (Group I; n=7) (1), or by slow injection of a homologous blood clot (50 mm long, 24 h old) (Groups II and III; n=7 and 5, respectively). Subsequently, the wound was closed and animals received a subcutaneous injection of buprenorphine (0.03 mg/kg) for pain relief, and 5 mL glucose-saline solution to compensate for loss of water and minerals. In the first three days after surgery, excessive weight loss was partially compensated by subcutaneous injection of Ringer's lactate solution (0-10 mL, depending on degree of weight loss). Within 30 min after MCAo, animals were positioned in the MR scanner, and acute imaging was conducted between 0.5 and 2 h after stroke. Immediately after the first imaging session, Group II and III animals received saline (Group II) or 10.0 mg/kg recombinant tissue plasminogen activator (rt-PA (Actilyse®, Boehringer Ingelheim, Alkmaar, The Netherlands, 3.0 mg/mL)) (Group III), intravenously administered over a

30-min period (10% bolus injection; 90% continuous infusion). Animals were allowed to recover afterwards. Group I animals underwent a second MRI session at 72 hours after onset, whereas for Group II and III animals MRI was repeated at 24 hours after MCAo to confirm reperfusion, and 168 hours to establish actual tissue injury.
In Group I, 7 out of 14 rats with an acute lesion in the MCA territory survived up to 3 days to undergo the second MRI session. In Groups II and III, survival rate after successful MCAo was higher: 7 out of 9 animals in Group II, and 5 out of 7 animals in Group III survived up to day 7. This led to the following sample sizes for the present study: Group I: n=7; Groups II: n=7; and Group III: n=5.

Image acquisition

MRI was conducted on a 4.7T scanner (Varian, Palo Alto, CA, USA). Group I animals underwent MRI – with a 9.0-cm inductively coupled Helmholtz coil for signal transmission and detection – at 0.5-2 h and at 72 h after MCAo. For each session, MRI consisted of T_2-weighted spin echo (TR 3000 ms; TE 17.5 ms; number of echoes (NE) 8; data-matrix 128x128x11; field-of-view (FOV) 25x25x13.2 mm^3; 0.13 mm inter-slice gap), diffusion-weighted multi-slice echo planar imaging (EPI) (TR 2000 ms; TE 80 ms; data-matrix 128x128x11, FOV 25x25x1.2 mm^3; 0.13 mm inter-slice gap; b 124, 404, 844 and 1444 s/mm^2; 3 diffusion directions), and dynamic susceptibility-weighted contrast-enhanced MRI (TR 300 ms; TE 20 ms; flip angle 5°; data-matrix 64x64x3; 500 time-points; FOV 25x25x3.6 mm^3; 0.13 mm inter-slice gap) in combination with an intravenous bolus of gadopentate-dimeglumine (Magnevist, Schering, The Netherlands; 0.5 mg/kg).
Group II and III animals underwent MRI with an updated protocol – using a 9.0-cm inductively coupled Helmholtz coil and an inductively coupled 2.5-cm surface coil for signal detection, respectively – at 0.5-2 h, 24 h and 168 h after MCAo. MRI consisted of T_2-weighted spin echo (TR 3600 ms; TE 15 ms; NE 12; data-matrix 256x128x19; FOV 32x32x19 mm^3), diffusion-weighted 8-shot EPI (TR 3500 ms; TE 38.5 ms; b 0 and 1428 mm^2/s; 6 diffusion directions; data-matrix 128x128x19; FOV 32x32x19 mm^3), and dynamic susceptibility-weighted contrast-enhanced MRI (TR 330ms; TE 25ms; flip angle 5°; data-matrix 64x64x5; 400 time-points; FOV 32x32x5.0 mm^3) was acquired in combination with an intravenous bolus of gadobutrol (Gadovist, Schering, The Netherlands; 0.32 mmol/kg).

Image processing

Parametric maps of the T_2 and trace of the apparent diffusion coefficient (ADC) were calculated by mono-exponential fitting. Maps of the cerebral blood flow index (CBFi), cerebral blood volume (CBV) and mean transit time (MTT) were calculated by tracer arrival time-insensitive deconvolution (Wu et al., 2003), with an arterial input function from two voxels in the ipsilateral internal carotid artery. Relative tracer delay and

dispersion were determined from the time-to-peak of the derived residue function (T_{max}). (Wu et al., 2003) All parametric maps were spatially aligned using a non-rigid co-registration procedure. (Klein et al., 2010) This was followed by segmentation of brain parenchyma from surrounding tissue using the brain extraction tool. (Smith, 2002) All maps were normalized and expressed as relative after dividing each voxel by mean values of normal appearing contralateral gray matter regions, except for T_{max}. T_{max} maps were normalized by subtraction of the derived mean values. (Wu et al., 2006) Mean contralateral gray matter values were calculated using a contralateral, CSF-excluded mask of four consecutive slices. Contamination by white matter tissue was prevented by three consecutive morphological erosion steps. Ipsilateral and contralateral hemispheres were defined by a manually derived linear boundary through the midline. CSF, specified as voxels with T_2 values at least 4.5 standard deviations higher than mean normal contralateral values (from 65 control rats), was excluded in further analysis. Infarcted tissue was automatically identified as voxels with T_2 values at least 2 standard deviations higher than mean contralateral gray matter values on post-stroke day 3 (Group I) or 7 (Groups II and III) (T_2-based lesion sizes at day 3 after permanent MCAo or at day 7 after embolic stroke have been shown to correspond with infarction size on post mortem histological sections (Mottet et al., 1997; Henninger et al., 2007)). Acute perfusion abnormality was similarly identified on acute MTT values. Acute diffusion abnormality was defined as at least 2 standard deviations lower than mean contralateral ADC values. Volumes with abnormal tissue were subsequently normalized by the total ipsilateral hemispheric volume, and expressed as hemispheric lesion fraction (HLF=lesion volume/ipsilateral hemispheric volume). The volumetric difference between the acute perfusion and diffusion abnormality was used to determine the perfusion-diffusion mismatch. A reduction of more than 40% in the volume of perfusion abnormality from 2 to 24 hours in Group II and III animals was considered indicative of reperfusion.

Tissue outcome prediction

To predict post-stroke tissue infarction, we used predictive algorithms that combine a carefully balanced set of acutely acquired MRI parameters ($x_i=x_1,..,x_m$) - here T_2, ADC, CBF, MTT, and T_{max} - on a voxel-wise basis in relation to corresponding tissue infarction derived from T_2 follow-up maps. (Wu et al., 2010) A predictive algorithm calculates, based on a training dataset, an optimized set of coefficients that map a relation of samples from the acutely acquired images to a class that represent ultimately infarcted tissue and a class that represents non-infarcted tissue. Subsequently, this set of coefficients can be used to estimate the probability of tissue infarction ($P_{infarct}=P(infarct|x_1,..,x_m)$) from newly introduced samples. To estimate $P_{infarct}$, we selected five predictive algorithms based on 1) a generalized linear model (GLM)

(Wu et al., 2001), 2) a generalized additive model (GAM) (Wood, 2006), 3) a support vector machine (SVM) (Bishop, 2007; Huang et al., 2011), 4) decision tree-based adaptive boosting (ADA) (Freund and Schapire, 1997), and 5) random forest (RF). (Breiman, 2001) Of these five algorithms, GLM and SVM had previously shown to successfully predict the extent of tissue infarction. (Wu et al., 2001; Huang et al., 2011)

GLM, GAM and SVM estimate $P_{infarct}$ by a logistic function:

$$P = \frac{1}{1+e^{-\eta(x)}}$$

where η(x) is a link function that defines the relationship of *M* MRI parameters (x) to the tissue outcome at follow-up. In GLM, η(x) is a linear link function:

$$\eta(x) = \sum_{j=1}^{M} \beta_{jT} x_j + \alpha$$

with β describing the weights of each MRI parameter, and α the bias or intercept of the linear function. Coefficients α and β can be estimated using iterative reweighted least squares fitting.(Wu et al., 2001, 2007)
In GAM β is replaced by an additional smoothing term f(x):

$$\eta(x) = \sum_{j=1}^{N} f_j(x_j) + \alpha$$

defining a nonlinear link function, where f(x) can be estimated using cubic spline regression. (Wood, 2006) In contrast to GLM and GAM, SVM uses a more indirect relationship defined in η(x). In SVM η(x) is a decision function which aims to subdivide the two tissue classes (infarct versus non-infarct). This binary decision function describes a linear hyperplane that aims to maximize the separating gap (i.e. margin) between the two tissue classes' training samples and is defined as:

$$f(x) = \left(\sum_{i}^{N} y_i \alpha_i \cdot K(x, x_i) + b \right)$$

α is a weighting vector that selects only those samples closest to the class boundaries which contribute to the estimation of the linear hyperplane (i.e. support vectors). α is bound between 0 and C, a regularization parameter that controls the tradeoff between optimizing the margin and allowing for some samples to reside on the wrong side of the decision boundary (i.e. misclassification error). Furthermore, a transformation kernel $K(x,x_i)$ can be used to circumvent the need of estimating a highly complex hyperplane by rearranging the data such that it allows for a simple linear decision boundary. (Bishop, 2007; Huang et al., 2011) In the end, class probability is obtained after fitting the binary decision function results to a sigmoid function. (Bishop, 2007)

In contrast to GLM, GAM and SVM, which define a single effective classification function, $P_{infarct}$ can be estimated by combining multiple apparently less effective decisions of which the combined probabilistic estimate may be highly effective. (Friedman, 2000; Breiman, 2001) In decision tree analysis the presented training data is recursively dichotomized in subgroups until node purity (i.e. all subgroup samples belong to the same class) is maximized. (Friedman, 2000) Yet, small variations in training data sampling may result in highly different decisions, i.e. decision trees are highly instable. This instability may therefore make these trees highly ineffective. Instability can be circumvented and made beneficial by using the collective classification or ensemble result of multiple decision trees for estimating infarction probability. (Bishop, 2007) In this study two ensemble methods were tested: Adaptive boosting (ADA) and random forest (RF). In this context ADA was applied as an ensemble meta-algorithm that sequentially grows and weights multiple decision trees to give an estimate of infarct probability. At each iterative step, weights are adjusted to emphasize the incorrect classifications, focusing on the parts of the training data that needs most improvement. (Freund and Schapire, 1995) Random forest (RF) is another type of ensemble method that provokes decision tree instability using bootstrap aggregating or bagging. A subset of randomly drawn samples with replacement from the set of training samples is used to simultaneously create multiple, variable decision trees. Variability is further established by randomly selecting a subset of MRI parameters for branching the decision trees' nodes (i.e. 'tries'). Infarction probability is determined by majority vote of each tree's classification result. (Breiman, 2001)

The five selected algorithms were operationally optimized by testing for prediction error for an applicable range of parameters. Prediction error was determined using data from Group I animals. Each parameter setting was assessed using a cross-validation scheme for which 500 bootstrapped realizations were taken from the complete set of data samples. Of each realization, 60% was reserved for training and 40% was reserved for testing. All predictive algorithms and subsequent analysis were created and applied using R (R Development Core, 2011) (http://www.r-project.org/).
Akaike Information Criterion (AIC), a measure for prediction error and algorithm complexity, was used to determine the MRI parameters to include for prediction.(Bishop, 2007) A GLM with all operational parameters included, was calculated as reference followed by sequentially adding or removing MRI parameters to minimize AIC (Wu et al., 2007). The optimal number of MRI parameters was then applied to all subsequent algorithms. For GAM, prediction error was minimized estimating the number of smoothing terms f(x) needed using generalized cross validation with unbiased risk estimator (UBRE) scoring.(Wood, 2006) SVM, ADA, and RF prediction error were minimized from the amount of wrongfully classified voxels (false positives and false negatives) for

each prediction, i.e. the classification error:

$$\varepsilon = \frac{FP + FN}{P + N}$$

Classification error minimization was associated with better predictive accuracy, provided algorithm flexibility was guaranteed. Algorithm flexibility was assured by reducing training-set bias. Training-set bias was defined as the difference in classification error of the test dataset compared to the training dataset. Under the assumption that with increasing number of available samples the classification error in the training set (apparent error: ε_a) increases, and the classification error in the test set decreases, training set bias should reduce. Increasing training bias can be associated with overfitting of the algorithm and thus to reduced overall performance of the algorithm.

A grid-searching approach, with gradually decreasing parameter step sizes, was applied to optimize the operational parameters of ADA, RF, and SVM. For ADA, the number of decision trees was compared with the maximally allowed depth of the partitioning trees. Analysis of the number of decision trees was considered from a range of 5-200 with a slowly decreasing step size from 50-25. Tree depth was considered from 1-5 with step sizes of 1. For RF, the number of MRI parameters randomly selected at each node (tries) was compared with the number of decision trees. The number of trees was varied from 50 to 500 with slowly decreasing step sizes of 50 to 5; the number of tries ranged from 1-5 with fixed step size of 1. SVM parameters as the transformation kernel k and regularization parameter C were similarly optimized. Five types of transformation kernels were selected and evaluated in combination with regularization parameter C. C was linearly incremented from 0.1 to 100 with stepsizes of 0.01.

The selected transformation kernels were:
Linear:

$$K(x, x_i) = \langle x, x_i \rangle$$

Radial basis function (RBF):

$$K(x, x_i) = e^{\left(-\sigma \|x - x\|^2\right)}$$

Laplace:

$$K(x, x_i) = e^{\left(-\sigma \|x - x\|\right)}$$

Polynomial:

$$K(x, x_i) = \left(scale \cdot \langle x - x_i \rangle + offset\right)^{\deg ree}$$

Bessel:

$$K(x, x_i) = \frac{Bessel_{v+1}^{n}\left(\sigma \|x - x_i\|\right)}{\left(\sigma \|x - x_i\|\right)^{-n(v+1)}}$$

At each parameter step, RBF and Laplace kernel width - defined as parameter σ - were automatically estimated by approximation of a range of values (usually between 0.1 and 0.9) which gave best results for segmentation (Karatzoglou et al., 2004) (data not shown). The polynomial kernel was assessed by varying the scale (1-50, stepsize=5), offset (1-50, stepsize=5) and degree (1-5, stepsize=1). For the Bessel kernel the order and degree were equally varied. (Karatzoglou et al., 2004)

After operational optimization, each algorithms' prediction accuracy was determined in Group I with a jack-knifing (i.e. leave-one-out) approach to prevent bias. (Efron, 1987) Predictions in Group II and III were based on aggregated data from Group I-trained models. Prediction accuracy was assessed by comparing the estimated infarction probability to the follow-up T_2-based tissue outcome. Probability maps were iteratively thresholded in step values of 1% ranging from 0-100%, and at each threshold, the voxels with correct and incorrect predictions of infarction - true positives (TP) and false positives (FP), respectively - and non-infarction - true negatives (TN) and false negatives (FN), respectively - were calculated. This allowed calculation of model sensitivity or recall:

$$snc = recall = \frac{TP}{TP + FN}$$

specificity:

$$spc = \frac{TN}{TN + FP}$$

and the positive predictive value or precision:

$$prc = \frac{TP}{TP + FP}$$

Subsequently, sensitivity and 1-specificity were used for receiver-operator-characteristic (ROC) statistics. Precision and recall values were used to create precision-recall (PR) graphs. In ROC statistics highly skewed datasets can give a biased view of an

algorithm's performance that may be avoided using PR statistics.(Davis and Goadrich, 2006) Quantitative comparisons were provided by calculating the area-under-the curve of the ROC (AUC_{roc}) and PR curve (AUC_{pr}). Infarction probability maps were thresholded at 50% to define predicted infarct fraction (PIF=predicted infarct volume/ipsilateral hemispheric volume). (Jonsdottir et al., 2009; Wu et al., 2007) Overlap of PIF and ultimate infarct fraction (UIF) defined from follow-up T_2 maps was expressed by Dice's similarity index and used to assess spatial accuracy. (Dice, 1945)

$$DSI = \frac{TP + TP}{TP + FP + FN + TP}$$

Differentiation between irreversibly damaged and potentially salvageable tissue

Group II and III animals were then used to differentiate between irreversibly damaged tissue, and tissue at risk of infarction that could be saved upon reperfusion. Therefore acute infarction risk maps were further partitioned into: a) normal appearing tissue (acute infarction probability <50%); b) irreversibly damaged tissue (acute infarction probability >50%, and tissue abnormality at follow-up stage); and c) potentially salvageable tissue at risk (acute infarction probability >50% and normal tissue appearance at follow-up stage). The infarction probability threshold that optimally separated potentially salvageable from irreversibly damaged tissue was determined by calculating inter- and intra-class infarction probability variance at probability values between 1 and 100%. Optimal differentiation was considered at the threshold for which inter- and intra-class variances were highest and lowest, respectively. (Otsu, 1979) The derived threshold was then applied to assess the overlap (with DSI) of: acutely predicted irreversibly damaged tissue and infarction at follow-up (i.e. TP); acutely predicted irreversibly damaged tissue and salvaged tissue at follow-up (i.e. FP); acutely predicted potentially salvageable tissue and normal appearing tissue at follow-up (i.e. TN); and acutely predicted potentially salvageable tissue and infarction at follow-up (i.e. FN).

Statistical analysis

Mean predicted infarction risk for each algorithm was compared using repeated measures ANOVA with post-hoc Tukey HSD correction. Prediction performance measures and tissue volume fractions were compared using a two-tailed Kruskal-Wallis test. Unpaired data was subsequently tested with post-hoc two-tailed Mann-Whitney rank sum test and false discovery rate (fdr) correction; pairwise comparisons were tested with two-tailed Mann-Whitney signed rank test with fdr correction.

Results

Acute and follow-up lesion volumes

Figure 4.1 shows lesion volumes, expressed as hemispheric lesion fractions, calculated from acute diffusion, acute perfusion, and follow-up T_2 MRI. In the acute phase, diffusion- and perfusion-based lesion volumes were not statistically different between groups; at follow-up, however, infarct volumes in Group I (permanent filament MCAo; day 3) were significantly larger than those in Groups II and III (embolic MCAo with reperfusion; day 7). All groups showed a significantly smaller acute diffusion-based lesion volume as compared to the volume of acute perfusion loss, i.e. 'perfusion-diffusion mismatch'. Follow-up T_2-based lesion volume was comparable to the acute perfusion-based lesion volume in Group I, and to the acute diffusion-based lesion volume in Groups II and III. MRI at 24 hours post-stroke revealed that the tissue volume with perfusion abnormality had reduced by more than 40% in all but one (Group III) animal in Groups II and III, indicative of reperfusion.

Algorithm optimization

Step-wise AIC optimization showed lowest AIC (AIC=2461) for the MRI parameter

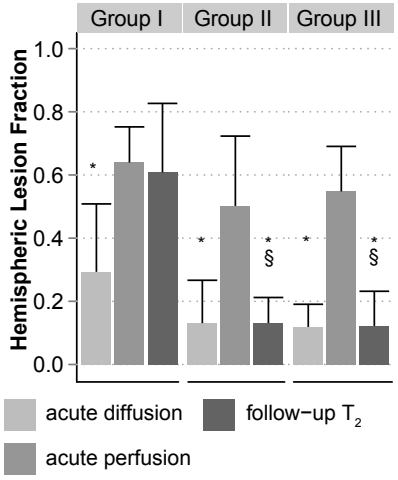

Figure 4.1. *Hemispheric lesion fractions (HLFs) based on abnormal values on acute ADC maps ('acute diffusion'), acute MTT maps ('acute perfusion') and follow-up T_2-weighted images ('follow-up T_2'), respectively, in Groups I-III (mean + sd). *P<0.05 versus acute perfusion-based HLF; §P<0.05 versus Group I follow-up T_2-based HLF.*

combination of T_2, ADC, CBF, MTT and T_{max}. Subsequently, these MRI parameters were presented to all other predictive algorithms to allow for fair comparison. For the GAM, smoothing was best applied to all parameters corresponding to lowest UBRE score (UBRE=-0.33). Figure 4.2 shows plots of the error optimization of the operational parameters of RF (A), ADA (B), and SVM (C). In RF, number of tries was evaluated compared with the number of trees grown. Classification error for RF classification leveled out at ε=0.171±0.005, corresponding to a total of 200 trees and 1 randomly sampled variable for node construction. For ADA the number of sequential steps was compared with the classification error for maximal depth of the partitioning tree. Minimal classification error was detected at a maximum of 125 iterations and maximal partition depth of 2 (ε=0.173±0.005). Each transformation kernel *C* was compared with the classification error to optimize SVM operation (kernel optimization was done in previous separate steps (data not shown)). The curves show persistent lowest error values for RBF and Laplace kernels, with lowest classification error for a Laplace kernel at *C*=1.2 and σ=0.39 (ε=0.18±0.005).

Prediction of infarction

The five predictive algorithms were trained with Group I data and subsequently applied to Group I, II and III data. Figure 4.3 shows examples of resultant infarction probability maps in Group I, II and III animals. Based on AUC_{roc}, AUC_{pr}, sensitivity and specificity values, all algorithms predicted actual infarction approximately equally well in (training) Group I (Figure 4.4). The size of overlap between the 50% risk-thresholded predicted infarction and actual infarcts on follow-up, was similar for all algorithms (mean DSI=0.77±0.11; P=0.99), which was also the case for the areas under the ROC curve (AUC_{roc}=0.88±0.12; P=0.99) and PR curve (AUC_{pr}=0.82±0.12; P=0.74).

Prediction accuracy in Groups II and III was similar for all algorithms. In contrast to Group I, however, the volumes of increased risk of infarction were significantly larger than follow-up infarct volumes in Groups II and III. This was reflected by significantly lower model specificity, AUC_{pr}, and DSI in Groups II and III as compared to Group I (Figure 4.4).
Infarction probability values within the predicted infarction volume were significantly different between algorithms (Table 4.1), despite similarity in size of the predicted infarction (P=0.83). Overall, mean infarction probability in predicted infarction volume was highest for ADA, and lowest for GLM. For all algorithms, infarction probability values in the predicted infarct volume were significantly higher in Group I as compared to Groups II and III, which was associated with a higher degree of perfusion loss (see also Figure 4.6). Nevertheless, the infarction probability values of tissue that actually infarcted were not significantly different between groups (Table 4.1).

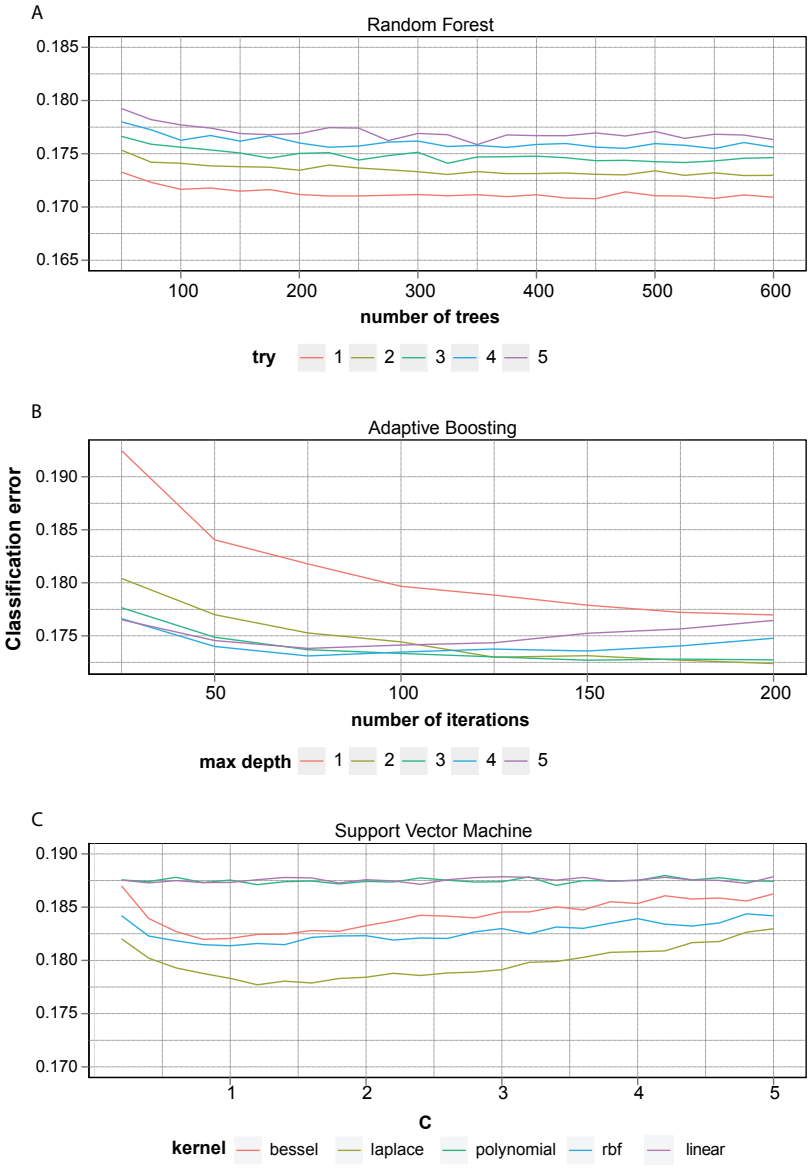

Figure 4.2. *Operational algorithm parameter optimization by minimizing classification error over 500 bootstraps of training and testing data. In RF (A), the number of MRI variables used for node-splitting (try) was compared with the number of trees used in ensemble; optimum was considered for 1 try and error stabilized around 200 trees. In ADA (B), the number of sequential steps was opposed to the maximal depth of the decision tree; optimum was considered for maximal depth of 2 and a maximum of 125 iterations. In SVM (C), optimization of the classification regularization parameter C was competed with five transformation kernels; lowest error was found for C=1.2 and a Laplace kernel with σ=0.39.*

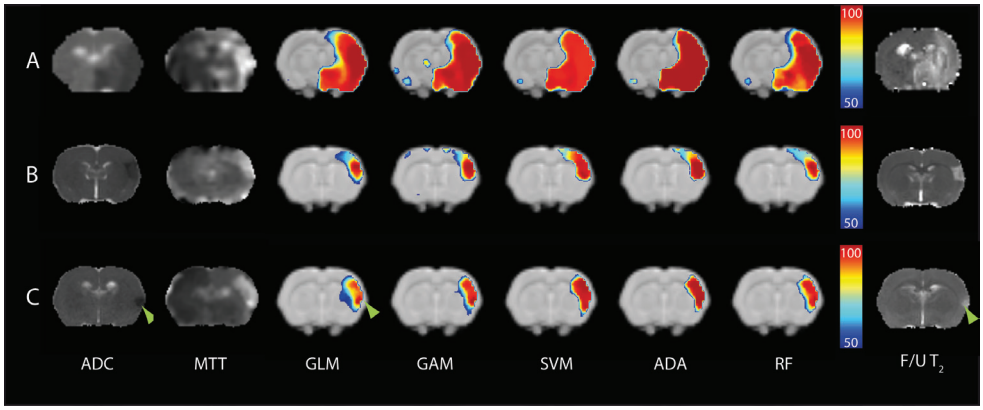

Figure 4.3. *Coronal rat brain slices with acute diffusion (ADC map; hypointensity) and perfusion abnormalities (MTT map; hyperintensity) after permanent filament MCAo (Group I) (A); embolic MCAo followed by vehicle treatment (Group II) (B); and embolic MCAo followed by rt-PA treatment (Group III) (C). Color-coded maps overlaid on anatomical template images display predicted risk of infarction (thresholded at 50%) calculated with GLM, GAM, SVM, ADA, and RF algorithms. Predicted infarction in Group I (A) corresponded well with the infarct on follow-up (F/U) T_2 map (hyperintensity), whereas infarct predictions in Groups II (B) and III (C) overestimated the ultimate infarct. Heterogeneity in risk values within the predicted infarction areas were particularly evident on GLM-based maps in Group III (C), in which the follow-up infarct correlated well with high risk values (green arrowheads), whereas salvaged tissue had distinctively lower risk values. This was less evident for ADA- or SVM-based predictions.*

Differentiation between irreversibly damaged and potentially salvageable tissue

Table 4.1 shows that infarction probabilities in the predicted infarction volume were lower in subsequently salvaged tissue as compared to ultimately infarcted tissue, which was most evident for GLM. Infarction probability profiles within the predicted infarction volumes were further categorized based on the smallest intraclass and largest interclass variance of areas that corresponded with eventually salvaged (FP) and eventually infarcted tissue (TP). Optimization yielded the lowest threshold for GLM (74±1.0%, $P<0.05$ versus all other algorithms). For ADA the threshold value was highest (82±1.4%). Figure 4.5 depicts density profiles of calculated infarction probabilities in Groups II and III. Infarction probability difference between potentially salvageable and irreversibly damaged tissue was largest for GLM (20±6.9%) and GAM (21±5.0%), which was significantly higher than the difference (13±4.3%) calculated with ADA ($P<0.05$).

Figure 4.6 shows that in all groups, acute CBF, MTT and T_{max} values were significantly different in the predicted irreversibly damaged and potentially salvageable tissue as compared to contralateral, indicative of critical perfusion loss. ADC values were significantly lowered in potentially salvageable tissue, but ADC values of predicted

Table 4.1. Predicted hemispheric infarction fractions and infarction probability

Model	Group	Hemispheric fraction	Infarction probability		
			PIV	Infarcted tissue	Salvaged tissue
GLM	I	0.58±0.13	84±8	91±5	69±7
	II	0.41±0.17†	70±8*	87±9	67±7
	III	0.31±0.14*†	72±3	89±9	68±6
	Overall		75±9	89±8	67±6
GAM	I	0.59±0.15	87±6	96±4	73±9
	II	0.38±0.17*†	77±5	96±4	75±6
	III	0.28±0.13*†	78±4	95±6	74±9
	Overall		81±7	96±4	74±7
SVM	I	0.60±0.15	90±2	95±2	83±4
	II	0.40±0.16*†	83±5*	96±2	81±5
	III	0.30±0.11*†	84±5*	95±4	81±8
	Overall		86±5	95±3	82±5
ADA	I	0.56±0.15	94±4	99±0	82±8
	II	0.36±0.18†	86±4*	99±2	85±5
	III	0.25±0.12*†	87±5	97±7	85±9
	Overall		89±5	98±4	84±7
RF	I	0.59±0.14	87±5	94±3	74±8
	II	0.40±0.17†	72±5*	91±5	73±5
	III	0.31±0.10*†	75±7*	91±10	73±9
	Overall		79±8	92±6	73±7
Ultimate infarct	I	0.61±0.22			
	II	0.13±0.08*			
	III	0.12±0.11*			

Hemispheric fractions reflect the portions of ipsilateral tissue that was predicted to become infarcted (at 50% risk threshold) as calculated with GLM, GAM, SVM, ADA and RF, and that ultimately turned out to be infarcted (on follow-up T_2 maps). Infarction probability(%) were calculated in the entire predicted infarction volume (PIV), and in the portions that were ultimately infarcted and salvaged at follow-up. Values are shown as mean±sd for Groups I, II and III, and averaged over all groups ('Overall'). Overall mean infarction probability in the predicted infarction volume was significantly different between all algorithms (Kruskall-Wallis test: $P<0.001$). *$P<0.05$ versus Group I; †$P<0.05$ versus ultimate infarct fraction.

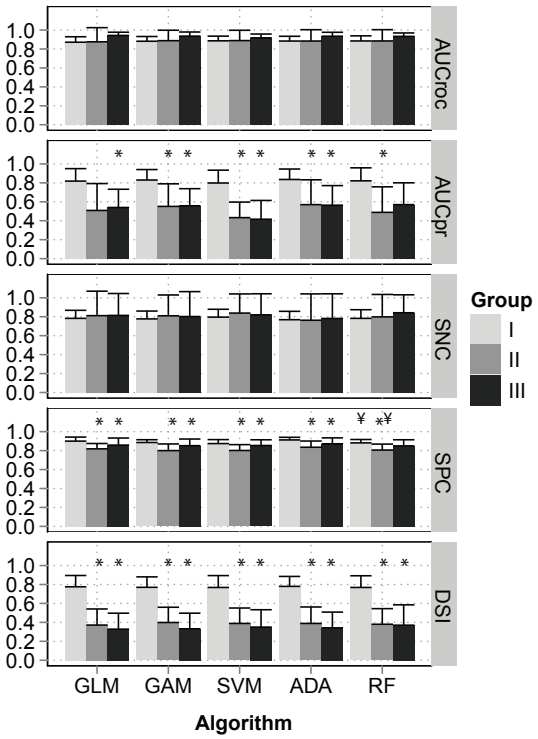

Figure 4.4. *Performance measures of the predictive algorithms for Groups I, II and III (mean+sd). AUC_{roc}: area under the ROC curve; AUC_{pr}: area under the PR curve; SNC: sensitivity; SPC: specificity; DSI: Dice's similarity index at a risk threshold of 50%.*P<0.05 versus Group I; ¥P<0.05 versus GLM.*

irreversibly damaged tissue were lower (P<0.001). T_2 values were also significantly different in the predicted irreversibly damaged and potentially salvageable tissue as compared to contralateral. Furthermore in Group II, T_2 was slightly elevated in irreversibly damaged tissue compared with salvageable tissue. These changes are reflective of progressive tissue injury.

The overlap (expressed as DSI and depicted in Figure 4.7) between acutely predicted infarction volume and actual infarct volume at follow-up, revealed that GLM and RF recognized potentially salvageable tissue best with highest overlap of predicted salvageable and actually salvaged tissue (TN), and lowest overlap of acutely predicted irreversibly damaged tissue but salvaged tissue at follow-up (FP). TN DSI values for GLM and RF corresponded with the degree of overlap between the acute perfusion-diffusion mismatch volume and non-infarcted tissue at follow-up (DSI=0.82±0.12). FN DSI values for GLM and RF were also comparable with DSI between the perfusion-diffusion mismatch and subsequently infarcted tissue (DSI=0.05±0.08).

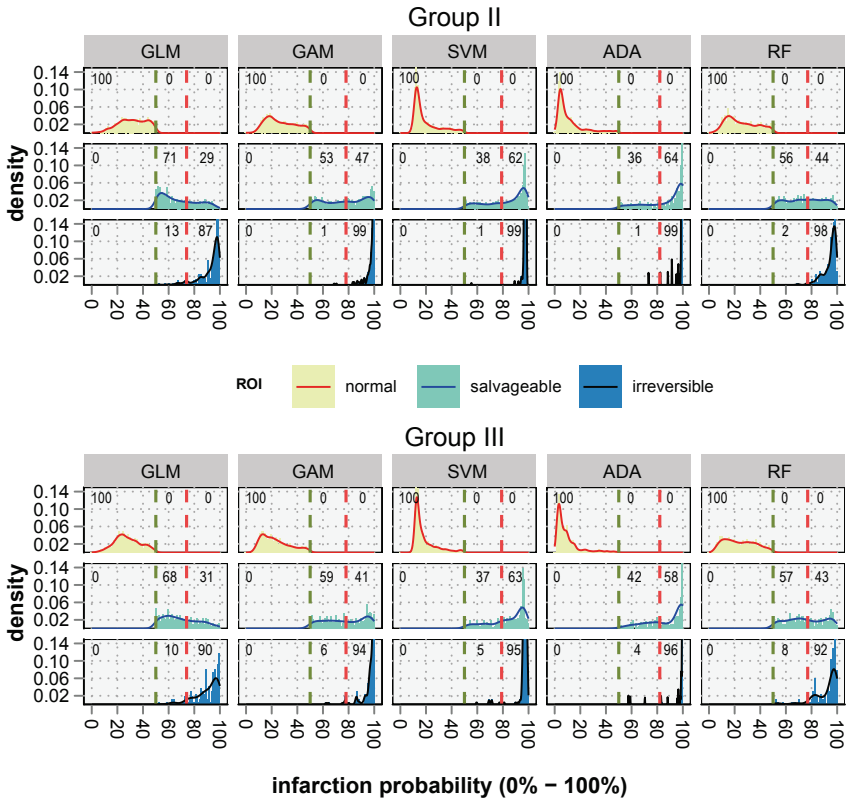

Figure 4.5. *Density plots of acute infarction probabilities calculated with GLM, GAM, SVM, ADA and RF in Groups II (A) and III (B). The plots show the distribution of infarction probability values (0-100%) in ipsilateral normal-appearing tissue ('normal'), potentially salvageable tissue ('salvageable'), and irreversibly damaged tissue ('irreversible'). Based on retrospective comparison between acute and follow-up tissue status, risk thresholds were determined that optimally differentiated between 'normal' and 'salvageable' (green dashed lines), and 'salvageable' and 'irreversible' (red dashed line). GLM, GAM, and RF allowed for larger differentiation between acutely predicted salvageable tissue and irreversibly damaged tissue than SVM and ADA. For GLM, GAM and RF the percentage of voxels that were actually salvaged and acutely predicted as salvageable (i.e. true negatives), was positively balanced compared with the percentage of voxels acutely derived as irreversibly damaged (i.e. false positives) (percentages at top of each facet). In contrast, ADA and SVM revealed a negative balance.*

SVM performed worst with lowest overlap for TN, and highest overlap of FP. Additionally, overlap of predicted irreversibly damaged and ultimate infarction at outcome (TP) was also lowest for SVM.

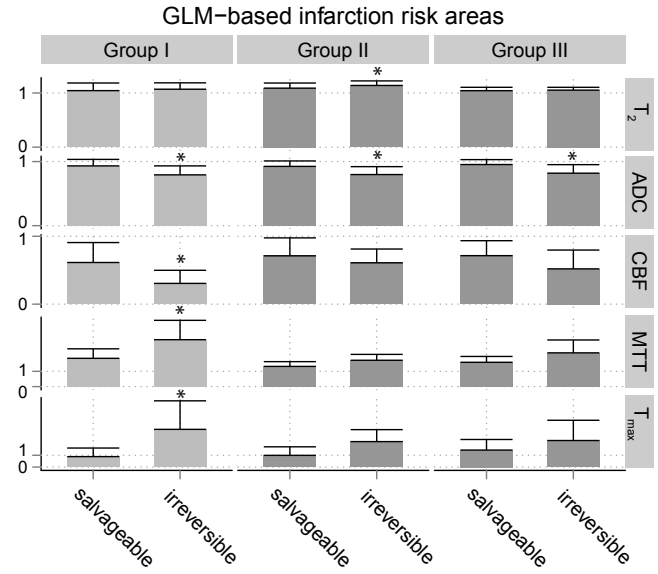

Figure 4.6. *Relative T_2, ADC, CBF, MTT, and T_{max} values (compared to normal appearing contralateral values) in GLM-predicted areas of irreversibly damaged (infarction probability >74%) or potentially salvageable tissue (infarction probability <74% but >50%) for Groups I, II and III within 2 h after stroke. *P<0.05 versus predicted salvageable tissue.*

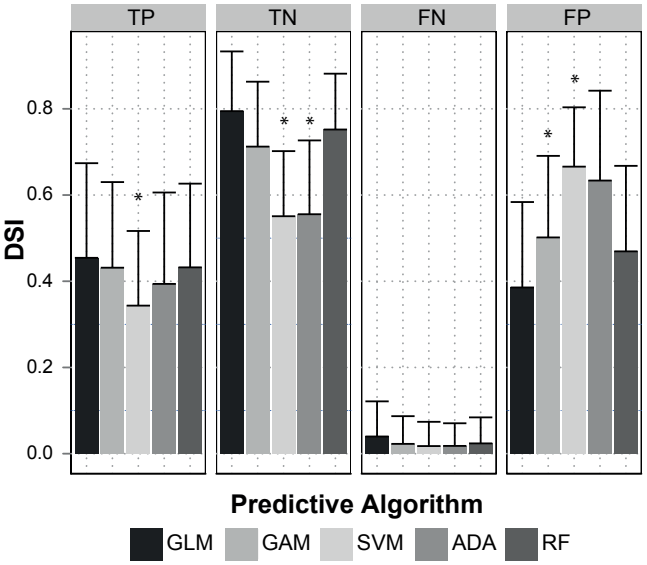

Figure 4.7. *Overlap, expressed as Dice's similarity index (DSI), between volumes of acutely predicted tissue fate – i.e. irreversibly damaged or potentially salvageable – from the five predictive algorithms (GLM, GAM, SVM, ADA, RF), and eventual outcome – i.e. infarction or salvaged – on follow-up scans. TP: true positive; FN: false negative. *P<0.05 versus GLM.*

Discussion

This study tested five different algorithms for early prediction of post-stroke tissue outcome, by evaluating accuracy in predicting brain infarction, and efficacy in differentiating potentially salvageable tissue from irreversibly damaged tissue. All algorithms performed equally well in acutely predicting the extent of tissue that infarcted chronically after permanent filament MCAo in rats. In a rat model of embolic stroke with subsequent spontaneous or rt-PA-induced reperfusion, it was shown that differences in the distribution of acutely predicted infarction risk values, particularly with GLM and RF algorithms, could be exploited to differentiate salvageable tissue from irreversibly damaged tissue.

Previous predictive modeling studies have speculated on the use of differences in spatial distribution of calculated infarction probabilities as a tool for selecting stroke patients eligible for therapeutic intervention (Wu et al., 2006) and/or for estimating potential treatment responsiveness. (Wu et al., 2007) It has, for instance, been suggested that the level of predicted infarction risk provides insight in the likelihood of reperfusion. (Wu et al., 2007) Our data demonstrate that tissue salvageability upon reperfusion is associated with the degree of infarction risk, which depends on the level of acute ischemic injury.

Algorithms were first trained in a model of permanent MCAo (Group I) to predict infarction when cerebral ischemia is sustained, i.e. without reperfusion that could reverse the progression of ischemic tissue injury. Animals in Groups II and III benefited from early spontaneous or rt-PA-induced reperfusion, which prevented lesion growth. Consequently, in contrast to Group I, follow-up infarctions were significantly smaller than the volume of acute perfusion loss. This allowed us to retrospectively identify potentially salvageable tissue from the acute MRI dataset, which we compared against the calculated probability of infarction modeled in Group I, i.e. if reperfusion would have been absent. Although algorithms were not perfect in predicting the final infarct (DSI<1.0), for each algorithm the calculated infarction probability of tissue that indeed became infarcted, was not significantly different between the three groups (Table 1), demonstrating the sensitivity and specificity of infarction probability calculation on underlying tissue status, with relative independence on differences in stroke models (e.g., filament vs. embolic MCAo), anesthesia (e.g., fentanyl citrate and fluanisone vs. isoflurane) and MRI settings (e.g., small variations in imaging parameters). In all groups infarction probability values reflected the degree of acute ischemic injury, expressed by perfusion reduction (high probability of infarction was associated with lowered CBF, and prolonged MTT and T_{max}) and tissue impairment (high probability of infarction was associated with lowered ADC and prolonged T_2).

In earlier studies, the findings of different correlations between acute brain tissue ADC (Jacobs et al., 2000) or perfusion (Sorensen et al., 1999b), and subsequent infarction – reflective of the complex, heterogeneous and dynamic nature of stroke pathophysiology – have raised the question whether nonlinear relations of acute tissue status and eventual outcome can be sufficiently captured with linear algorithms like GLM. (Østergaard et al., 2009; Wu et al., 2006, 2010) To that end SVM and GAM have previously been introduced, and the current study adds ADA and RF, as potentially more effective models for nonlinear relationships.(Østergaard et al., 2009; Huang et al., 2011)

Our study shows that the level and distribution of calculated infarction probability values can differ significantly between these types of predictive algorithms. Where SVM and ADA provided relatively smooth infarction probability maps, the distribution of risk values was more heterogeneous with GLM, GAM and RF. These differences may be related to the underlying method for discriminating infarcting from non-infarcting tissue. Regression models (GLM and GAM) and RF define a more direct relation of the training samples to the corresponding outcome. In ADA, and particularly in SVM, however, this relation is more indirect and aimed at iteratively optimizing the margin (dividing plane) that optimally separates infarcted from non-infarcted tissue in the training samples. (Bishop, 2007) Furthermore, SVM, originally a binary classifier, requires an additional conversion step to obtain probabilistic values, which may impose less accurate approximation of probability. (Bishop, 2007)
Nevertheless, the lack of significant differences between linear and non-linear algorithms in predicting the extent of infarction at follow-up, which is in line with previous studies in experimental settings (Huang et al., 2011, 2012) and in human patients (Gottrup et al., 2005), challenges the advantage of complex (non-linear) predictive algorithms for improved stroke outcome prediction. Our study suggests that the use of such algorithms may impose loss of additional information that could be of importance for further differentiation of heterogeneous tissue conditions. The distribution of infarction probabilities calculated with GLM, GAM or RF, was better linked to different tissue outcome, i.e. irreversibly damaged or salvaged. Nevertheless, it remains questionable whether any of these algorithms can fully capture the complexity of post-stroke tissue dynamics within a single algorithm, particularly when timings of stroke onset and reperfusion vary. We speculate that multiple or hierarchically arranged algorithms, each describing a different aspect of tissue outcome, might provide improved prediction estimates.(Bishop, 2007; Wu et al., 2010) Careful selection of training data (Jonsdottir et al., 2009), and incorporation of additional imaging or non-imaging biomarkers, such as tissue pH (Zhou et al., 2003), oxygen extraction fraction (An and Lin, 2000), artery occlusion site (Lansberg et al., 2008), or time after stroke onset, may further contribute to voxel-based stroke outcome predictions without increasing diagnostic complexity. (Wu et al., 2010)

In conclusion, we observed that different predictive algorithms are similarly effective in depicting tissue at risk of infarction. However, these algorithms had varying efficacy in differentiating between areas that were irreversibly damaged versus areas that could be salvaged after reperfusion. Our experimental stroke study allowed direct comparison between acute infarction predictions and ultimate tissue outcomes, and demonstrated that multiparametric MRI-based predictive modeling - with GAM, RF, and particularly GLM algorithms – enables discrimination between irreversibly damaged and potentially salvageable tissue. These predictive models performed equally well in identifying tissue amenable to reperfusion as compared to the perfusion-diffusion mismatch model. Added value of the statistical algorithms is provided by the quantitative information on infarction probability on a voxel-wise basis. Where assessment of tissue viability based on single indices and a single threshold is challenging (particularly in heterogeneous clinical settings), predictive algorithms give a quantitative likelihood of infarction or salvageability based on multiple parameters where each parameter describes a different aspect of the pathophysiological condition. This may contribute to more confident treatment decision-making and subsequent monitoring in the early stages of ischemic stroke. These predictive algorithms, which are readily applicable in preclinical and clinical settings, therefore provide promising means for treatment decision-making and treatment efficacy monitoring after acute ischemic stroke.

5

Prediction of post-stroke hemorrhagic transformation using MRI-based algorithms

Mark J.R.J. Bouts[1], Ivo A.C.W. Tiebosch[1], Umesh Rudrapatna[1], Annette van der Toorn[1], Ona Wu[2], and Rick M. Dijkhuizen[1]

[1] Biomedical MR Imaging & Spectroscopy Group, Image Sciences Institute, University Medical Center Utrecht, Utrecht, The Netherlands.
[2] Athinoula A. Martinos Center for Biomedical Imaging, Department of Radiology, Massachusetts General Hospital, Charlestown, MA, United States.

submitted for publication

Abstract

Estimation of risk of hemorrhagic transformation is crucial for treatment decision-making after acute ischemic stroke. This study aimed to determine the efficacy of multi-parametric MRI-based predictive algorithms in calculating probability of hemorrhagic transformation after experimental stroke.

Male spontaneously hypertensive rats were subjected to embolic stroke and, after 3 h, treated with recombinant tissue plasminogen activator (Group I: n=6) or placebo (Group II: n=7). Multiparametric MRI of brain tissue T_2, T_2*, diffusion, perfusion, and blood-brain barrier permeability, was done at 2, 24, and 168 h post-stroke. Generalized linear model (GLM) and random forest (RF) predictive algorithms were developed to calculate probability of hemorrhage and infarction based on acute MRI data, which was validated against outcome on MRI and histology after 7 days. Different classification accuracy measures, e.g. area-under-the-curve (AUC) of the receiver-operating characteristic and Dice's Similarity Index (DSI), were calculated to compare prediction efficacy of various prediction models.

Infarction and hemorrhagic transformation were predicted with high sensitivity and specificity. Highest accuracy of hemorrhage prediction was achieved with a RF-based model that included additional spatial features (Group I: AUC=0.85±0.14; Group II: AUC=0.89±0.09), with significant improvement over perfusion- or permeability-based thresholding methods. However, overlap between predicted and actual tissue outcome was significantly lower for hemorrhage prediction models (maximum DSI=0.20±0.06) as compared to infarct prediction models (maximum DSI=0.81±0.06).

Multiparametric MRI-based predictive algorithms enable early identification of post-ischemic tissue at risk of hemorrhagic transformation, and may contribute to improvement of safe and effective individualized therapeutic intervention after acute stroke.

Introduction

Despite its effectiveness in improving clinical outcome in patients suffering from acute ischemic stroke, the application of thrombolytic therapy with recombinant tissue plasminogen activator (rt-PA) is limited by strict (timing) guidelines. (Hacke et al., 2008; Wardlaw et al., 2012) It has been shown that patients receiving thrombolysis display a substantially increased risk of developing hemorrhagic transformation (odds ratio 4.55; confidence interval: 2.92-7.09) over a natural incidence of 15 to 26%. (Horowitz et al., 1991; Wardlaw et al., 2012) The potential benefit of thrombolytic treatment is therefore counterbalanced by a higher risk of hemorrhagic transformation, which further increases as time progresses. (Dijkhuizen et al., 2001) Nevertheless, some patients may still benefit from thrombolysis even well beyond 4.5 h after stroke onset. (Copen et al., 2009; Wardlaw et al., 2012) Individualized assessment criteria are therefore warranted to optimize inclusion or exclusion of patients for thrombolytic treatment.

Neuroimaging, and especially MRI, has shown to be effective in identifying areas of cerebral ischemia. Particularly, diffusion-weighted imaging –sensitive to early ischemic tissue changes– and perfusion-weighted imaging –sensitive to hemodynamic disturbances– have been considered as two potent means to identify tissue at risk of infarction. (Sobesky, 2012) Additionally, diffusion- and perfusion-weighted MRI may inform on risk of hemorrhagic transformation. Substantial reduction in tissue water diffusion (Selim et al., 2002), large initial lesion volume on diffusion-weighted MRI (Selim et al., 2002; Campbell et al., 2011; Lansberg et al., 2007), large area of perfusion loss (Albers et al., 2006), and regions with very low cerebral blood volume (Alsop et al., 2005; Campbell et al., 2010b), have all been proposed as indicators of increased risk of hemorrhagic transformation. In addition, early parenchymal signal enhancement on T_1-weighted MR images after injection of gadolinium-containing contrast agent administration, indicative of increased blood-brain barrier (BBB) permeability, may provide an early sign of hemorrhagic transformation. (Knight et al., 1998; Dijkhuizen et al., 2001; Neumann-Haefelin et al., 2002; Ding et al., 2006a; Hjort et al., 2008; Hoffmann et al., 2012) Nevertheless, as a single measure none of these MRI-based indices was able to reliably identify the tissue at risk of hemorrhage prior to thrombolytic treatment. (Alsop et al., 2005; Hoffmann et al., 2012; Kim et al., 2005)
It may be speculated that voxel-wise methods that combine different pathology measures would improve detection of tissue likely to hemorrhage. (Wu et al., 2010) Previous studies have demonstrated the ability of these methods in effectively calculating probability of infarction at a voxel level. (Chapter 4; Wu et al., 2001, 2007, 2010) Yet, the potential of predictive algorithms to signify tissue at risk of hemorrhagic transformation has not yet been evaluated. Hence this study aimed to determine the efficacy of

prediction models to estimate risk of hemorrhage after cerebral ischemia-reperfusion based on multiple MRI parameters. To that aim probability of hemorrhagic transformation and infarction were calculated from acute multiparametric MRI after embolic ischemic stroke in hypertensive rats, which we compared against final tissue outcome following rt-PA or placebo treatment.

Materials and methods

Animal model

All animal procedures were approved by the animal ethical and experimental care committee of the University Medical Center Utrecht and Utrecht University following the guidelines of the European Union's Council Directive. Male spontaneously hypertensive rats (Charles River, Germany), weighing 280-330 g were subjected to right-sided middle cerebral artery occlusion (MCAo) as previously described. (Zhang et al., 1997; Tiebosch et al., 2012) In brief, rats were endotracheally intubated and mechanically ventilated with 2% isoflurane in air:O2 (2:1). All animals received subcutaneous injection of gentamicin (5 mg/kg) as antibiotic, and 2.5 mL glucose solution (2.5% in saline) to prevent dehydration. During all procedures core temperature was kept at 37.5 ± 0.5 ˚C with a temperature-controlled heating pad. Thromboembolic stroke was induced after exposing the right carotid artery by a ventral incision in the neck. A modified catheter was advanced into the internal carotid artery towards the origin of the MCA. A homologous (25 mm long, 24 h old) blood clot was slowly injected followed by removal of the catheter. The wound was closed and animals were directly prepared for MRI (see below).

Immediately after the first MRI session, animals were treated with an intravenous infusion of saline (n=10, Group I) or 10 mg/kg rt-PA (Activase®, Genentech, concentrated to 3 mg/ml) (n=10, Group II), of which 10% was administered as a bolus, followed by continuous infusion of the remaining 90% over 30 minutes.

Postoperative care included subcutaneous injections (2 times) of 0.03 mg/kg buprenorphine for pain relief (Temgesic®,Ricket & Colman, Kingston-Upon-Hill, UK) and glucose (2.5%) in 2.5 mL saline. Animals were socially housed according to a 12 h lights-on lights-off protocol. During the three subsequent days after stroke, Ringer's lactate (0-1 mL, depending on amount of weight loss) was daily administered to compensate for excessive weight loss.

MRI of tissue status

Magnetic resonance imaging was conducted on a 4.7T animal MR system (Agilent, Palo

Alto, CA, USA). A 90 mm diameter in-house developed Helmholtz volume coil was used for radiofrequency excitation, and a 25 mm diameter inductively coupled surface coil for signal reception.

MR imaging was conducted immediately after MCAo, and again at 1 and 7 days after stroke. During MRI animals were restrained in a MR-compatible holder with earplugs and a tooth-holder, and continuously mechanically ventilated with 2% isoflurane in air:O_2 (2:1). Body temperature and expired CO_2 were monitored and kept within physiological range.

For all MRI acquisitions the field-of-view (FOV) was fixed to 32 x 32 mm^2, with a slice thickness of 1 mm. The MRI protocol consisted of multiple spin-echo T_2-weighted images (repetition time (TR) 3600 ms; echo time (TE) 12-144 ms; data matrix size 256 x 128 x 19) and multiple gradient-echo T_2*-weighted images (TR 1400 ms; TE 7-70 ms; data matrix size 256 x 128 x 19) acquired for reconstruction of quantitative T_2 maps and T_2* maps by non-linear least square fitting. (Van der Zijden et al., 2008) Maps of the apparent diffusion coefficient (ADC) were acquired after fitting the full-tensor of the diffusion matrix obtained by diffusion-weighted 8-shot echo planar imaging (echo planar imaging (EPI); TR 3500 ms; echo time (TE) 38.5 ms; b-values 0 and 1428 s/mm^2; 6 diffusion-weighted directions, data matrix size 128 x 128 x 19) (Van der Zijden et al., 2008). Dynamic susceptibility contrast-enhanced (DSC) MRI was acquired using gradient echo EPI (TR 330 ms; TE 25 ms; data matrix size 64 x 64 x 5) in combination with an intravenous bolus injection of 0.35 mmol/kg gadobutrol (Gadovist®, Schering, The Netherlands). Maps of cerebral blood flow (CBF), cerebral blood volume (CBV), mean transit time (MTT) and bolus peak time (T_{max}) were subsequently acquired by circular deconvolution of the tissue concentration curves with an arterial reference curve obtained from the contralateral hemisphere.(Wu et al., 2003) T_1-weighted images (gradient echo; TR 160 ms; TE 4 ms; data matrix size 256 x 128 x 19) were acquired to assess BBB integrity. T_1-weighted images were acquired every 2.73 min from just before up to 35 min after gadobutrol injection. T_1-weighted images were then used to calculate quantitative T_1 maps using:

$$S(TR) = S_0(1 - e^{-TR/T_1})e^{-TE/T_2*}$$

with S_0 as the estimated proton density obtained from the T_2 mapping routine and T_2* as calculated from the T_2* mapping routine. To compensate for differences in gain and reconstruction settings of the T_1-weighted versus T_2- and T_2*-weighted acquisitions, an extra scaling factor of 16.5 was used to achieve T_1 in normal ranges. (Haacke et al., 1999) R_1 ($1/T_1$) maps were subsequently used for estimation of the blood-to-brain transfer constant (K_i) and extravascular/extracellular volume (V_p) using the Patlak matrix analysis of compartmental dynamics with a plasma concentration estimate from the sagittal sinus (4 voxels) as reference. (Patlak and Blasberg, 1985; Ewing et al., 2003)

Histological assessment of intracerebral hemorrhage

Immediately after the final MRI session, animals were intraperitoneally injected with an overdose of pentobarbital followed by intracardial perfusion with cooled saline. Brains were extracted, cooled and cut in 2 mm slices. Subsequently, slices were placed in ice cold PBS and covered with a glass slide to allow for photography. Photographs were taken on a 1 mm grid, using a digital color camera (Moticam2300, Motic, Wetzlar, Germany) attached to binocular microscope. Digital images were then transferred to a separate workstation for visual assessment of extravascular blood disposition.

Image processing

T_2, ADC, perfusion parameter, and BBB index maps were spatially aligned to a common template acquired from six healthy rats using a non-rigid registration procedure. (Klein et al., 2010) Image analyses and group comparisons were carried out on four consecutive slices. Signal from non-parenchymal tissue was removed by using a mask obtained from the brain extraction tool (Smith, 2002). Signal from CSF was excluded after its identification as areas with T_2 values of more than 4.5 standard deviations (4.5σ) of normal-appearing contralateral gray matter calculated from averaged T_2 maps from all included animals. Coregistered maps were normalized against mean values of normal appearing contralateral gray matter regions, except for T_{max} maps that were normalized by subtraction of the derived mean values. (Wu et al., 2006) Mean contralateral gray matter values were calculated using a contralateral, CSF-excluded mask of the four consecutive slices. Infarcted tissue on post-stroke day 7 was automatically identified as voxels with T_2 values at least 2σ higher than mean contralateral gray matter values. Perfusion and BBB abnormalities at the acute stage were similarly identified on MTT and K_i maps, respectively. Diffusion abnormality was defined as 2σ lower than mean contralateral gray matter values on ADC maps. Abnormalities on CBV and CBF maps were similarly identified. Hemispheric lesion fractions were calculated by dividing the lesion volume by the volume of the ipsilateral hemisphere.
Hemorrhagic areas, characterized by clear hypointense signal, were outlined on the third echo image of the T_2*-weighted MRI dataset obtained at day 7 post-stroke. Manual outlines were created by two experienced MR researchers (R.D., M.B.) with the digital photography images as reference to prevent inclusion of non-hemorrhage-related susceptibility artifacts.

Predictive modeling

The acute MRI data of Group II (rt-PA-treated) animals with pre-treatment lesions and post-treatment hemorrhage and infarct after 7 days were used to train and evaluate algorithms for prediction of hemorrhagic transformation. Group I animals were used to

evaluate the effect of placebo treatment on lesion development in comparison to Group II animals. Group I animals were furthermore used to train and evaluate algorithms for prediction of infarction.

Tissue outcome was predicted using statistical algorithms that relates acutely acquired normalized MRI parameters (x = {rT2, rADC, rCBF, rCBV, rMTT, rT_{max}, rK_t, rV_p}) and possibly additional positional properties, i.e. the predictive features, to corresponding ultimate tissue status on follow-up MRI images after 7 days. MRI-based predictive algorithms can calculate, based on training data, an optimized set of rules that map a relation of samples from the acutely acquired images to a class that represents either ultimately affected tissue or a class that represents non-affected tissue. Subsequently, this set of rules can be used to estimate the probability of pathology (e.g., hemorrhagic transformation or infarction) ($P_{outcome} = P(outcome|x_1,..,x_m)$) from newly introduced samples. In this study various training sets were used to develop different types of predictive models to calculate probability of hemorrhagic transformation or infarction acutely post-stroke. A parametric generalized linear model (GLM) and a non-parametric Random Forest (RF) algorithm to predict hemorrhagic transformation were trained with acute multiparametric MRI data validated against intracerebral hemorrhage on post-stroke day 7 T_2*-weighted images (Hemorrhage Prediction Models A and B). In addition, GLM- and RF-based algorithms (Hemorrhage Prediction Models C and D) similar to Hemorrhage Prediction Models A and B, respectively, were developed with inclusion of additional spatial informative features. Spatial maps included voxel-wise distance to the brain border, distance from the ipsilateral temporal cortex, and edge-enhanced images for each included MRI map calculated from first order-derivative maps in the x, y and z directions using voxel-wise convolution with a first-derivative kernel. (Sonka et al., 2007) Examples of the included spatial feature maps are shown in Figure 5.1. Lastly, RF-based Infarction Prediction Models A and B were developed to calculate tissue infarction probability based on acute multiparametric MRI data and spatial features, similar to Hemorrhage Prediction Model D, validated against infarction on post-stroke day 7 T_2 maps.

The features of the training sets were presented to a previously introduced parametric GLM (Wu et al., 2001) and a non-parametric RF algorithm to estimate the probability of tissue injury at outcome ($P_{outcome}$) (Chapter 4; Breiman, 2001).

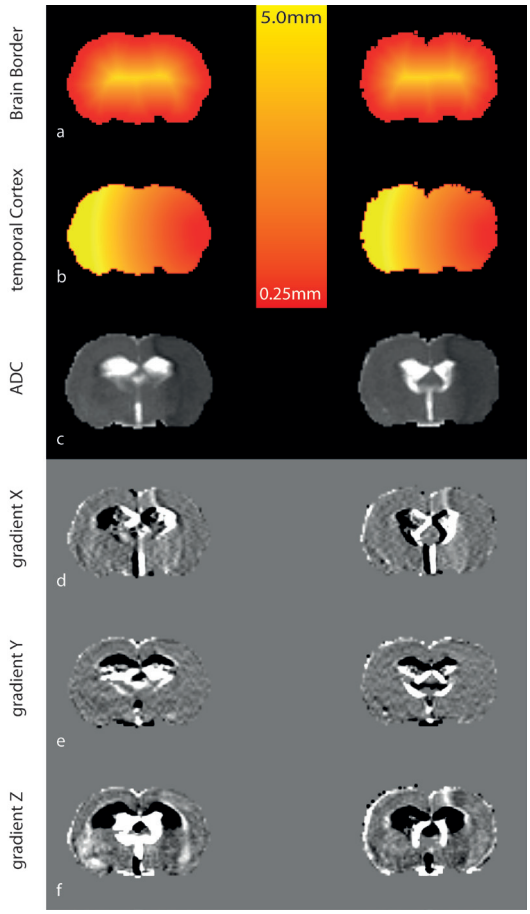

Figure 5.1. *Depiction of spatial features that were included in Hemorrhage Prediction Models C and D, and Infarction Prediction Models A and B. Distance (in mm) to brain border (a), and distance to the ipsilateral temporal cortex (b) were used as positional features, effectively operating as penalty terms to reduce false positives in the contralateral hemisphere. Gradient images as derived from acute parametric maps (for example ADC (c)) were calculated along the x, y and z direction (d, e, and f, respectively) as an extra contrast feature.*

GLM calculates the probability of tissue outcome using a logistic function:

$$P = \frac{1}{1 + e^{-\eta(x)}}$$

$\eta(x)$ is a linear link function that defines the relationship of M MRI parameters to tissue outcome at follow-up:

$$\eta(x) = \sum_{j=1}^{M} \beta_{jT} x_j + \alpha$$

with β describing the weights of each MRI parameter, and α the bias or intercept of the linear function. Coefficients α and β can be estimated using iterative reweighted least squares fitting. (Wu et al., 2001) RF is an ensemble algorithm that generates an aggregate result based on the outcome of multiple predictive algorithms. RF is based on a bootstrap aggregating approach in which multiple classification and regression trees (CART) are created by a randomized tree-building algorithm. During training, decision trees are grown from equally sized but modified subsets of the original training dataset. Further classification robustness is achieved by considering only a random subsample of the total available features for node splitting. This also provides feature importance calculation, ranking features in their degree of contribution to the prediction. The aggregate result of the algorithm is achieved by normalized majority vote over the multiple decision trees. Further details on RF and feature importance calculation can be found elsewhere. (Breiman, 2001) All predictive models were implemented in R. (R Development Core, 2011)

The predictive features that contributed to the prediction were selected by a recursive feature elimination cross-validation scheme. Feature combinations were iteratively fitted by presenting 1000 bootstrap samples of the total training data to a RF-based model. Each combination was evaluated by calculating the overlap between the classifier's predicted and actual outcome expressed by Cohen's Kappa measure.(Cohen, 1960) Features maximizing the overlap were preserved for the final RF predictor. Subsequently the number of features for node splitting (i.e. tries) was similarly considered based on the selected features; maximal Kappa determined the optimal number of tries. To evaluate the efficacy of the predictive algorithms within each training group (hemorrhage prediction: Group II; infarct prediction: Group I) cross-validation was conducted using a jack-knifing approach to prevent prediction bias. (Efron, 1987; Wu et al., 2007) Subsequent predictions in the test groups were based on an aggregate model calculated from the training group as a whole.(Chapter 4; Wu et al., 2007) Prediction accuracy was assessed by comparing the estimated hemorrhagic transformation probability to the follow-up T_2*-based hemorrhage, or the infarction probability to the follow-up T_2-based infarct. Probability maps were iteratively thresholded in step values of 1% ranging from 0-100%, and at each threshold, the voxels with correct and incorrect predictions of tissue pathology (i.e. hemorrhage or infarction) - true positives (TP) and false positives (FP), respectively - and absence of tissue pathology - true negatives (TN) and false negatives (FN), respectively - were calculated. This allowed calculation of model Sensitivity (snc) and Specificity (spc) (see Chapter 4).
Subsequently, Sensitivity and 1-Specificity were used for receiver-operating characteristic (ROC) statistics. Quantitative comparisons were provided by calculating the area-under-the-curve of the ROC (AUC). At a fixed probability threshold of 50%, the Youden's (*J*) index - defined as Sensitivity + Specificity -1 - was calculated to assess the

overall performance of the algorithms in classifying affected tissue. (Wu et al., 2007) *J* = 0 indicates a low diagnostic value, whereas *J* = 1 indicates a perfect diagnosis. Dice's Similarity Index (DSI) was calculated to express the overlap of predicted hemorrhagic or infarcting tissue and tissue that actually hemorrhaged or infarcted at follow-up. (Chapter 4; Dice, 1945). The accuracy of the predicted values was assessed using the root mean square error defined as:

$$RMSE = \frac{1}{N}\sqrt{\sum_{i=1}^{N}(y_i - p_i)^2}$$

N represents the total number of voxels, y_i the actual outcome at voxel *i*, and p_i the prediction. Where AUC and *J* aim at maximizing values (towards 1), RMSE aims at minimizing values (towards 0).

Data analysis and statistics

Predicted lesion volumes, expressed as volumetric fraction of the ipsilateral hemisphere (predicted lesion fraction), were calculated from GLM- or RF-based estimation of probability of hemorrhage or infarction exceeding 50%.

ROC analysis was extended by thresholding of brain tissue with lowered CBV or ADC from 2σ up to 5σ (steps of 0.5σ) below mean contralateral values. Thresholded maps were subsequently summed and normalized by the number of thresholds used. Sensitivity and Specificity, *J*, and DSI were calculated at the set threshold of 2σ. A similar strategy was applied for K_i with values above threshold (from 2σ from contralateral mean value).

Statistical analysis

Statistical testing of MRI parameters, prediction performance measures, and mean predicted probability of hemorrhage or infarction were compared with repeated measures ANOVA with post-hoc false discovery rate detection.

Results

Animal model

Out of 20 animals, two animals (Group I, n = 1; Group II, n = 1) developed subarachnoid hemorrhage and five animals (Group I, n = 2; Group II, n = 3) did not display cerebral hypoperfusion at the first MRI time-point. These animals were therefore excluded from this study. All but three (Group I, n = 1; Group II, n = 2) of the remaining thirteen animals, showed signs of reperfusion, i.e. more than 40% increase in cerebral blood flow from the acute to the 24 h time-point. All but one animal (Group I, n = 1) had developed intracerebral hemorrhage at the final time-point of imaging (day 7 post-stroke).

MRI of tissue status

Figure 5.2 shows maps of acute ADC, CBF, CBV, MTT and K_i from a rat prior to placebo treatment (upper row) and a rat prior to rt-PA treatment. Follow-up imaging revealed infarcted tissue (as characterized by prolonged T_2) and hemorrhagic tissue (as characterized by reduced T_2*-weighted signal intensity). Acute tissue perfusion and diffusion indices in subsequently infarcted and hemorrhagic areas were significantly different from contralateral values, except for CBV in hemorrhagic regions, as shown in Figure 5.3. K_i and V_p were not statistically different between infarcting or hemorrhagic areas as compared to contralateral tissue. T_{max} was significantly longer in subsequently hemorrhagic areas than in infarcting areas .

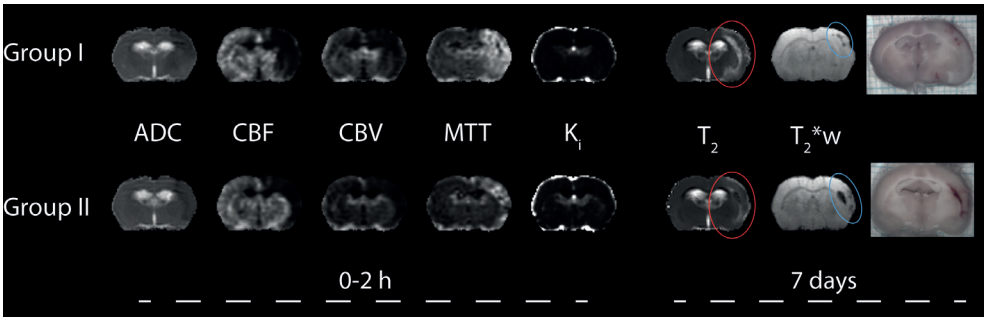

Figure 5.2. *Images of coronal slices of a rat brain from the placebo-treated (upper row) and rt-PA-treated group (lower row). Acute (2 h post-stroke; before treatment) maps of diffusion (ADC), perfusion (CBF, CBV and MTT), and BBB permeability (K_i) indicate tissue abnormality as a result of ischemia (lowered diffusion, reduced perfusion and occasionally increased BBB leakage). Follow-up MRI and histology after 7 days displayed infarcted tissue (characterized by prolonged T_2) (red ellipses) and intracerebral hemorrhage (characterized by reduced T_2*-weighted signal intensity (blue ellipses), and parenchymal blood accumulation).*

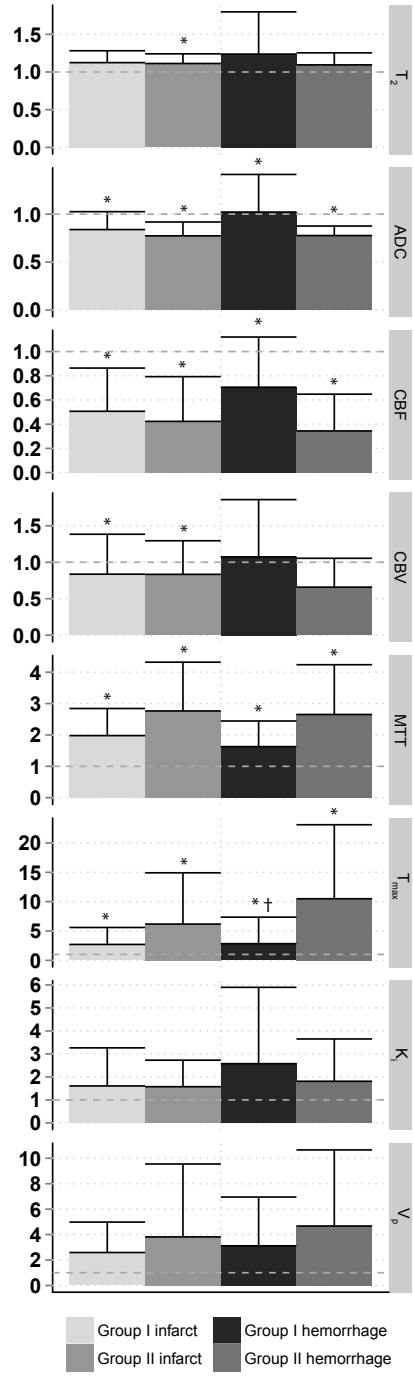

Figure 5.3. *Acute pre-treatment MRI parameter values, relative to mean contralateral gray matter values, of infarcted and hemorrhagic regions at follow-up. *P<0.05 versus contralateral; †P<0.01 versus infarct.*

The hemispheric hemorrhagic volume fractions were 0.04 ± 0.04 in Group I and 0.05 ± 0.02 in Group II, while hemispheric infarct volume fractions were 0.42 ± 0.10 (Group I) and 0.40 ± 0.10 (Group II), at 7 days after stroke. Hemispheric volume fractions of acutely lowered CBV had similar sizes as subsequent hemorrhagic volumes (0.08 ± 0.11 (Group I) and 0.04 ± 0.04 (Group II)), whereas hemispheric volume fractions with elevated K_i or lowered ADC and CBF were somewhat larger (Group I: 0.14 ± 0.07 (K_i), 0.29±0.14 (ADC), and 0.21 ± 0.19 (CBF); Group II: 0.15 ± 0.09 (K_i) , 0.35±0.13 (ADC), and 0.20 ± 0.12 (CBF)).

Predictive modeling

Thresholding of the volumes with abnormal ADC, CBV, and K_i revealed overlap with areas with subsequent hemorrhagic transformation (Figure 5.4). Prediction accuracy measures are summarized in Table 5.1. AUC, *J* and Sensitivity were highest for ADC-based thresholding. However, CBV- and K_i-based thresholding resulted in highest Specificity values.

Predictive algorithms, trained with data from Group II animals, provided four prediction models to calculate probability of hemorrhagic transformation. Feature selection in RF-based Hemorrhage Prediction Model B provided the highest degree of overlap between predicted and actual outcome with inclusion of all MRI parameters and 2 random variables per node split. Importance ranking of the predictive features revealed largest contribution of rADC, rCBF and rCBV, and lowest contribution of rK_i (Table 5.2). The contribution of spatial features to the prediction of hemorrhagic transformation in Hemorrhage Prediction Model D was strongly dependent on the features being used. We found that prediction accuracy remained relatively stable with inclusion of more than 12 features with 3 random variables per node split. We therefore selected the 12 top-ranked features for prediction in Hemorrhage Prediction Model D. Analysis of the spatial features revealed a substantial contribution of voxel-wise distance from the ipsilateral temporal cortex, and a z-directional gradient in the acute ADC map, in addition to rADC, rCBF and rCBV (Table 5.2). Subsequently, spatial features were also used in a GLM-based Hemorrhage Prediction Model C to allow for comparison of all prediction models.

Table 5.1. Prediction accuracy for ADC, CBV, and K_i thresholding and hemorrhage prediction models

Model	Group	AUC	J	Sensitivity	Specificity	DSI	RMSE
ADC[thres]	I	0.75±0.11‡	0.51±0.21	0.64±0.24‡§	0.86±0.05§	0.13±0.07	NA
	II	0.75±0.11‡§	0.54±0.11‡§	0.70±0.12‡§	0.83±0.09	0.18±0.07	NA
CBV[thres]	I	0.65±0.14	0.29±0.28	0.33±0.31†	0.96±0.05†	0.13±0.12	NA
	II	0.54±0.06†	0.09±0.11†	0.11±0.12†	0.99±0.01	0.11±0.11	NA
K_i[thres]	I	0.51±0.03†	0.02±0.07	0.11±0.07†	0.92±0.02	0.04±0.04	NA
	II	0.53±0.07†	0.05±0.14†	0.17±0.20†	0.88±0.07	0.05±0.06	NA
Model A	I	0.79±0.16‡	0.47±0.29	0.69±0.32‡	0.78±0.06‡§	0.11±0.05	0.42±0.06
	II	0.83±0.07‡§	0.51±0.12‡§	0.80±0.21‡§	0.70±0.11	0.18±0.07	0.47±0.10
Model B	I	0.77±0.20	0.37±0.29	0.67±0.33‡	0.70±0.08‡+§||	0.13±0.05	0.45±0.06
	II	0.83±0.07‡†§||	0.59±0.08‡§	0.80±0.18§	0.70±0.14	0.20±0.06*	0.44±0.12
Model C	I	0.86±0.08‡	0.51±0.26	0.71±0.30‡	0.80±0.05‡§	0.10±0.05	0.41±0.05
	II	0.90±0.02‡†§	0.65±0.24§	0.86±0.30‡§	0.78±0.08	0.17±0.06	0.42±0.09
Model D	I	0.85±0.14‡	0.53±0.30	0.67±0.35‡	0.86±0.06	0.12±0.05	0.36±0.06
	II	0.89±0.09‡†§	0.62±0.24§	0.76±0.32§	0.84±0.09	0.19±0.04*	0.36±0.10

*P<0.05 versus Group I; †P<0.05 versus ADC[thres]; ‡P<0.05 versus K_i[thresh]; §P<0.05 versus CBV[thresh]; || versus model D; NA: not applicable.

Table 5.2 Importance ranking of the features in the random-forest based models for infarct and hemorrhage prediction

Hemorrhage Prediction Model B		Hemorrhage Prediction Model D		Infarct Prediction Model D	
Feature	Relative Importance	Feature	Relative Importance	Feature	Relative Importance
rADC	100.0	rADC	100.0	rADC	57.9
rCBF	76.4	rCBF	87.6	rCBF	22.0
rCBV	66.9	Dist tCx	70.4	Dist tCx	100.0
rV_p	21.9	rCBV	64.7	rCBV	13.4
rT_{max}	13.5	rV_p	24.5	rV_p	18.2
rMTT	0.1	rT_{max}	17.5	rT_{max}	37.4
rT_2	0.0	Dist BB	16.4	Dist BB	41.0
rK_i	0.0	rMTT	12.6	rMTT	27.0
		rV_{pz}	11.7	rV_{pz}	5.5
		$rADC_z$	7.3	$rADC_z$	0.9
		rT_2	7.2	rT_2	48.6
		$rCBF_x$	2.9	$rCBF_x$	5.3
		$rCBF_y$	0.0	$rCBF_y$	0.0

Importance ranking scaled between most contributing (100%) and least contributing feature (0%) of the aggregate trained models. Dist tCx: distance to ipsilateral temporal cortex, Dist BB: distance to brain border, ADC_z: gradient of ADC map in z-direction, CBF_x: gradient of CBF map in x direction, CBF_y: gradient of CBF map in y direction, V_{pz}: gradient of extravascular space map in z direction

Figure 5.4 shows that Hemorrhage Prediction Models A and B were able to identify tissue that subsequently hemorrhaged, however GLM-based Model A also assigned increased probability values to contralateral regions without hemorrhagic transformation, which was also observed for the thresholding methods. Inclusion of spatial features in Hemorrhage Prediction Models C and D improved specificity of hemorrhage prediction. However only RF-based Model D demonstrated accurate ipsilateral specificity of predicted hemorrhagic area, which largely matched with actual intracerebral hemorrhage at follow-up. The ROC curve of the pooled predictions of Hemorrhagic Prediction Model D clearly dominated those of the other models (Figure 5.5). Table 5.1 shows that incorporation of spatial features in the RF-based Model D resulted in increased AUC and reduced RMSE.

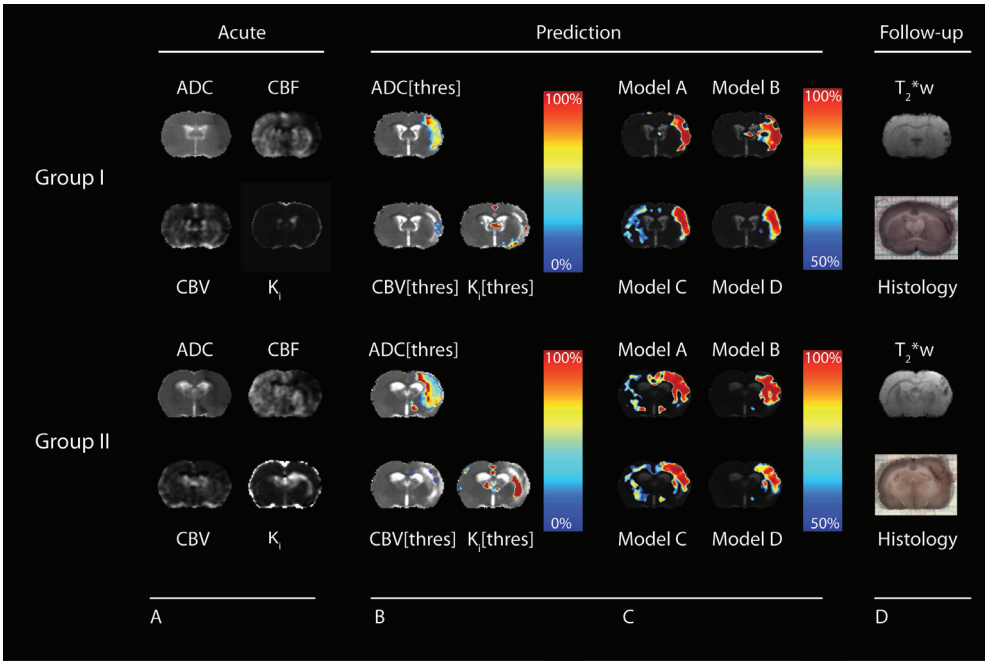

Figure 5.4. *Maps of acute ADC, CBF, CBV and K_i (panel A), with corresponding 7 days post-stroke T_2*-weighted images and histological tissue sections (panel D) of placebo- (Group I) and rt-PA-treated rats (Group II). Thresholded maps were voxel-wise summed and normalized between 0 and 100%, and overlaid on 7 day follow-up T_2 maps (panel B). Thresholding of abnormal CBV showed most specific matching with subsequent hemorrhagic regions, as compared to K_i- and ADC-based thresholding. Of the predictive models, Hemorrhage Prediction Model D (RF-based), which included MRI parameters as well as spatial features, demonstrated most optimal matching with ultimately hemorrhagic areas. Hemorrhagic probabilities above 50% are overlaid on 7 day follow-up T_2 maps (panel C).*

Voxel-wise predictive models mostly improved prediction accuracies as compared to the thresholding approaches (see Table 5.1). Highest Sensitivity, however, was achieved with CBV-based thresholding. Despite these high classification scores, actual overlap between the predicted hemorrhagic area and the area that truly hemorrhaged (expressed by DSI) was relatively low for all tested models.

To further assess the two best performing Hemorrhage Prediction Models C and D, assigned hemorrhagic probability values were evaluated in areas of acutely predicted and ultimately actual hemorrhage (TP), acutely predicted and ultimately no hemorrhage (FP), acutely no predicted and ultimately actual hemorrhage (FN), and acutely no predicted and ultimately no actual hemorrhage (TN). As expected, probability values of TP regions were significantly increased over risk values in FN and TN regions for both models. However, only for Hemorrhage Prediction Model D we observed significantly higher probability values in TP regions as compared to FP regions (repeated

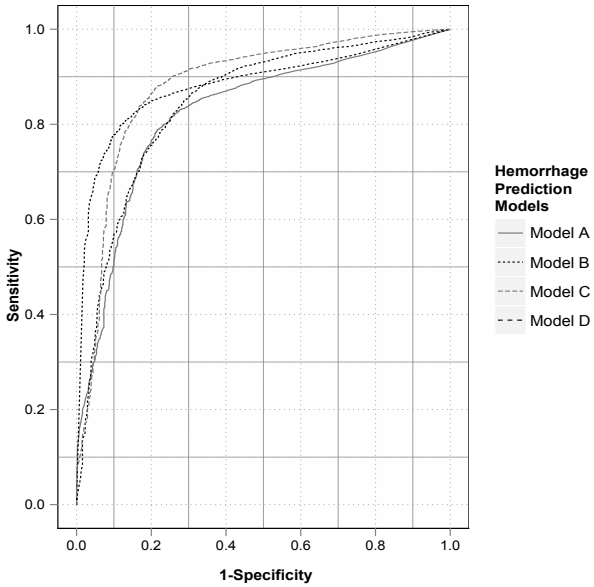

Figure 5.5. *ROC curves reflecting the performance in predicting tissue outcome for the four Hemorrhage Prediction Models for the Group II (training) cohort. All models included acute MRI-based measures of T_2, diffusion, perfusion, and BBB leakage. Additional spatial information was included in Hemorrhage Prediction Models C and D. Larger area under the curve indicates better performance.*

measures ANOVA: Group I, $P < 0.05$; Group II, $P < 0.05$). Furthermore, probability values in TN regions were most deviant from probability values in FN regions for Hemorrhage Prediction Model D with statistical significance for Group II ($P < 0.05$), and a trend for Group I ($P = 0.06$) (Figure 5.6).

In the animal without follow-up hemorrhage, the area with acutely predicted hemorrhagic transformation was minor (Figure 5.7). Model D-calculated hemorrhagic probability of the 50%-thresholded area in this animal was substantially lower than the mean probability in all other animals (56 ± 6% versus 76 ± 5%). Nevertheless, predictive models generally overestimated the tissue at risk of hemorrhage (Wilcox signed rank sum test (with false discovery rate detection), $P < 0.05$ compared to ultimate hemorrhagic volume). Model D-based 50%-thresholded probability maps showed a smaller degree of overestimation (50%-thresholded volume fraction Group I: 0.29 ± 0.12 ($P = 0.01$); Group II: 0.33 ± 0.17 ($P = 0.07$)) than Model C-based maps (Group I: 0.39 ± 0.08; Group II: 0.46 ± 0.15).

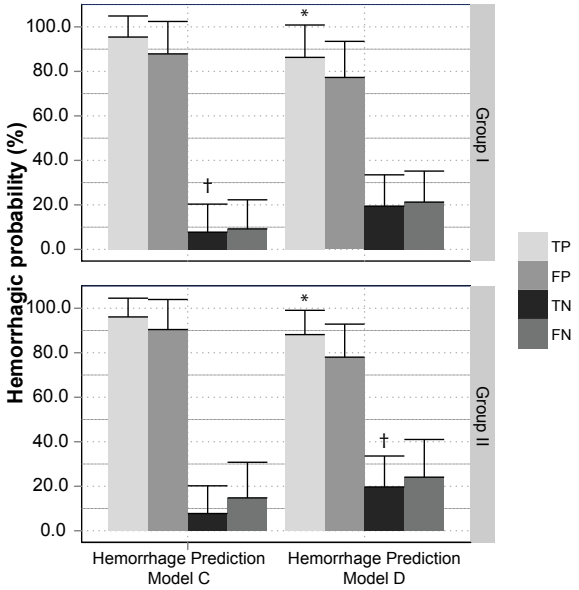

Figure 5.6. *Assigned hemorrhagic probability values of Hemorrhage Prediction Models C and D in TP, FP, TN, FN regions for hemorrhage in Group I and Group II rats. Mean calculated hemorrhagic probability in TP regions was significantly higher than that in FP regions for Hemorrhage Prediction Model D in both treatment Groups. This was not observed for Hemorrhage Prediction Model C. Mean hemorrhagic probability in TN regions was significantly lower in Model C-based predictions for Group I, and in Model D-based predictions for Group II – with a trend for Group I (P=0.06). *P<0.05, TP versus FP. †P<0.05, TN versus FN.*

To evaluate the models' accuracy to predict hemorrhagic transformation, we compared their performance with similar infarction prediction models. Based on the best performing Hemorrhage Prediction Model (i.e. Model D), an RF-based Infarct Prediction Model that included MRI parameters and spatial features was trained with data from the placebo-treated animals (i.e. Group I), representing 'normal' infarction development (Infarct Prediction Model A). Since infarct volumes were much larger than hemorrhage volumes, we also tested the Infarction Prediction Model with a restricted number of voxels, equaling the number of voxels (i.e. 1200) used in the Hemorrhage Prediction Models (Infarct Prediction Model B). Figure 5.8 shows examples of prediction of infarction in a placebo-treated animal (A) and a rt-PA-treated animal (B). Table 5.3 lists the prediction accuracy measured for both Infarction Prediction Models. Both models were equally accurate in predicting infarction with significantly higher DSI values compared to the Hemorrhage Prediction Models (Group I: $P < 0.01$; Group II: $P < 0.01$).

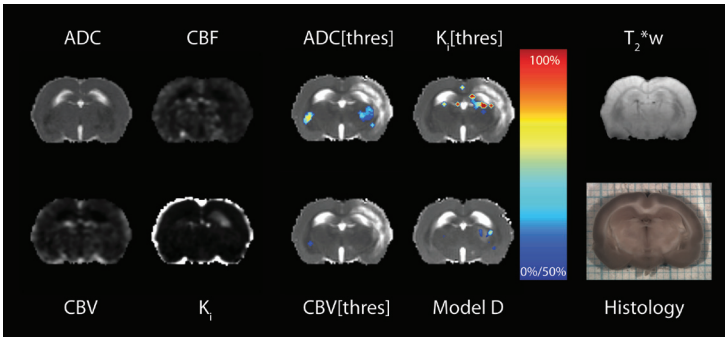

Figure 5.7. *Maps of acute ADC, CBF, CBV, and K_i with subsequent 7 day post-stroke T_2*-weighted image and histological section of a placebo-treated rat without hemorrhagic transformation. Hemorrhage probability (overlaid on 7 day follow-up T_2 maps) was calculated by means of ADC, CBV or K_i-based thresholding (normalized incidence: 0-100%), or using Hemorrhage Prediction Model D (50-100%).*

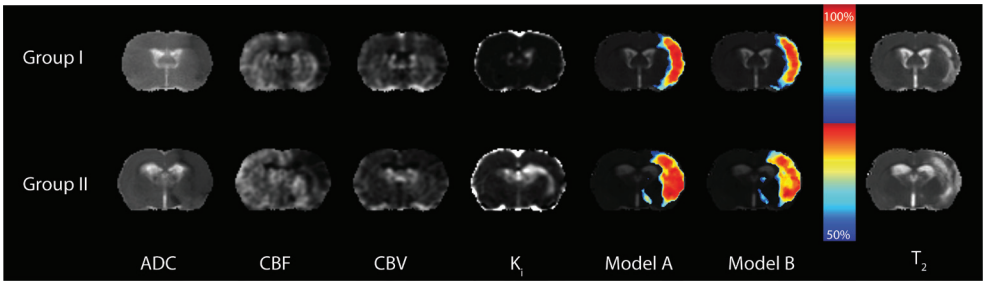

Figure 5.8. *Maps of ADC, CBF, CBV, K_i, and calculated infarction probabilities (from Infarction Prediction Models A and B) in rat brain acutely after unilateral stroke, and follow-up T_2 map at day 7 for a placebo- (Group I) and rt-PA-treated animal (Group II). Infarction Prediction Models (RF model based on MRI parameters and spatial features) were trained with inclusion of all infarcted voxels (Model A), or a reduced number of samples (i.e. 1200 voxels; Model B) comparable to the Hemorrhage Prediction Models. The area of predicted infarction corresponded well with the actual ultimate infarct, with high similarity between the two models.*

Discussion

In our study we aimed to determine the efficacy of MRI-based voxel-wise predictive algorithms to identify tissue at risk of developing secondary hemorrhage after acute ischemic stroke. In an established animal model of stroke with reperfusion-induced hemorrhagic transformation, we found that individualized maps of hemorrhagic probability can be effectively obtained from a combination of MRI parameters, with highest accuracy when calculated with a RF-based supervised algorithm.

Table 5.3. Accuracy measures of infarct prediction models

	Infarct Prediction Model A		Infarct Prediction Model B	
Group	I	II	I	II
AUC	0.94 ±0.02	0.92±0.08	0.94 ±0.02	0.91±0.09
J	0.74±0.09	0.70±0.22	0.73±0.09	0.70±0.23
Sensitivity	0.84±0.11	0.84±0.11	0.83±0.22	0.84±0.23
Specificity	0.90±0.02	0.87±0.02	0.90±0.02	0.86±0.02
RMSE	0.29±0.02	0.31±0.02	0.31±0.01	0.33±0.02
DSI	0.81±0.06	0.76±0.18	0.81±0.06	0.75±0.19

Earlier studies heralded the use of MRI as a potential tool for elucidating tissue at risk of hemorrhage. For example, very low CBV within the area of diffusion abnormality (Alsop et al., 2005; Campbell et al., 2010b), or voxel-wise combinations of abnormal ADC with T_{1sat} or T_2 (Ding et al., 2005) have been associated with increased likelihood of hemorrhage after acute ischemic stroke. In these studies viability thresholds were calculated to determine tissue outcome, subsequently generating discrete tissue theme maps depicting tissue at risk. Our study moves forward by: 1) including multiple (more than 2) MRI-based parameters of hemodynamic and tissue status, as well as spatial features; 2) ruling out assumptions on viability thresholds; and 3) calculating a probabilistic rather than discrete output. 4) Furthermore our experiments were conducted under reproducible and controllable conditions using a clinically relevant animal model.

Previously, supervised MRI-based prediction methods have been successfully employed to calculate probability of tissue infarction after acute clinical (Wu et al., 2001) or experimental stroke.(Chapter 4; Wu et al., 2007) We have recently shown in normotensive rat stroke models that GLM- and RF-based predictive algorithms allow distinction of potentially salvageable tissue from the heterogeneity in the distribution of infarct probabilities (Chapter 4). These two algorithms were also employed in the current study, and conformably high accuracy in predicting tissue infarction was attained in a stroke model with spontaneously hypertensive animals. Importantly, reduction of the training data samples (i.e. image voxels) to a number comparable to the sample size in the hemorrhage prediction models did not significantly affect the prediction efficacy. The presented multiparametric MRI-based algorithms were used to develop hemorrhage prediction models that improved prediction of hemorrhagic transformation over thresholding of single indices like K_i or CBV. Particularly for RF-based models, specificity of the prediction improved with inclusion of spatial features that guided voxel-wise classification. This has also been observed in other studies where spatial

lesion distribution maps increased accuracy of prediction of tissue infarction.(Huang et al., 2010, 2011) However, infarct distribution depends on many factors, such as vascular occlusion site (Chapter 3; Fiehler et al., 2005), type of occlusion (Liu et al., 2009), and the duration of occlusion (Chapter 2; Wardlaw et al., 2012), which may be challenging to derive *a priori* in clinical practice. Therefore we employed more general spatial features, such as distance from the brain border or distance from the temporal cortex, which can be unbiasedly derived from each individual subject.
Our results show a difference in distribution of probability values between GLM- and RF-based predictive algorithms. Probability values in falsely predicted hemorrhagic tissue were significantly lower than values in correctly predicted hemorrhagic tissue, when calculated with RF-based algorithms, which was not the case for GLM-based predictions. This difference may arise from the assumed linear progression of injury from initial imaging towards actual outcome in GLM, an assumption which is less strict in the piece-wise linear RF model.

Despite the high prediction accuracies of our models, the actual overlap of the predicted hemorrhagic area and the actual hemorrhage was relatively low. Although regions with predicted hemorrhagic transformation resided in close proximity to ultimately hemorrhagic areas (as reflected by measures of specificity and sensitivity), all tested prediction methods overestimated the tissue at risk of hemorrhage. Previous studies reported on a 'compelling' correspondence between areas of projected hemorrhagic transformation and the actual hemorrhage, but did not effectually quantify the exact spatial correspondence. (Neumann-Haefelin et al., 2002; Alsop et al., 2005; Ding et al., 2006b; Campbell et al., 2010b) Underestimation of the actual extent of hemorrhage may partly explain incomplete matching. Indefinite matching between early imaging markers and subsequent hemorrhagic development has also been observed by others, reporting an insignificant correspondence of early contrast-induced signal enhancement with subsequent hemorrhagic transformation. (Rozanski et al., 2010; Campbell et al., 2011) Our study particularly focused on gross hemorrhages identified as a local signal intensity reduction on T_2*-weighted images, caused by the magnetic susceptibility effect of deoxygenated blood, histologically verified from clear blood accumulation on post mortem brain sections acquired directly after the final MRI session. Mild or microscopic hemorrhage may have remained undetected especially when obscured by edema-associated T_2 prolongation. (Dijkhuizen et al., 2001)

The development of hemorrhagic transformation is strongly associated with increased permeability of the BBB. (Zoppo et al., 1998) MRI of early parenchymal enhancement as a result of leakage of contrast agent (i.e. gadolinium chelate) over the BBB has been shown to be predictive of development of hemorrhagic transformation in animal stroke models (Knight et al., 1998; Dijkhuizen et al., 2001; Neumann-Haefelin et al., 2002;

Ding et al., 2006b) and human stroke patients. (Warach and Latour, 2004 ;Kim et al., 2005; Bang et al., 2007; Hjort et al., 2008; Kastrup et al., 2008) Yet in the current study, increased extravasation, reflected by elevated K_i, was only occasionally observed and was not necessarily associated with the hemorrhagic area. Our study aimed at identifying tissue likely to develop hemorrhagic transformation within a short, acute time-window of less than 3 h post-stroke, which may have been too early for progression of significantly elevated BBB permeability. (Yang and Betz, 1994; Zoppo et al., 1998) Furthermore, low perfusion, particularly in regions with severe CBV reductions (i.e. with increased risk of hemorrhagic transformation), may have restricted local contrast agent arrival despite potential presence of leaky vessels. Likewise, other studies have also reported limitations of the accuracy of BBB permeability measurements to predict successive hemorrhage. (Neumann-Haefelin et al., 2002; Ding et al., 2006b; Rozanski et al., 2010)

Additional pathophysiological processes, such as spontaneous reperfusion with subsequent hyperperfusion (Alsop et al., 2005; Pan et al., 2007) and inflammation (Zoppo et al., 1991; Pan et al., 2007; Rosell et al., 2008), which typically occur at later time-points, can significantly exacerbate vessel wall integrity and accelerate hemorrhagic transformation. Furthermore, other factors like age, co-morbidities, and medication may considerably increase risk of bleeding. Inclusion of such additional (non-imaging) features in predictive algorithms may contribute to improved accuracy of prediction of hemorrhagic transformation after acute ischemic stroke.

Although our study involved a relatively small sample size, which may have reduced statistical power, our findings clearly demonstrate an increased sensitivity in predicting areas at risk of hemorrhagic transformation with voxel-wise MRI-based prediction models. This further extends the potential of these models, which have been successfully applied to predict tissue at risk of infarction (Wu et al., 2001, 2006, 2007) and to identify tissue amenable for reperfusion therapy (Chapter 4; Tiebosch et al., 2012), to inform on potential adverse effects of thrombolytic treatment after stroke. Since these algorithms can be readily applied in clinical practice, they may open up opportunities for further improving individualized care, where careful identification of presence and location of risk of hemorrhage can be critical for safe and effective intervention in acute ischemic stroke patients. (T.I.S. investigators, 2006; Campbell et al., 2010b)

6

General Discussion

Acute therapy in ischemic stroke aims at resolving the cerebral ischemic state by reestablishing the supply of valuable oxygen and nutrients to the affected tissue. To date the only effective drug approved for early treatment of ischemic stroke is recombinant tissue plasminogen activator. However its usability is limited to a strict time window of at most 4.5 hours after stroke. (Hacke et al., 2008; Wardlaw et al., 2012) After which, restoration of oxygen supply and glucose delivery may promote inflammatory responses, edema formation or subsequent development of hemorrhage. (Warach and Latour, 2004; Pan et al., 2007). In recent years it has become more apparent that selecting patients solely based on time may be ill-posed and that more patients would benefit from thrombolysis when recruitment was based on a more individualized basis. (Thomalla et al., 2006) Prediction of tissue outcome after ischemic stroke deals with a careful balance between tissue likely to respond favorably to reperfusion therapy versus tissue for which reperfusion therapy might further exacerbate tissue injury. Stroke as a disease of altered cerebral hemodynamics involves local metabolic, hemostatic, and vascular changes - either primary or secondary to the ischemic injury - which alterations depend on the time after disease onset. All changes are predictive as a single factor but - since they operate in conjunction - boost predictive power as a collection. (Warach, 2001)

Neuroimaging has taken a strategically important position in the early diagnosis of patients suffering from ischemic stroke. Its ability to allow for non-invasive and repetitive assessment, while informing on many of the above described aspects, makes it an indispensable tool for treatment planning and disease management. Particularly the use of MRI and specifically diffusion-weighted imaging and perfusion-weighted imaging, has shown to be effective for the early detection of tissue at risk of infarction. The mismatch between tissue volumes with abnormal diffusion and perfusion has been advocated as a simple and effective tool for identifying the penumbral tissue. (Jansen et al., 1999; Kidwell, 2013) Yet debates on the reversibility of the presumed irreversibly damaged lesion with diffusion abnormality (Kidwell et al., 2000; Fiehler et al., 2002; Kranz and Eastwood, 2009; Campbell et al., 2012) or the inability of specifically discriminating the penumbral tissue (Kidwell et al., 2003; Kane et al., 2007a), have led to the introduction of alternatives like the MR angiography–diffusion mismatch, a concept derived from CT imaging where a discrepancy between a small diffusion lesion volume and a considerably affected perfusion territory, might identify those likely to benefit from reperfusion therapy. (Lansberg et al., 2008; Goyal et al., 2013) Yet, neither perfusion-diffusion mismatch nor MR-angiography diffusion mismatch informs directly on the duration of stroke. The perfusion-diffusion mismatch may sustain for longer periods of time (Copen et al., 2009), but it remains unclear whether this is due to sustained perfusion levels preserving tissue architecture, or that the diffusion or perfusion lesion

volumes expand alike due to slow failure of the collateral flow and lesion expansion due to peri-lesional spreading depolarizations. (Heiss, 2010) Therefore additional imaging information that aid in staging of the stroke, may improve tissue prediction by informing on infarct progression. (Wu et al., 2011; Goyal et al., 2013) However, as the number and complexity of different imaging approaches increases, so does the interpretability of its derived metrics, especially when these metrics need to be combined to inform on potential tissue injury progression after stroke. Voxel-wise multiparametric analysis methods have been suggested as a promising alternative, integrating the above described aspects of stroke within a single index without increasing diagnostic complexity. (see for review (Østergaard et al., 2009; Wu et al., 2010)) Yet, their potential as a tool for predicting different tissue outcomes has been proven to a limited extent. The main objective of this thesis was to elucidate the potential of voxel-based models for the prediction of variable tissue outcome after stroke. To that aim, various voxel-based statistical models were evaluated in their potency of tissue progression monitoring and tissue outcome prediction, based on serially acquired multiparametric MRI data in experimental animal models of stroke.

The studies in this thesis focused on the voxel-wise identification and prediction of tissue changes after experimental stroke. The use of non-invasive MR imaging to assess the initial injury and its progression allowed for prediction and subsequent validation against follow-up images or histological sections. In particular we employed structural (e.g. diffusion-weighted) imaging to visualize the progression of tissue injury on a voxel-wise basis after permanent or transient MCA occlusion in macaques (Chapter 2). In addition, diffusion-weighted MRI, perfusion-weighted MRI and MR angiography were employed to determine the pattern of diffusion and perfusion abnormality in relation to MR angiography-derived vessel occlusion locations after embolic stroke in rats (Chapter 3). The efficacy of the MR angiography-diffusion mismatch to depict salvageable tissue was tested against the diffusion-perfusion mismatch. Structural, diffusion, and perfusion imaging were furthermore employed to test the efficacy of different MRI-based predictive algorithms to predict tissue infarction after stroke (Chapter 4). With the addition of measures of blood-brain barrier permeability, as derived from dynamic contrast enhanced imaging, the capacity of predictive algorithms to predict secondary bleeding after embolic stroke in spontaneously hypertensive rats was also tested (Chapter 5).

The studies in this thesis reveal that voxel-wise aggregation of different MR imaging indices improves characterization and prediction of tissue outcome after ischemic stroke. This thesis specifically demonstrates that i) tracking of spatiotemporal changes of MRI-based parameters of diffusion and T_2 by means of a user-independent clustering procedure elucidates distinct temporal patterns which relate to varying degrees of

tissue injury (Chapter 2); ii) the volume and location of cerebral perfusion and diffusion abnormality have a strong correlation with the arterial occlusion site (chapter 3); iii) comorbidities, as hypertension, strongly influence the tissue volume of perfusion and diffusion abnormality with respect to vascular occlusion site (Chapter 3); iv) the MR angiography-diffusion mismatch shows increased specificity over the perfusion-diffusion mismatch in selecting individuals that may benefit from reperfusion; v) different predictive algorithms predict the extent of tissue infarction after permanent ischemic stroke equally well (Chapters 4 & 5); vi) predictive algorithms based on a generalized linear model or random forest allow for differentiation between potentially salvageable tissue and irreversibly damaged tissue (Chapter 4); vii) voxel-wise predictive algorithms enable identification of tissue at increased risk of hemorrhage (Chapter 5).

In this thesis we employed different multiparametric techniques for predicting tissue outcome after stroke. In the next part I will briefly discuss the findings of this thesis with respect to the tools applied, and additionally discuss their pitfalls and potentials.

Perfusion-diffusion mismatch

The combined use of diffusion-weighted imaging and perfusion-weighted imaging has been heralded as a sensitive and useful means to differentiate between irreversibly injured tissue and tissue at risk that is still amenable for thrombolytic treatment. (Jansen et al., 1999) However, characterization of the progression of tissue integrity beyond the acute stage of the perfusion-diffusion mismatch has hardly been investigated experimentally. In this thesis we employed the perfusion-diffusion mismatch concept to identify potentially salvageable tissue (Chapters 3 & 4). In our studies the tissue volume of diffusion abnormality was defined by a significant reduction in apparent diffusion coefficient compared to values in normal-appearing contralateral gray matter. The volume of perfusion abnormality was defined by a significant prolongation of mean transit time (MTT) of an intravenously injected bolus of contrast-agent compared to values in contralateral tissue. Previous pre-clinical studies employed cerebral blood flow values for the delineation of the abnormal perfusion volume. (Meng et al., 2004; Henninger et al., 2006; Reid et al., 2012) These studies used arterial spin labeling techniques, a MRI technique that allows for more straightforward quantification of CBF. We employed dynamic susceptibility contrast-enhanced (DSC) MRI to derive measures of perfusion. Next to a wider clinical availability of DSC MRI, making our experiments more comparable to clinical practice, our DSC MRI setup allowed for shorter acquisition times, and improved spatial and temporal resolution compared to the ASL setup available at our site. However, quantification of DSC MRI is more challenging. In DSC MRI, absolute CBF quantification is hampered by numerous factors (see for review

(Calamante et al., 2007; Knutsson et al., 2010)), therefore we calculated relative measures of perfusion. Nevertheless, in line with previous clinical studies (Rose et al., 2004; Christensen et al., 2009), the derived volumes with perfusion abnormality from these metrics corresponded well with the tissue that - without successfully reestablished perfusion - eventually infarcted at follow-up (see Chapters 4 & 5). Furthermore, tissue salvaged upon reperfusion was well correlated with the area defined by the perfusion-diffusion mismatch (Chapters 3 & 4).

Yet, areas with presumed irreversibly damaged tissue recovered upon reperfusion in some cases (Chapter 3). Particularly in patient cohorts the standardization of the perfusion-diffusion mismatch has proven to be challenging (Chapter 1). As a result a multitude of different single parameter thresholds have been applied for identification of diffusion and perfusion abnormalities which volumes have shown mostly moderate accuracy with subsequent tissue infarction volumes. (Sobesky et al., 2005 ;Bandera et al., 2006; Kane et al., 2007a; Christensen et al., 2009; Kranz and Eastwood, 2009) Especially in perfusion-weighted imaging, thresholds have been based on many different metrics to identify tissue at risk of infarction. (Kane et al., 2007a; Christensen et al., 2009) Also ratios used to derive perfusion-diffusion mismatch volumes have been disputed. In the EPITHET and DEFUSE trial 20% volume difference was used for depicting the perfusion-diffusion mismatch (Albers et al., 2006; Davis et al., 2008), whereas other studies speculated on the use of a 2:1 ratio of perfusion versus diffusion abnormality volume to select patients that may respond favorably to thrombolysis. (Donnan et al., 2009) Similar holds true in preclinical work, where the perfusion-diffusion mismatch may inform on tissue progression. Although, underlying variations in stroke type (Henninger et al., 2006), animal strain (Bardutzky et al., 2005; Coyle, 1986), or occlusion duration are more controllable, derived viability thresholds are still variable which preclude generalizability.

All in all due to the lacking consensus on the different parameters to use, generalizability is difficult to achieve, and the selection of patients based on the perfusion-diffusion mismatch may remain controversial. (Donnan et al., 2009; Hacke et al., 2009) It may thus be questioned whether this method is actually capable of specifically identifying the amount of penumbral tissue. The simple volumetric comparison of the perfusion-diffusion mismatch obscures important aspects including tissue type, collateral flow status, and vessel occlusion site, all known to influence tissue injury progression. When aiming at increasing specificity on a single parameter basis alternative MRI-based methods that inform on the metabolic rate of oxygen (OEF, $CMRO_2$)(Lee et al., 2003) or locally changing pH as a result of anaerobic metabolism (Zhou et al., 2003; Sun et al., 2007), hold more promise in specifically identifying penumbral tissue. (Ostergaard et al., 2009; Sobesky, 2012) Where PET-based experiments showed increased oxygen

extraction fraction (OEF) with a decreased oxygen metabolic rate to signify the penumbral tissue. (Fisher and Bastan, 2012) Nevertheless despite the above limitations, rats with perfusion-diffusion mismatch did respond favorably to thrombolytic treatment with observable attenuation of lesion growth (See Chapters 3 & 4). Furthermore we found the perfusion-mismatch to be sensitive in selecting those that benefitted from reperfusion (Chapter 3), but specificity was invariably low. So as a simple and intuitive additional tool, the perfusion-diffusion mismatch may be considered as a sensitive marker for subjects amenable for thrombolytic treatment (Davis et al., 2008; Lansberg et al., 2012; Kidwell, 2013), but whether it really can be used as a tool for patient selection requires improved standardization and further prospective research.

MR angiography-diffusion mismatch

The location and subsequent development of acute diffusion and perfusion lesion volumes was strongly correlated with the extent and location of large vessel occlusion within the circle of Willis as detected with magnetic resonance angiography (Chapter 3). Occlusion in the distal part of the middle cerebral artery (MCA) resulted in predominantly cortical lesions. Flow obstruction in the proximal part of the MCA along with the internal carotid artery resulted in large cortical and subcortical lesion volumes, with relatively small differences in acute diffusion and perfusion lesion volumes. This is in line with other studies that found largest infarct volumes for occlusions of the internal carotid artery and proximal part of the MCA (Derex et al., 2004; Overgaard et al., 2010), and may be used as a trade-off for selecting those where recanalization may improve outcome after thrombolytic therapy (Fiehler et al., 2005; De Silva et al., 2010)

MR-angiography-diffusion mismatch has been suggested as an alternative for the perfusion-diffusion mismatch for selecting patients that could be responsive to thrombolytic therapy, thereby obviating the need for perfusion imaging. Based on the diffusion MRI data and the MR angiography data, the physician may determine the extent of irreversibly damaged tissue relative to the involved vascular territory, from which subsequent infarct growth may be projected. We found the MR-angiography-diffusion mismatch to be highly specific in identifying potential benefit from reperfusion. However it also unnecessarily excluded animals that actually benefitted from reperfusion (Chapter 3). This corroborates previous criticism where the MR angiography-diffusion mismatch was disputed as a restricted selection tool focusing only on those patients with relatively small tissue lesions in a relatively large territory. Unnecessarily excluding patients with more moderate tissue lesions who may also benefit from reperfusion. (Schellinger and Köhrmann, 2008; Sobesky, 2012) Furthermore the degree of arterial obstruction may be incorrectly estimated with MR angiography, because of decreased sensitivity to flow

in more distal parts of the arterial tree. (Reese et al., 1999; esselmann et al., 2001; De Silva et al., 2010) In some cases a perfusion-diffusion mismatch was observed when no obvious flow obstruction could be noticed (Chapter 3 Figure 3.A). MR angiography informs on the observable macrovasculature, however stroke is at large a disease that originates because of ischemia at the microvascular level.

Indeed, volume of the acute diffusion lesion may inform on the severity of ischemia, with largest volumes noticeable for large vessel occlusions. However, subsequent infarct growth is also dependent on other factors such as collateral capabilities (Liebeskind, 2003) and tissue susceptibility (Chapter3; Coyle, 1986; Klatzo, 1987; Knight et al., 1994). These may confound the assessment of infarction risk based on the acute diffusion lesion volume and occlusion site only. Collateral flow plays an important role in the development of tissue injury after stroke. (Liebeskind, 2003) The presence of collateral flow holds a bifold potential in stroke outcome by 1) sustaining tissue at risk of infarction for prolonged period of time thereby opening up opportunities for thrombolytic therapy (Liebeskind, 2003), and 2) allowing for alternative routes of the thrombolytic agent to arrive at the blood clot causing the ischemia. (Copen et al., 2011) Direct knowledge of the collateral capabilities, as can be measured with perfusion-weighted imaging provides important information to predict tissue salvageability and to plan subsequent treatment.

Despite the abovementioned limitations of MR angiography, identification of the vascular occlusion site may support strategic treatment planning. Proximal occlusions may imply larger clot burden (Marder et al., 2006), warranting alternative thrombolysis or thrombectomy techniques to prevent infarct growth. (Fiehler et al., 2005) On the other end, the vessel occlusion site may also inform on those patients unlikely to benefit from reperfusion. Particularly those with proximal ICA/MCA occlusion, where an immediate fall of blood flow in the lenticulostriatal arteries increases vasculopathy since collateral supply is only limited, consequently increasing the risks of hemorrhagic transformation. (Vora et al., 2007; Zoppo et al., 1998) This actually coincides with the malignant profile as observed in phase II clinical trials, where large acute DWI volumes (>85mL) and substantial hypoperfusion were associated with poor outcome. (Mlynash et al., 2011) Therefore angiography complementary to diffusion-weighted imaging, perfusion-weighted imaging may contribute to improved understanding of the underlying vasculopathy. Offering better support for treatment decision-making as well as improving understanding of (experimental) treatment regimes.

Multiparametric voxel-wise predictions

In Chapters 4 and 5 supervised multiparametric analysis was employed to predict tissue outcome after stroke on a voxel-wise basis. Voxel-wise multiparametric analysis has been suggested as an alternative approach to improve tissue discrimination and interpretability. When comparing tissue infarct predictions in this thesis it can be observed that although inclusion of new MRI indices increases the model complexity, the diagnostic interpretability remains unaffected. In chapter 4 we trained and employed a random forest-based predictive model using T_2, diffusion, and perfusion parameters to calculate the risk of tissue infarction. The subsequently calculated risk maps indicated areas at risk of infarction (See Figure 4.3). The extended predictive model of Chapter 5 was similar to the one in chapter 4 but included additional spatial features as well as measures of blood brain barrier integrity. A model more complex than the one used in chapter 4, nevertheless the resulting risk maps shared similar interpretability to those in chapter 4 (See Figure 5.8).

Predictive algorithms

The risk distribution calculated from multiparametric predictive algorithms may contribute to discrimination of tissue with a variable degree of injury at follow-up (Chapters 4 & 5). Tissue responsive to reperfusion revealed lower risk values compared to irreversibly damaged tissue (Chapter 4). This is in line with previous work that showed GLM-based variations in risk distribution to correlate with irreversibly damaged tissue versus tissue amenable for thrombolytic therapy (Wu et al., 2006, 2007; Jonsdottir et al., 2009). Our studies moved forward by clarifying that this heterogeneous distribution of risk values does not apply for all predictive models. The risk maps as identified with support vector machine (SVM) and adaptive boosting (ADA) were smoother than those of a generalized linear model (GLM) or random forest (RF). Variations that may arise from differences in optimizing the decision boundary for tissue class differentiation. That may be more directly related to the training data in the GLM or RF, than the ADA or SVM that transform the input data to achieve optimal class segregation. In essence the heterogeneous predictions of the GLM or random forest arise from less confident tissue class predictions close to the class boundary of infarcted versus non-infarcted tissue. Nevertheless as a result the risk maps generated with GLM or RF discriminated potentially salvageable tissue from irreversibly damaged tissue better compared to those generated with SVM or ADA. Consequently these algorithms were selected for the hemorrhagic transformation prediction models of chapter 5 and also there the distribution of assigned risk values was found to contribute to improved discrimination between hemorrhagic tissues versus non-hemorrhagic tissues.

Nonetheless the assumed linear development of tissue injury in the generalized linear model may not always be correct given the set of input features. Both acute abnormally low and abnormally high ADC (Schwamm et al., 1998) as well as CBV (Sorensen et al., 1999b) have been linked with subsequent tissue infarction. It has therefore been speculated that other models such as a generalized additive model or random forest - models that derive their functional form from the underlying data rather than prior linear assumptions - to better differentiate between tissues.(Wu et al., 2010). Notwithstanding, the more homogeneous development of experimental stroke models compared to patients, random forest based predictions in Chapter 5, did show improved performance in differentiating tissue likely to hemorrhage over the GLM-based prediction using similar training data. Differences that may arise from marginally deviating perfusion values of both hemorrhagic and non-hemorrhagic tissue in the ischemic territory, varations that may be better differentiated by the piecewise linear random forest compared to the linear GLM (Chapter 5). This implicates that simply proposing a complex predictive algorithm for predicting the extent of tissue injury with good accuracy may omit valuable additional information that could contribute to improved interpretation. Newly proposed algorithms for tissue outcome prediction should therefore not only focus on the proper detection of the extent of tissue injury, but should also explore possibilities of detecting multiple tissue outcomes or predict multiple scenarios of tissue injury progression.

Training data

Careful definition of the underlying training data may already improve predictions without the need for complex predictive algorithms. In the study of Jonsdottir et al the need for careful selection and sampling of the data used for training was shown from GLM-based predictions. (Jonsdottir et al., 2009) This study demonstrated reduced areas under the receiver operator characteristics curve when the number of samples was not in balance. Additionally, when a substantial amount of border zone (i.e. penumbral tissue) samples were included in the training data the risk distribution shifted. Therefore in our work we carefully selected data for training by 1) strategically selecting the training data based on the specific tissue type to predict - tissue infarction prediction was determined based on a 'natural' evolution where tissue infarction was allowed to develop unimpeded (Chapter 4), whereas hemorrhage prediction was based on outcome in animals most likely to develop hemorrhage, i.e. those treated with rt-PA (Chapter 5); 2) employing parametric maps instead of 'weighted' images normalized by mean contralateral grey matter values to allow for robust cross-subject comparisons (Ding et al., 2006a; Wu et al., 2010); 3) consistently making sure that a carefully selected balance of affected versus non-affected tissue (i.e. infarcted versus non-infarcted (Chapters 4 & 5) or hemorrhagic versus non-hemorrhagic (Chapter 5)

tissue) was selected; and 4) utilizing extensive optimization procedures to optimize the balance between model complexity and prediction accuracy. As a result particularly T_2, ADC, CBF, MTT, and T_{max} were found to be important indices for prediction of infarction. Other preclinical studies found use in only ADC and CBF values for predictive modeling training (Shen and Duong, 2008; Huang et al., 2010, 2011). Although the predicted infarct volumes showed good correspondence with subsequent follow-up volumes, the tissue's progression may not be sufficiently captured by CBF and ADC. Notwithstanding the high variability of CBF due to bolus dispersion in DSC MRI, the complementary use of MTT and T_{max} informs on bolus delay. High T_{max} values seen in hyperacute stroke often coexist with hypoperfusion and may inform on poor delayed collateral supply. (Calamante et al., 2006; Willats et al., 2012)

Although careful selection of the training data may improve predictions, some difficulties remain. Penumbral areas may sustain viable for some prolonged periods of time, but eventually become part of the infarcted tissue when perfusion is not reinstated. (Heiss, 2010; Sobesky, 2012) In chapter 2 a temporally adjusted ISODATA clustering approach, revealed distinct evolutionary patterns of T_2, apparent diffusion coefficient, and fractional anisotropy with variable tissue injury. The progression of these values depended on affected tissue, time after stroke onset, and whether the state of ischemia continued unimpeded. Although, this approach may deliver useful insights in the heterogeneous development of stroke, it is impractical for stroke prediction where a 'snapshot' in time should inform on tissue progression. As time advances, ischemia-induced tissue injury progresses causing a change in tissue parameters detected with MRI. And where most of the attention has been devoted to using imaging biomarkers as a tool for estimating tissue progression or as a surrogate tool to derive stroke onset (Kidwell, 2013; Wu et al., 2011), forming a complete reflection of tissue progression may be impossible to achieve with MRI alone. Other non-imaging factors strongly influence tissue outcome. Clinical factors such as age, functional score (e.g. National Institutes of Health Scale (NIHSS) score), or comorbidities like diabetes, hypertension, to name a few, all individually affect tissue vulnerability to ischemic stroke. (Vora et al., 2011; Wu et al., 2011) Hypertension, for example, may induce increased tissue vulnerability and impose vascular malformations influencing the capability of collaterals to sustain the affected perfusion territory. (Coyle, 1986; Howells et al., 2010; Reid et al., 2012) In Chapter 3 hypertensive rats developed substantially larger lesion volumes compared to normotensive rats for similar vessel occlusion patterns. This would imply that predictions based on training data derived from normotensive subjects would underestimate tissue infarction when hypertensive subjects are considered. We therefore reason that including non-imaging markers improve tissue outcome predictions over imaging only based predictions.

Furthermore information on spatial tissue injury distributions may further improve predictions. Tissue vulnerability shows a strong regional dependency, e.g. white matter responds differently to ischemia than gray matter. (Chapter 2; Knight et al., 1994) Chapter 3 showed distributional differences of tissue lesions dependent on the location of flow disturbance. These distribution maps provide information on patterns of collateral flow and could be incorporated in the predictive model as additional supportive information. In Chapter 5 predictions improved after incorporating positional information after observing that most of the hemorrhages were found in cortical tissue. Previous work supports this by reporting improved voxel-wise prediction with the inclusion of infarct distribution maps. (Shen and Duong, 2008; Huang et al., 2010) Similarly, stroke severity assessment was improved by weighting NIHSS scoring in combination with regional volume distributions, informing on tissue most vulnerable to acute ischemia. (Cheng et al., 2011; Menezes et al., 2007) It may therefore be expected that either incorporation of additional (non-)imaging biomarkers in association with tissue vulnerability maps or the use of multiple or hierarchical prediction models - each trained with data from different time stages (hyperacute, subacute) after stroke or trained for different tissue progression scenarios (e.g. with or without reperfusion) – may hold strong potential for improved tissue outcome prediction.

Prediction of hemorrhagic transformation

Previously, supervised multiparametric prediction methods primarily focused on the calculation of infarction risk. However, with progression of time the risk of hemorrhagic transformation may be similarly critical since it can outweigh the benefits of thrombolysis. (Wardlaw et al., 2012) As a potential confounding factor for treatment success, estimating the risk of secondary bleeding is an important step in patient triage. Therefore the identification of tissue likely to develop secondary bleeding may carry great potency in assessing the risks of thrombolytic therapy.

Recent studies suggested single modalities as diffusion-weighted imaging as a promising tool for identifying patients that may develop secondary bleeding, where substantial diffusion lesion volumes (Thomalla et al., 2006; Singer et al., 2008; Mlynash et al., 2011) or substantially reduced ADC values (Selim et al., 2002) were associated with increased hemorrhage. Other studies identified severe reductions in hemodynamic parameters such as CBV as specific measures for predicting hemorrhagic transformation. (Alsop et al., 2005; Campbell et al., 2010b) The disruption of the blood-brain barrier, as measured from leakage of contrast agent out of the cerebral vasculature, was also linked with increased likelihood of hemorrhage. (Knight et al., 1998 ; Dijkhuizen et al., 2001; Hjort et al., 2008) In chapter 5 we investigated the efficacy of multiparametric prediction methods to calculate the risk of hemorrhage and subsequently compared

our results to single parameter-based thresholding. The combination of structural and hemodynamic information on the underlying tissue contributed to improved sensitivity of the prediction compared to single CBV- or K_i-based thresholding.
However, the development of hemorrhage is a process that may go beyond the severity of the initial injury. Hemorrhagic transformation is at the end of a complex, possibly reperfusion related, cascade that includes free radical formation, inflammation, and edema formation. (Pan et al., 2007) In our study 50% risk-thresholded maps overestimated the area that actually hemorrhaged, as indicated by a reduced specificity. Although predicted hemorrhagic areas were in close proximity to the actual hemorrhage, a relatively low spatial correlation of the predicted area with the eventual outcome was found. Similarly in a study of Ding *et al* the acutely identified abnormal regions were found to reside in close spatial proximity (within at most 0.75 mm) of the actual hemorrhage, but these also seemed to overestimate the hemorrhagic area, but real overlap was not reported. (Ding et al., 2006b) Previous studies also informed on a compelling correspondence of the acute imaging parameters and follow-up imaging, but did not quantifiy the correspondence (Alsop et al., 2005) or reported differing correlations dependent on the occurrence of thrombolysis. (Neumann-Haefelin et al., 2002) Notwithstanding the fact that our study was limited to the analysis of gross hemorrhage which may have underestimated the actual extent of the hemorrhage, it does imply early prediction of hemorrhagic transformation in stroke is a very challenging problem. With a natural occurrence of almost 65% and only a marginal percentage being symptomatic, the adverse role of hemorrhage transformation is not fully understood. Asymptomatic hemorrhagic transformation (e.g. hemorrhagic infarcts) has been abated as a reperfusion related epiphenomenon dependent on the degree of damage to the microvasculature, rather than the thrombolytic treatment, and consequently would carry little clinical impact. (Thomalla et al., 2007; Trouillas and Kummer, 2006; Zoppo et al., 1998) Symptomatic bleedings (e.g. parenchymal hematoma) on the other hand have a strong clinical impact with increased likelihood of functional deterioration and possible death. However it does not seem to be related to the severity of pretreatment ischemia, but more on the nature and dose of the thrombolytic treatment (Trouillas and Kummer, 2006), or older age. (Neumann-Haefelin et al., 2002; Thomalla et al., 2007) Yet, it is the possibility of acute conversion of the hemorrhagic infarction into petechial hematoma as a result of thrombolysis that raises the issue of the role of the initial ischemia in relation to the hemorrhage itself. (Trouillas and Kummer, 2006) Although in chapter 5 we specifically aimed at predicting tissue outcome based on the treatment arm of our small cohort and selected animals with a high likelihood of developing symptomatic bleedings (Henning et al., 2008), our small cohort of animals precluded the differentiation of the different types of hemorrhages. Obviously, real potency of these predictive models lies in predicting those specific scenarios that are of clinical

interest. Therefore, further studies should involve inclusion only those subjects that develop symptomatic bleedings to better assess the potential risks of thrombolytic therapy. Additionally, spatiotemporally tracing of hemorrhaging tissues could also open opportunities to further elucidate specific imaging markers or evolutionary patterns that differentiate those areas proceeding to petechial hematoma from those that remain an asymptomatic hemorrhagic infarct (Chapter 2).

Voxel-wise prediction models in (pre-) clinical research

Treatment success or failure in stroke research is often assessed by means of measurement of infarct size or behavior. (Mergenthaler and Meisel, 2012; Kidwell, 2013) Obvious attenuation of infarct size or accelerated behavioral recovery is associated with treatment success or its absence with failure. However, treatment induced changes – either positive or negative – may not be obviously reflected in these outcome parameters. Treatment-induced changes may have a more subtle origin. Changes in progression of tissue injury may be present without obvious reflection on infarct size or behavioral assessment. With about 90% of promising preclinical treatment studies not finding their way to everyday clinical practice, there is a demand for improving insights in the underlying processes that arise from experimental treatment studies. (Van der Worp et al., 2010) MRI as a non-invasive tool allows for longitudinal measurements. Voxel-wise statistical tools have been proposed as a useful and unbiased means to characterize tissue fates. The use of multiparametric MRI to delineate lesion tissue at different stages after stroke has shown improved tissue characterization over single MR parameter techniques. (Jacobs et al., 2001a, 2001b; Wu et al., 2001) These delineated areas were subsequently used for ROI-based analysis elucidating and tracking treatment induced changes after stroke in rats (Ding et al., 2004; Shen et al., 2004b) or in humans (Mitsias et al., 2002; Lu et al., 2005). Although ISODATA derived lesion volumes are unbiased and have shown good correspondence with histology (Jacobs et al., 2001a; Ding et al., 2006a), utilizing ISODATA for lesion delineation may not fully exploit the potential of this approach. Other approaches such as fuzzy c-means or regular k-means have also shown to be at least comparably effective in unbiased lesion delineation. (Carano et al., 2000) ISODATA's real utility particularly lies in its unbiased definition of the number of clusters. ROI-based analysis may introduce regional averaging potentially obscuring subtle changes in tissue development. (Nagesh et al., 1998) ISODATA, or comparable other proposed clustering techniques (see for review (Bishop, 2007)), look for groupings of voxels based on the underlying data rather than expectations of the underlying tissue, therefore circumventing the need for pre-defining the number of clusters. This allows for the identification of subtle changes in tissue which could not be observed with volumetric analysis. (Nagesh et al., 1998) The modified ISODATA in chapter 2 was employed to temporally trace stroke induced changes in diffusion and T_2 parameters. It

revealed distinct patterns of concurrent MRI changes, with different levels and timings of tissue progression, identifying not only different infarct sizes but also different levels of tissue injury progression (See chapter 2), patterns that were not observed in a previously conducted volumetric analysis. (Liu et al., 2007) The use of this type of analysis may open opportunities to identify tissue development that contributes to or opposes treatment success. In a pilot study in rats suffering from subarachnoid hemorrhage for instance we were able to identify a separately identified cluster that may hint to a possible treatment effect interferon-β by means of combining T_2, diffusion, and perfusion data. (Bouts. et al., 2010)

An increasing number of clusters may, however, challenge biological interpretability. (Shen et al., 2004b) The clusters detected are likely to increase when more MR indices, for instance informing on hemodynamic or blood brain barrier integrity, are included in the model. Good spatial correspondence with advanced coregistration tools as Elastix (Klein et al., 2010) or ANTS (Avants et al., 2011) are necessary to prevent misjudging artifacts as biologically relevant clusters in temporally tracing tissue fate. We employed additional spatial contiguity constraints, specialized coregistration techniques (Staring et al., 2007), and heuristics on initial parameter settings (i.e. distance between gray and white matter to define inter- and intracluster distance as the dispersion with the contralateral white matter region) to reduce the influence of artifacts and maintain biological interpretability. Notwithstanding these challenges this technique may hold potential as an additional tool for improved identification and definition of tissue injury development after ischemic stroke.

Chapters 4 & 5 revealed that calculated risk values corresponded with the severity of the injury. High risk values either corresponded with irreversibly damaged tissue or hemorrhage, whereas low risk values reflected no tissue injury or no hemorrhage. This quantitative index may offer an individualized grading system that obviates the need for deriving multiple viability thresholds that only apply to certain subcategories of subjects. (Thomalla et al., 2006; Reid et al., 2012) Furthermore, this index can encompass information of multiple aspects of the stroke including collateral capabilities, time from onset, and vessel occlusion site, aspects that hamper the perfusion-diffusion mismatch or angiography-diffusion mismatch (see above). Nevertheless, specific criteria for thrombolytic recruitment still need to be defined, but these criteria would be based on a more inclusive classification of the underlying tissue.

Supervised MRI-based prediction algorithms may also be used to assess the efficacy and toxicity of new therapies in experimental as well as early-phase clinical trials. In first instance, predictions of the extent of infarction based on acutely derived MRI

parameters can offer increased prognostic insights into the progression of tissue to infarction. Relatively mildly affected areas that are predicted to infarct could be amenable to subsequent treatment. In Chapter 4 the prediction models were deliberately trained for the prediction of tissue infarction without intermittent reperfusion. Subsequently, infarct predictions on animals that reperfused overestimated tissue infarction indicative of tissue injury attenuation. Differentiation of these regions that actually infarcted from those that salvaged upon reperfusion increases insights in treatment-induced changes. In an experimental treatment study we employed GLM-based predictions to determine the efficacy of liposome-encapsulated dexamethasone as a promising anti-inflammatory treatment after stroke. Although, follow-up infarct volumes were comparable among treatment groups, we detected a significant attenuation of the predicted infarct volume compared to the actual tissue infarction volume at follow-up in the liposome-encapsulated dexamethasone group, an effect not observed in the other treatment groups. (Tiebosch et al., 2012) Effectually, this concept offers opportunities of developing models that estimate the tissue progression under treatment versus non-treatment conditions. In an early-phase clinical trial, Wu et al employed GLM-based prediction models to assess the efficacy of normobaric oxygen therapy. In this study tissue infarction predictions of models trained with patients not receiving oxygen therapy were compared to predictions of models trained with patients receiving oxygen therapy. Despite the small group sizes used, this study already showed that the predicted infarct growth for the patients receiving normobaric oxygen was attenuated compared to the placebo control group. (Wu et al., 2012) This suggests that neuroradiologists, stroke physicians, or stroke researchers can be offered *a priori* estimations of the benefit and risk from a specific treatment regime without being faced with a wealth of different imaging modalities describing the current tissue status.

Conclusion

MRI-based algorithms provide a powerful means for the prediction of tissue outcome after stroke. Specifically, the results described in this thesis show that the voxel-wise aggregation of multiple MRI indices within in a single index may further enhance characterization and prediction of variable tissue injury after stroke. These tissue theme maps offer a readily interpretable alternative to analysis of a complex and heterogeneous disease mechanism embodied by a multitude of (MR) imaging-based biomarkers. Where the voxel-wise integration offers unique opportunities to differentiate and track heterogeneous tissue progression without the need for defining restricted viability thresholds. These methods furthermore offer opportunities to enhance the understanding of tissue injury progression and possible implications of new therapeutic treatment strategies in both an experimental and clinical environment. By non-invasively and prospectively informing on the implications of possible treatment strategies, fitting adjustments may result in improved patient care on an individual basis. Yet, where the studies in this thesis were limited by their retrospective nature, future (pre) clinical prospective studies including larger cohorts are needed to fully elucidate the potential of these methods. Meanwhile continuing advances in the development of new algorithms and informative MRI-based biomarkers offer a wealth of opportunities in further improving these highly promising tools.

Bibliography

Adami, A., Thijs, V., Tong, D.C., Beaulieu, C., Moseley, M.E., and Yenari, M.A. (2002). Use of diffusion weighted MRI to predict the occurrence and severity of hemorrhagic transformation in a rabbit model of embolic stroke. Brain Res. *944*, 32–39.

Albers, G.W., Thijs, V.N., Wechsler, L., Kemp, S., Schlaug, G., Skalabrin, E., Bammer, R., Kakuda, W., Lansberg, M.G., Shuaib, A., et al. (2006). Magnetic resonance imaging profiles predict clinical response to early reperfusion: The diffusion and perfusion imaging evaluation for understanding stroke evolution (DEFUSE) study. ANN Neurol. *60*, 508–517.

Allen, J.S., Damasio, H., and Grabowski, T.J. (2002). Normal neuroanatomical variation in the human brain: An MRI-volumetric study. Am J Phys Anthropol. *118*, 341–358.

Alsop, D.C., Makovetskaya, E., Kumar, S., Selim, M., and Schlaug, G. (2005). Markedly reduced apparent blood bolume on bolus contrast magnetic resonance imaging as a predictor of hemorrhage after thrombolytic therapy for acute ischemic Stroke. Stroke *36*, 746–750.

An, H., and Lin, W. (2000). Quantitative measurements of cerebral blood oxygen saturation using magnetic resonance imaging. J Cereb Blood Flow Metab. *20*, 1225–1236.

Arthur, D., and Vassilvitskii, S. (2007). K-means++: The advantages of careful seeding. Proc Ann Symp.Disc Algo (SODA '07) 1027–1035.

Astrup, J., Siesjö, B.K., and Symon, L. (1981). Thresholds in cerebral ischemia - the ischemic penumbra. Stroke *12*, 723–725.

Avants, B.B., Tustison, N.J., Song, G., Cook, P.A., Klein, A., and Gee, J.C. (2011). A reproducible evaluation of ANTs similarity metric performance in brain image registration. Neuroimage *54*, 2033–2044.

Bagher-Ebadian, H., Jafari-Khouzani, K., Mitsias, P.D., Lu, M., Soltanian-Zadeh, H., Chopp, M., and Ewing, J.R. (2011). Predicting Final Extent of Ischemic Infarction Using Artificial Neural Network Analysis of Multi-Parametric MRI in Patients with Stroke. PLoS ONE *6*, e22626.

Baird, A.E., Benfield, A., Schlaug, G., Siewert, B., Lövblad, K.O., Edelman, R.R., and Warach, S. (1997). Enlargement of human cerebral ischemic lesion volumes measured by diffusion-weighted magnetic resonance imaging. ANN Neurol. *41*, 581–589.

Ball, G.H., and Hall, D.J. (1965). ISODATA, a novel method of data analysis and pattern classification (DTIC Document).

Bandera, E., Botteri, M., Minelli, C., Sutton, A., Abrams, K.R., and Latronico, N. (2006). Cerebral Blood Flow Threshold of Ischemic Penumbra and Infarct Core in Acute Ischemic Stroke A Systematic Review. Stroke *37*, 1334–1339.

Bang, O.Y., Buck, B.H., Saver, J.L., Alger, J.R., Yoon, S.R., Starkman, S., Ovbiagele, B., Kim, D., Ali, L.K., Sanossian, N., et al. (2007). Prediction of hemorrhagic transformation after recanalization therapy using T2*-permeability magnetic resonance imaging. ANN Neurol. *62*, 170–176.

Bang, O.Y., Saver, J.L., Buck, B.H., Alger, J.R., Starkman, S., Ovbiagele, B., Kim, D., Jahan, R., Duckwiler, G.R., Yoon, S.R., et al. (2008). Impact of collateral flow on tissue fate in acute ischaemic stroke. J Neurol, Neurosur Ps. *79*, 625–629.

Bardutzky, J., Shen, Q., Henninger, N., Bouley, J., Duong, T.Q., and Fisher, M. (2005). Differences in Ischemic Lesion Evolution in Different Rat Strains Using Diffusion and Perfusion Imaging. Stroke *36*, 2000–2005.

Basser, P.J., Mattiello, J., and LeBihan, D. (1994). Estimation of the effective self-diffusion tensor from the NMR spin echo. J Magn Reson B. *103*, 247–254.

Bederson, J.B., Pitts, L.H., Tsuji, M., Nishimura, M.C., Davis, R.L., and Bartkowski, H. (1986). Rat middle cerebral artery occlusion: evaluation of the model and development of a neurologic examination. Stroke *17*, 472–476.

Besselmann, M., Liu, M., Diedenhofen, M., Franke, C., and Hoehn, M. (2001). MR angiographic investigation of transient focal cerebral ischemia in rat. NMR in Biomed. *14*, 289–296.

Bhagat, Y.A., Emery, D.J., Shuaib, A., Sher, F., Rizvi, N.H., Akhtar, N., Clare, T.L., Leatherdale, T., and Beaulieu, C. (2006). The relationship between diffusion anisotropy and time of onset after stroke. J Cereb Blood Flow Metab. *26*, 1442–1450.

Bihan, D.L., Turner, R., Douek, P., and Patronas, N. (1992). Diffusion MR imaging: clinical applications. AJR *159*, 591–599.

Bishop, C.M. (2007). Pattern Recognition and Machine Learning (Springer).

Bouts, M.J.R.J., Tiebosch, I.A.C.W., Zwartbol, R., Wu, O., and Dijkhuizen, R.M. (2010). Effects of Treatment on Brain Tissue Classification with Serial MRI-Based ISODATA Cluster Analysis in an Experimental Subarachnoid Hemorrhage Model. Proc. Intl. Soc. Mag. Reson. Med, (Stockholm, Sweden), p. 3132.

Breiman, L. (2001). Random forests. Mach Learn. *45*, 5–32.

Cai, H., Yao, H., Ibayashi, S., Uchimura, H., and Fujishima, M. (1998). Photothrombotic middle cerebral artery occlusion in spontaneously hypertensive rats: influence of substrain, gender, and distal middle cerebral artery patterns on infarct size. Stroke *29*, 1982–1987.

Cai, W., Chen, S., and Zhang, D. (2007). Fast and robust fuzzy c-means clustering algorithms incorporating local information for image segmentation. Pattern Recognition *40*, 825–838.

Calamante, F., Lythgoe, M.F., Pell, G.S., Thomas, D.L., King, M.D., Busza, A.L., Sotak, C.H., Williams, S.R., Ordidge, R.J., and Gadian, D.G. (1999). Early changes in water diffusion, perfusion, T1, and T2 during focal cerebral ischemia in the rat studied at 8.5 T. Magn Reson Med. *41*, 479–485.

Calamante, F., Willats, L., Gadian, D.G., and Connelly, A. (2006). Bolus delay and dispersion in perfusion MRI: Implications for tissue predictor models in stroke. Magn Reson Med. *55*, 1180–1185.

Calamante, F., Vonken, E.-J.P.A., and Van Osch, M.J.P. (2007). Contrast agent concentration measurements affecting quantification of bolus-tracking perfusion MRI. Magn Reson Med. *58*, 544–553.

Campbell, B.C.V., Christensen, S., Foster, S.J., Desmond, P.M., Parsons, M.W., Butcher, K.S., Barber, P.A., Levi, C.R., Bladin, C.F., Donnan, G.A., et al. (2010a). Visual assessment of perfusion-diffusion mismatch is inadequate to select patients for thrombolysis. Cerebrovasc Dis. *29*, 592–596.

Campbell, B.C.V., Christensen, S., Butcher, K.S., Gordon, I., Parsons, M.W., Desmond, P.M., Barber, P.A., Levi, C.R., Bladin, C.F., Silva, D.A.D., et al. (2010b). Regional very low cerebral blood volume predicts hemorrhagic transformation better than diffusion-weighted imaging volume and thresholded apparent diffusion coefficient in acute ischemic stroke. Stroke *41*, 82–88.

Campbell, B.C.V., Costello, C., Christensen, S., Ebinger, M., Parsons, M.W., Desmond, P.M., Barber, P.A., Butcher, K.S., Levi, C.R., De Silva, D.A., et al. (2011). Fluid-attenuated inversion recovery hyperintensity in acute ischemic stroke may not predict hemorrhagic transformation. Cerebrovasc Dis. *32*, 401–405.

Campbell, B.C.V., Purushotham, A., Christensen, S., Desmond, P.M., Nagakane, Y., Parsons, M.W., Lansberg, M.G., Mlynash, M., Straka, M., De Silva, D.A., et al. (2012). The infarct core is well represented by the acute diffusion lesion: Sustained reversal is infrequent. J Cereb Blood Flow Metab. *32*, 50–56.

Cao, Y., Brown, S.L., Knight, R.A., Fenstermacher, J.D., and Ewing, J.R. (2005). Effect of intravascular-to-extravascular water exchange on the determination of blood-to-tissue transfer constant by magnetic resonance imaging. Magn Reson Med *53*, 282–293.

Carano, R.A.D., Li, F., Irie, K., Helmer, K.G., Silva, M.D., Fisher, M., and Sotak, C.H. (2000). Multispectral analysis of the temporal evolution of cerebral ischemia in the rat brain. Journal of Magnetic Resonance Imaging *12*, 842–858.

Chan, P.H. (2001). Reactive oxygen radicals in signaling and damage in the ischemic brain. J Cereb Blood Flow Metab. *21*, 2–14.

Cheng, B., Golsari, A., Fiehler, J., Rosenkranz, M., Gerloff, C., and Thomalla, G. (2011). Dynamics of regional distribution of ischemic lesions in middle cerebral artery trunk occlusion relates to collateral circulation. J Cereb Blood Flow Metab. *31*, 36–40.

Christensen, S., Mouridsen, K., Wu, O., Hjort, N., Karstoft, H., Thomalla, G., Rother, J., Fiehler, J., Kucinski, T., and Ostergaard, L. (2009). Comparison of 10 perfusion MRI parameters in 97 sub-6-hour stroke patients using voxel-based receiver operating characteristics analysis. Stroke *40*, 2055–2061.

Cohen, J. (1960). A coefficient of agreement for nominal scales. Educ and Psycholog M. *20*, 37–46.

Collins, D.L., Neelin, P., Peters, T.M., and Evans, A.C. (1994). Automatic 3D intersubject registration of MR volumetric data in standardized Talairach space. J Comput Assist Tomogr. *18*, 192–205.

Copen, W.A., Rezai Gharai, L., Barak, E.R., Schwamm, L.H., Wu, O., Kamalian, S., Gonzalez, R.G., and Schaefer, P.W. (2009). Existence of the diffusion-perfusion mismatch within 24 hours after onset of acute stroke: dependence on proximal arterial occlusion. Radiology *250*, 878–886.

Copen, W.A., Schaefer, P.W., and Wu, O. (2011). MR perfusion imaging in acute ischemic stroke. Neuroimaging Clin N Am *21*, 259–283.

Coyle, P. (1986). Different susceptibilities to cerebral infarction in spontaneously hypertensive (SHR) and normotensive Sprague-Dawley rats. Stroke *17*, 520–525.

Coyle, P. (1987). Dorsal cerebral collaterals of stroke-prone spontaneously hypertensive rats (SHRSP) and Wistar Kyoto rats (WKY). Anat. Rec. *218*, 40–44.

Coyle, P., and Heistad, D.D. (1986). Blood flow through cerebral collateral vessels in hypertensive and normotensive rats. Hypertension *8*, II67.

Coyle, P., Odenheimer, D.J., and Sing, C.F. (1984). Cerebral infarction after middle cerebral artery occlusion in progenies of spontaneously stroke-prone and normal rats. Stroke *15*, 711–716.

De Crespigny, A.J., D'Arceuil, H.E., Maynard, K.I., He, J., McAuliffe, D., Norbash, A., Sehgal, P.K., Hamberg, L., Hunter, G., Budzik, R.F., et al. (2005). Acute studies of a new primate model of reversible middle cerebral artery occlusion. J Stroke Cerebrovasc Dis. *14*, 80–87.

D'Arceuil, H.E., Duggan, M., He, J., Pryor, J., and De Crespigny, A. (2006). Middle cerebral artery occlusion in Macaca fascicularis: acute and chronic stroke evolution. Journal Med Primatol *35*, 78–86.

Dávalos, A., Blanco, M., Pedraza, S., Leira, R., Castellanos, M., Pumar, J.M., Silva, Y., Serena, J., and Castillo, J. (2004). The clinical-DWI mismatch: a new diagnostic approach to the brain tissue at risk of infarction. Neurology *62*, 2187–2192.

Davis, J., and Goadrich, M. (2006). The relationship between Precision-Recall and ROC curves. ICML 2006 - Proc Int Conf Mach Learn, pp. 233–240.

Davis, S.M., Donnan, G.A., Parsons, M.W., Levi, C., Butcher, K.S., Peeters, A., Barber, P.A., Bladin, C., De Silva, D.A., Byrnes, G., et al. (2008). Effects of alteplase beyond 3 h after stroke in the Echoplanar Imaging Thrombolytic Evaluation Trial (EPITHET): a placebo-controlled randomised trial. Lancet Neurol. *7*, 299–309.

Deguchi, I., Takeda, H., Furuya, D., Hattori, K., Dembo, T., Nagoya, H., Kato, Y., Fukuoka, T., Maruyama, H., and Tanahashi, N. (2011). Significance of clinical-diffusion mismatch in hyperacute cerebral infarction. J Stroke Cerebrovasc Dis *20*, 62–67.

Deguchi, I., Dembo, T., Fukuoka, T., Nagoya, H., Maruyama, H., Kato, Y., Oe, Y., Horiuchi, Y., Takeda, H., and Tanahashi, N. (2012). Usefulness of MRA-DWI mismatch in neuroendovascular therapy for acute cerebral infarction. Eur J Neurol *19*, 114–120.

Derex, L., Hermier, M., Adeleine, P., Pialat, J.B., Wiart, M., Berthezène, Y., Froment, J.C., Trouillas, P., and Nighoghossian, N. (2004). Influence of the site of arterial occlusion on multiple baseline hemodynamic MRI parameters and post-thrombolytic recanalization in acute stroke. Neuroradiology *46*, 883–887.

Dice, L.R. (1945). Measures of the Amount of Ecologic Association Between Species. Ecology *26*, 297–302.

Dijkhuizen, R.M., and Nicolay, K. (2003). Magnetic resonance imaging in experimental models of brain disorders. J. Cereb. Blood Flow Metab. *23*, 1383–1402.

Dijkhuizen, R.M., Berkelbach van der Sprenkel, J.W., Tulleken, K.A., and Nicolay, K. (1997). Regional assessment of tissue oxygenation and the temporal evolution of hemodynamic parameters and water diffusion during acute focal ischemia in rat brain. Brain Res. *750*, 161–170.

Dijkhuizen, R.M., Knollema, S., Worp, H.B. van der, Horst, G.J.T., Wildt, D.J.D., Sprenkel, J.W.B. van der, Tulleken, K.A.F., and Nicolay, K. (1998a). Dynamics of cerebral tissue injury and perfusion after temporary hypoxia-ischemia in the rat evidence for region-specific sensitivity and delayed damage. Stroke *29*, 695–704.

Dijkhuizen, R.M., Knollema, S., Van der Worp, H.B., Ter Horst, G.J., De Wildt, D.J., Berkelbach van der Sprenkel JW, Tulleken, K.A., and Nicolay, K. (1998b). Dynamics of cerebral tissue injury and perfusion after temporary hypoxia-ischemia in the rat: evidence for region-specific sensitivity and delayed damage. Stroke *29*, 695–704.

Dijkhuizen, R.M., Asahi, M., Wu, O., Rosen, B.R., and Lo, E.H. (2001). Delayed rt-PA treatment in a rat embolic stroke model: diagnosis and prognosis of ischemic injury and hemorrhagic transformation with magnetic resonance imaging. J. Cereb. Blood Flow Metab. *21*, 964–971.

Ding, G., Jiang, Q., Zhang, L., Zhang, Z., Knight, R.A., Soltanian-Zadeh, H., Lu, M., Ewing, J.R., Li, Q., Whitton, P.A., et al. (2004). Multiparametric ISODATA analysis of embolic stroke and rt-PA intervention in rat. J Neurol Sci. *223*, 135–143.

Ding, G., Nagesh, V., Jiang, Q., Zhang, L., Zhang, Z.G., Li, L., Knight, R.A., Li, Q., Ewing, J.R., and Chopp, M. (2005). Early prediction of gross hemorrhagic transformation by noncontrast agent mri cluster analysis after embolic stroke in rat. Stroke *36*, 1247–1252.

Ding, G., Jiang, Q., Li, L., Zhang, L., Zhang, Z.G., Soltanian-Zadeh, H., Li, Q., Whitton, P.A., Ewing, J.R., and Chopp, M. (2006a). Characterization of cerebral tissue by MRI map ISODATA in embolic stroke in rat. Brain Res. *1084*, 202–209.

Ding, G., Jiang, Q., Li, L., Zhang, L., Gang Zhang, Z., Ledbetter, K.A., Ewing, J.R., Li, Q., and Chopp, M. (2006b). Detection of BBB disruption and hemorrhage by Gd-DTPA enhanced MRI after embolic stroke in rat. Brain Res. *1114*, 195–203.

Ding, G., Jiang, Q., Li, L., Zhang, L., Zhang, Z.G., Ledbetter, K.A., Panda, S., Davarani, S.P.N., Athiraman, H., Li, Q., et al. (2008). Magnetic resonance imaging investigation of axonal remodeling and angiogenesis after embolic stroke in sildenafil-treated rats. J Cereb Blood Flow Metab. *28*, 1440–1448.

Dirnagl, U., Iadecola, C., and Moskowitz, M.A. (1999). Pathobiology of ischaemic stroke: an integrated view. Trends Neurosci. *22*, 391–397.

Dirnagl, U., Simon, R.P., and Hallenbeck, J.M. (2003). Ischemic tolerance and endogenous neuroprotection. Trends Neurosci. *26*, 248–254.

Donnan, G.A., Baron, J.-C., Ma, H., and Davis, S.M. (2009). Penumbral selection of patients for trials of acute stroke therapy. Lancet Neurol. *8*, 261–269.

Van Dorsten, F. a., Olàh, L., Schwindt, W., Grüne, M., Uhlenküken, U., Pillekamp, F., Hossmann, K.-A., and Hoehn, M. (2002). Dynamic changes of ADC, perfusion, and NMR relaxation parameters in transient focal ischemia of rat brain. Magn Reson Med. *47*, 97–104.

Ebinger, M., Iwanaga, T., Prosser, J.F., Silva, D.A.D., Christensen, S., Collins, M., Parsons, M.W., Levi, C.R., Bladin, C.F., Barber, P.A., et al. (2009). Clinical–diffusion mismatch and benefit from thrombolysis 3 to 6 hours after acute stroke. Stroke *40*, 2572–2574.

Efron, B. (1987). The Jackknife, the bootstrap, and other resampling plans (Society for Industrial Mathematics).

Einstein, A. (1905). On the movement of small particles suspended in stationary liquids required by the molecular-kinetic theory of heat. Ânnalen Der Physik *17*, 549–560.

Ewing, J.R., Knight, R.A., Nagaraja, T.N., Yee, J.S., Nagesh, V., Whitton, P.A., Li, L., and Fenstermacher, J.D. (2003). Patlak plots of Gd-DTPA MRI data yield blood–brain transfer constants concordant with those of 14C-sucrose in areas of blood–brain opening. Magn Reson Med. *50*, 283–292.

Fiebach, J.B., Al-Rawi, Y., Wintermark, M., Furlan, A.J., Rowley, H.A., Lindstén, A., Smyej, J., Eng, P., Warach, S., and Pedraza, S. (2012). Vascular occlusion enables selecting acute ischemic stroke patients for treatment with desmoteplase. Stroke *43*, 1561–1566.

Fiehler, J., Foth, M., Kucinski, T., Knab, R., Von Bezold, M., Weiller, C., Zeumer, H., and Rother, J. (2002). Severe ADC decreases do not predict irreversible tissue damage in humans. Stroke *33*, 79–86.

Fiehler, J., Knudsen, K., Kucinski, T., Kidwell, C.S., Alger, J.R., Thomalla, G., Eckert, B., Wittkugel, O., Weiller, C., Zeumer, H., et al. (2004). Predictors of apparent diffusion coefficient normalization in stroke patients. Stroke *35*, 514–519.

Fiehler, J., Knudsen, K., Thomalla, G., Goebell, E., Rosenkranz, M., Weiller, C., Röther, J., Zeumer, H., and Kucinski, T. (2005). Vascular occlusion sites determine differences in lesion growth from early apparent diffusion coefficient lesion to final infarct. Am J Neuroradiol. *26*, 1056 –1061.

Fiorelli, M., Bastianello, S., Kummer, R. von, Zoppo, G.J. del, Larrue, V., Lesaffre, E., Ringleb, A.P., Lorenzano, S., Manelfe, C., and Bozzao, L. (1999). Hemorrhagic transformation within 36 hours of a cerebral infarct relationships with early clinical deterioration and 3-month outcome in the european cooperative acute stroke study i (ecass i) cohort. Stroke *30*, 2280–2284.

Fisher, M., and Bastan, B. (2012). Identifying and utilizing the ischemic penumbra. Neurology *79*, S79–85.

Fisher, M., Feuerstein, G., Howells, D.W., Hurn, P.D., Kent, T.A., Savitz, S.I., and Lo, E.H. (2009). Update of the stroke therapy academic industry roundtable preclinical recommendations. Stroke *40*, 2244–2250.

Freund, Y., and Schapire, R. (1995). A desicion-theoretic generalization of on-line learning and an application to boosting. In Computational Learning Theory, P. Vitányi, ed. (Springer Berlin / Heidelberg), pp. 23–37.

Freund, Y., and Schapire, R.E. (1997). A decision-theoretic generalization of on-line learning and an application to boosting. Journal Comput Syst Sci. *55*, 119–139.

Friedman, J. (2000). Additive logistic regression: a statistical view of boosting (With discussion and a rejoinder by the authors). ANN Statist. *28*, 337–407.

Furlan, M., Marchal, G., Viader, F., Derlon, J.M., and Baron, J.C. (1996). Spontaneous neurological recovery after stroke and the fate of the ischemic penumbra. ANN Neurol. *40*, 216–226.

Girn, H.R.S., Ahilathirunayagam, S., Mavor, A.I.D., and Homer-Vanniasinkam, S. (2007). Reperfusion syndrome: cellular mechanisms of microvascular dysfunction and potential therapeutic strategies. Vasc Endovasc Surg. *41*, 277–293.

Gorter, J.W. (1999). Major bleeding during anticoagulation after cerebral ischemia Patterns and risk factors. Neurology *53*, 1319–1319.

Gottrup, C., Thomsen, K., Locht, P., Wu, O., Sorensen, A.G., Koroshetz, W.J., and Østergaard, L. (2005). Applying instance-based techniques to prediction of final outcome in acute stroke. Artif Intell Med *33*, 223–236.

Goyal, M., Menon, B.K., and Derdeyn, C.P. (2013). Perfusion Imaging in Acute Ischemic Stroke: Let Us Improve the Science before Changing Clinical Practice. Radiology *266*, 16–21.

Green, H.A.L., Peña, A., Price, C.J., Warburton, E.A., Pickard, J.D., Carpenter, T.A., and Gillard, J.H. (2002). Increased anisotropy in acute stroke a possible explanation. Stroke *33*, 1517–1521.

Gregoire, N. (1989). The blood-brain barrier. J Neuroradiol *16*, 238–250.

Guadagno, J.V., Warburton, E.A., Aigbirhio, F.I., Smielewski, P., Fryer, T.D., Harding, S., Price, C.J., Gillard, J.H., Carpenter, T.A., and Baron, J.-C. (2004). Does the acute diffusion-weighted imaging lesion represent penumbra as well as core? a combined quantitative pet/mri voxel-based study. J Cereb Blood Flow Metab. *24*, 1249–1254.

Haacke, E.M., Brown, R.W., Thompson, M.R., and Venkatesan, R. (1999). Magnetic resonance imaging: physical principles and sequence design (Wiley-Liss).

Hacke, W., Brott, T., Caplan, L., Meier, D., Fieschi, C., Von Kummer, R., Donnan, G., Heiss, W.D., Wahlgren, N.G., Spranger, M., et al. (1999). Thrombolysis in acute ischemic stroke: controlled trials and clinical experience. Neurology *53*, S3–14.

Hacke, W., Kaste, M., Bluhmki, E., Brozman, M., Dávalos, A., Guidetti, D., Larrue, V., Lees, K.R., Medeghri, Z., Machnig, T., et al. (2008). Thrombolysis with alteplase 3 to 4.5 hours after acute ischemic stroke. N. Engl. J. Med. *359*, 1317–1329.

Hacke, W., Furlan, A.J., Al-Rawi, Y., Davalos, A., Fiebach, J.B., Gruber, F., Kaste, M., Lipka, L.J., Pedraza, S., Ringleb, P.A., et al. (2009). Intravenous desmoteplase in patients with acute ischaemic stroke selected by MRI perfusion-diffusion weighted imaging or perfusion CT (DIAS-2): a prospective, randomised, double-blind, placebo-controlled study. Lancet Neurol *8*, 141–150.

Hamberg, L.M., Boccalini, P., Stranjalis, G., Hunter, G.J., Huang, Z., Halpern, E., Weisskoff, R.M., Moskowitz, M.A., and Rosen, B.R. (1996). Continuous assessment of relative cerebral blood volume in transient ischemia using steady state susceptibility-contrast MRI. Magn Reson Med. *35*, 168–173.

Harrer, J.U. (2010). Clinical applicability and the perfusion-diffusion mismatch theory: not yet a perfect match. Neurology *75*, 1034–1035.

Hastie, T., Tibshirani, R., and Friedman, J. (2009). The elements of statistical learning: data mining, inference, and prediction, second edition (Springer).

Heiss, W.-D. (2010). The concept of the penumbra: can it be translated to stroke management? Int J Stroke *5*, 290–295.

Heiss, W.-D., and Rosner, G. (1983). Functional recovery of cortical neurons as related to degree and duration of ischemia. ANN Neurol. *14*, 294–301.

Hendrikse, J., Grond, J. van der, Lu, H., Zijl, P.C.M. van, and Golay, X. (2004). Flow territory mapping of the cerebral arteries with regional perfusion MRI. Stroke *35*, 882–887.

Henning, E.C., Latour, L.L., Hallenbeck, J.M., and Warach, S. (2008). Reperfusion-associated hemorrhagic transformation in SHR rats: evidence of symptomatic parenchymal hematoma. Stroke *39*, 3405–3410.

Henninger, N., Sicard, K.M., Schmidt, K.F., Bardutzky, J., and Fisher, M. (2006). Comparison of ischemic lesion evolution in embolic versus mechanical middle cerebral artery occlusion in sprague dawley rats using diffusion and perfusion imaging. Stroke *37*, 1283–1287.

Henninger N, Sicard KM, Fisher M. (2007). Spectacular shrinking deficit: insights from multimodal magnetic resonance imaging after embolic middle cerebral artery occlusion in Sprague-Dawley rats. J Cereb Blood Flow Metab. *27*, 1756–1763.

Hjort, N., Christensen, S., Sølling, C., Ashkanian, M., Wu, O., Røhl, L., Gyldensted, C., Andersen, G., and Østergaard, L. (2005a). Ischemic injury detected by diffusion imaging 11 minutes after stroke. Ann. Neurol. *58*, 462–465.

Hjort, N., Butcher, K., Davis, S.M., Kidwell, C.S., Koroshetz, W.J., Röther, J., Schellinger, P.D., Warach, S., and Østergaard, L. (2005b). Magnetic resonance imaging criteria for thrombolysis in acute cerebral infarct. Stroke *36*, 388–397.

Hjort, N., Wu, O., Ashkanian, M., Sølling, C., Mouridsen, K., Christensen, S., Gyldensted, C., Andersen, G., and Østergaard, L. (2008). MRI detection of early blood-brain barrier disruption parenchymal enhancement predicts focal hemorrhagic transformation after thrombolysis. Stroke *39*, 1025–1028.

Hoffmann, A., Bredno, J., Wendland, M.F., Derugin, N., Hom, J., Schuster, T., Zimmer, C., Su, H., Ohara, P.T., Young, W.L., et al. (2012). MRI blood–brain barrier permeability measurements to predict hemorrhagic transformation in a rat model of ischemic stroke. Transl. Stroke Res. *3*, 508–516.

Horowitz, S.H., Zito, J.L., Donnarumma, R., Patel, M., and Alvir, J. (1991). Computed tomographic-angiographic findings within the first five hours of cerebral infarction. Stroke *22*, 1245–1253.

Hossmann, K.A. (1996). Periinfarct depolarizations. Cerebrovasc Brain Metab Rev *8*, 195–208.

Howells, D.W., Porritt, M.J., Rewell, S.S.J., O'Collins, V., Sena, E.S., Van der Worp, H.B., Traystman, R.J., and Macleod, M.R. (2010). Different strokes for different folks: the rich diversity of animal models of focal cerebral ischemia. J Cereb Blood Flow Metab. *30*, 1412–1431.

Huang, S., Shen, Q., and Duong, T.Q. (2010). Artificial neural network prediction of ischemic tissue fate in acute stroke imaging. J Cereb Blood Flow Metab. *30*, 1661–1670.

Huang, S., Shen, Q., and Duong, T.Q. (2011). Quantitative prediction of acute ischemic tissue fate using support vector machine. Brain Res. *1405*, 77–84.

Hui, E.S., Du, F., Huang, S., Shen, Q., and Duong, T.Q. (2012). Spatiotemporal dynamics of diffusional kurtosis, mean diffusivity and perfusion changes in experimental stroke. Brain Res. *1451*, 100–109.

Intengan, H.D., and Schiffrin, E.L. (2000). Structure and mechanical properties of resistance arteries in hypertension role of adhesion molecules and extracellular matrix determinants. Hypertension *36*, 312–318.

Investigators, T.I.S. (2006). Hemorrhage in the interventional management of stroke study. Stroke *37*, 847–851.

Ito, U., Ohno, K., Nakamura, R., Suganuma, F., and Inaba, Y. (1979). Brain edema during ischemia and after restoration of blood flow. Measurement of water, sodium, potassium content and plasma protein permeability. Stroke *10*, 542–547.

Jacobs, M.A., Knight, R.A., Soltanian-Zadeh, H., Zheng, Z.G., Goussev, A.V., Peck, D.J., Windham, J.P., and Chopp, M. (2000). Unsupervised segmentation of multiparameter MRI in experimental cerebral ischemia with comparison to T2, diffusion, and ADC MRI parameters and histopathological validation. J Magn Reson Imaging *11*, 425–437.

Jacobs, M.A., Zhang, Z.G., Knight, R.A., Soltanian-Zadeh, H., Goussev, A.V., Peck, D.J., and Chopp, M. (2001a). A model for multiparametric mri tissue characterization in experimental cerebral ischemia with histological validation in rat: part 1. Stroke *32*, 943–949.

Jacobs, M.A., Mitsias, P., Soltanian-Zadeh, H., Santhakumar, S., Ghanei, A., Hammond, R., Peck, D.J., Chopp, M., and Patel, S. (2001b). Multiparametric MRI tissue characterization in clinical stroke with correlation to clinical outcome: part 2. Stroke *32*, 950–957.

Janjua, N. (2012). Use of neuroimaging to guide the treatment of patients beyond the 8-hour time window. Neurology *79*, S95–S99.

Jansen, O., Schellinger, P., Fiebach, J., Hacke, W., and Sartor, K. (1999). Early recanalisation in acute ischaemic stroke saves tissue at risk defined by MRI. Lancet *353*, 2036–2037.

Jiang, Q., Ewing, J.R., Ding, G.L., Zhang, L., Zhang, Z.G., Li, L., Whitton, P., Lu, M., Hu, J., Li, Q.J., et al. (2005). Quantitative evaluation of BBB permeability after embolic stroke in rat using MRI. J Cereb Blood Flow Metab. *25*, 583–592.

Jiang, Q., Zhang, Z.G., Ding, G.L., Silver, B., Zhang, L., Meng, H., Lu, M., Pourabdillah-Nejed-D., S., Wang, L., Savant-Bhonsale, S., et al. (2006). MRI detects white matter reorganization after neural progenitor cell treatment of stroke. NeuroImage *32*, 1080–1089.

Jiang, Q., Ewing, J.R., and Chopp, M. (2012). MRI of blood–brain barrier permeability in cerebral ischemia. Transl Stroke Res. *3*, 56–64.

Jones, T.H., Morawetz, R.B., Crowell, R.M., Marcoux, F.W., FitzGibbon, S.J., DeGirolami, U., and Ojemann, R.G. (1981). Thresholds of focal cerebral ischemia in awake monkeys. J Neurosurg. *54*, 773–782.

Jonsdottir, K.Y., Østergaard, L., and Mouridsen, K. (2009). Predicting tissue outcome from acute stroke magnetic resonance imaging: improving model performance by optimal sampling of training data. Stroke *40*, 3006–3011.

Kane, I., Carpenter, T., Chappell, F., Rivers, C., Armitage, P., Sandercock, P., and Wardlaw, J. (2007a). Comparison of 10 different magnetic resonance perfusion imaging processing methods in acute ischemic stroke effect on lesion size, proportion of patients with diffusion/perfusion mismatch, clinical scores, and radiologic outcomes. Stroke *38*, 3158–3164.

Kane, I., Sandercock, P., and Wardlaw, J. (2007b). Magnetic resonance perfusion diffusion mismatch and thrombolysis in acute ischaemic stroke: a systematic review of the evidence to date. J Neurol Neurosurg Psych. *78*, 485–491.

Karatzoglou, A., Smola, A., Hornik, K., and Zeileis, A. (2004). kernlab - An S4 Package for Kernel Methods in R. J Stat Softw *11*, 1–20.

Kastrup, A., Gröschel, K., Ringer, T.M., Redecker, C., Cordesmeyer, R., Witte, O.W., and Terborg, C. (2008). Early disruption of the blood-brain barrier after thrombolytic therapy predicts hemorrhage in patients with acute stroke. Stroke *39*, 2385–2387.

Kato, H., Izumiyama, M., Izumiyama, K., Takahashi, A., and Itoyama, Y. (2002). Silent cerebral microbleeds on t2*-weighted mri correlation with stroke subtype, stroke recurrence, and leukoaraiosis. Stroke *33*, 1536–1540.

Kaur, J., Tuor, U.I., Zhao, Z., Petersen, J., Jin, A.Y., and Barber, P.A. (2009). Quantified T1 as an adjunct to apparent diffusion coefficient for early infarct detection: a high-field magnetic resonance study in a rat stroke model. Int J Stroke *4*, 159–168.

Kidwell, C.S. (2013). MRI biomarkers in acute ischemic stroke: a conceptual framework and historical analysis. Stroke *44*, 570–578.

Kidwell, C.S., Saver, J.L., Mattiello, J., Starkman, S., Vinuela, F., Duckwiler, G., Gobin, Y.P., Jahan, R., Vespa, P., Kalafut, M., et al. (2000). Thrombolytic reversal of acute human cerebral ischemic injury shown by diffusion/perfusion magnetic resonance imaging. ANN Neurol. *47*, 462–469.

Kidwell, C.S., Saver, J.L., Starkman, S., Duckwiler, G., Jahan, R., Vespa, P., Pablo Villablanca, J., Liebeskind, D.S., Gobin, Y.P., Vinuela, F., et al. (2002). Late secondary ischemic injury in patients receiving intraarterial thrombolysis. ANN Neurol. *52*, 698–703.

Kidwell, C.S., Alger, J.R., and Saver, J.L. (2003). Beyond mismatch: evolving paradigms in imaging the ischemic penumbra with multimodal magnetic resonance imaging. Stroke *34*, 2729–2735.

Kim, E.Y., Na, D.G., Kim, S.S., Lee, K.H., Ryoo, J.W., and Kim, H.K. (2005). Prediction of hemorrhagic transformation in acute ischemic stroke: role of diffusion-weighted imaging and early parenchymal enhancement. Am J Neuroradiol. *26*, 1050–1055.

Kim, S.J., Seok, J.M., Bang, O.Y., Kim, G.-M., Kim, K.H., Jeon, P., Chung, C.-S., Lee, K.H., Alger, J.R., and Liebeskind, D.S. (2009). MR mismatch profiles in patients with intracranial atherosclerotic stroke: A comprehensive approach comparing stroke subtypes. J Cereb Blood Flow Metab. *29*, 1138–1145.

Kirino, T., Tamura, A., and Sano, K. (1984). Delayed neuronal death in the rat hippocampus following transient forebrain ischemia. Acta Neuropathol *64*, 139–147.

Klatzo, I. (1987). Pathophysiological aspects of brain edema. Acta Neuropathol *72*, 236–239.

Klein, S., Staring, M., Murphy, K., Viergever, M.A., and Pluim, J.P. (2010). Elastix: a toolbox for intensity-based medical image registration. IEEE Trans Med Imaging *29*, 196–205.

Knight, R.A., Dereski, M.O., Helpern, J.A., Ordidge, R.J., Chopp, M., and Rosenberg, G.A. (1994). Magnetic resonance imaging assessment of evolving focal cerebral ischemia: Comparison with histopathology in rats. Stroke *25*, 1252–1262.

Knight, R.A., Barker, P.B., Fagan, S.C., Li, Y., Jacobs, M.A., and Welch, K.M.A. (1998). Prediction of impending hemorrhagic transformation in ischemic stroke using magnetic resonance imaging in rats. Stroke *29*, 144–151.

Knutsson, L., Ståhlberg, F., and Wirestam, R. (2010). Absolute quantification of perfusion using dynamic susceptibility contrast MRI: pitfalls and possibilities. Magn Reson Mat Phys, Biol Med. *23*, 1–21.

Kranz, P.G., and Eastwood, J.D. (2009). Does diffusion-weighted imaging represent the ischemic core? an evidence-based systematic review. Am J Neuroradiol. *30*, 1206–1212.

Kwa, V.I.H., Franke, C.L., Verbeeten, B., and Stam, J. (1998). Silent intracerebral microhemorrhages in patients with ischemic stroke. ANN Neurol. *44*, 372–377.

Van Laar, P.J., Van der Grond, J., and Hendrikse, J. (2008). Brain perfusion territory imaging: methods and clinical applications of selective arterial spin-labeling MR imaging. Radiology *246*, 354–364.

Lansberg, M.G., Thijs, V.N., Bammer, R., Kemp, S., Wijman, C.A.C., Marks, M.P., and Albers, G.W. (2007). Risk factors of symptomatic intracerebral hemorrhage after tPA therapy for acute stroke. Stroke *38*, 2275–2278.

Lansberg, M.G., Thijs, V.N., Bammer, R., Olivot, J.-M., Marks, M.P., Wechsler, L.R., Kemp, S., and Albers, G.W. (2008). The MRA-DWI mismatch identifies patients with stroke who are likely to benefit from reperfusion. Stroke *39*, 2491–2496.

Lansberg, M.G., Bluhmki, E., and Thijs, V.N. (2009). Efficacy and safety of tissue plasminogen activator 3 to 4.5 hours after acute ischemic stroke: a meta-analysis. Stroke *40*, 2438–2441.

Lansberg, M.G., Straka, M., Kemp, S., Mlynash, M., Wechsler, L.R., Jovin, T.G., Wilder, M.J., Lutsep, H.L., Czartoski, T.J., Bernstein, R.A., et al. (2012). MRI profile and response to endovascular reperfusion after stroke (DEFUSE 2): a prospective cohort study. The Lancet Neurology *11*, 860–867.

Larrue, V., Kummer, R. von, Müller, A., and Bluhmki, E. (2001). Risk factors for severe hemorrhagic transformation in ischemic stroke patients treated with recombinant tissue plasminogen activator a secondary analysis of the european-australasian acute stroke study (ECASS II). Stroke *32*, 438–441.

Lee, J.-M., Grabb, M.C., Zipfel, G.J., and Choi, D.W. (2000). Brain tissue responses to ischemia. J Clin Invest *106*, 723–731.

Lee, J.-M., Vo, K.D., An, H., Celik, A., Lee, Y., Hsu, C.Y., and Lin, W. (2003). Magnetic resonance cerebral metabolic rate of oxygen utilization in hyperacute stroke patients. ANN Neurol. *53*, 227–232.

Li, F., Han, S., Tatlisumak, T., Carano, R.A.D., Irie, K., Sotak, C.H., and Fisher, M. (1998). A new method to improve in-bore middle cerebral artery occlusion in rats demonstration with diffusion- and perfusion-weighted imaging. Stroke *29*, 1715–1720.

Li, F., Han, S.S., Tatlisumak, T., Liu, K.F., Garcia, J.H., Sotak, C.H., and Fisher, M. (1999). Reversal of acute apparent diffusion coefficient abnormalities and delayed neuronal death following transient focal cerebral ischemia in rats. ANN Neurol. *46*, 333–342.

Li, F., Liu, K.-F., Silva, M.D., Omae, T., Sotak, C.H., Fenstermacher, J.D., and Fisher, M. (2000). Transient and permanent resolution of ischemic lesions on diffusion-weighted imaging after brief periods of focal ischemia in rats correlation with histopathology. Stroke *31*, 946–954.

Li, F., Liu, K.-F., Silva, M.D., Meng, X., Gerriets, T., Helmer, K.G., Fenstermacher, J.D., Sotak, C.H., and Fisher, M. (2002). Acute postischemic renormalization of the apparent diffusion coefficient of water is not associated with reversal of astrocytic swelling and neuronal shrinkage in rats. Am J Neuroradiol. *23*, 180–188.

Li, L., Jiang, Q., Ding, G., Zhang, L., Zhang, Z.G., Ewing, J.R., Knight, R.A., Kapke, A., Soltanian-Zadeh, H., and Chopp, M. (2005). Map-ISODATA demarcates regional response to combination rt-PA and 7E3 F(ab')2 treatment of embolic stroke in the rat. J Magn Reson Imaging *21*, 726–734.

Li, L., Jiang, Q., Zhang, L., Ding, G., Gang Zhang, Z., Li, Q., Ewing, J.R., Lu, M., Panda, S., Ledbetter, K.A., et al. (2007). Angiogenesis and improved cerebral blood flow in the ischemic boundary area detected by MRI after administration of sildenafil to rats with embolic stroke. Brain Res. *1132*, 185–192.

Li, L., Jiang, Q., Ding, G., Zhang, L., Zhang, Z.G., Li, Q., Panda, S., Kapke, A., Lu, M., Ewing, J.R., et al. (2009). MRI Identification of White Matter Reorganization Enhanced by Erythropoietin Treatment in a Rat Model of Focal Ischemia. Stroke *40*, 936–941.

Liebeskind, D.S. (2003). Collateral circulation. Stroke *34*, 2279–2284.

Liebeskind, D.S. (2005). Collaterals in acute stroke: beyond the clot. Neuroimaging Clin. N. Am. *15*, 553–573, x.

Liu, S., Zhen, G., Meloni, B.P., Campbell, K., and Winn, H.R. (2009). Rodent stroke model guidelines for preclinical stroke trials (1st edition). J Exp Stroke Transl Med *2*, 2–27.

Liu, Y., D'Arceuil, H.E., Westmoreland, S., He, J., Duggan, M., Gonzalez, R.G., Pryor, J., and De Crespigny, A.J. (2007). Serial diffusion tensor MRI after transient and permanent cerebral ischemia in nonhuman primates. Stroke *38*, 138–145.

Lo, E.H., Moskowitz, M.A., and Jacobs, T.P. (2005). Exciting, radical, suicidal: how brain cells die after stroke. Stroke *36*, 189–192.

Longa, E.Z., Weinstein, P.R., Carlson, S., and Cummins, R. (1989). Reversible middle cerebral artery occlusion without craniectomy in rats. Stroke *20*, 84–91.

Lopez, A.D., and Mathers, C.D. (2006). Measuring the global burden of disease and epidemiological transitions: 2002-2030. Ann Trop Med Parasitol *100*, 481–499.

Lu, M., Mitsias, P.D., Ewing, J.R., Soltanian-Zadeh, H., Bagher-Ebadian, H., Zhao, Q., Oja-Tebbe, N., Patel, S.C., and Chopp, M. (2005). Predicting final infarct size using acute and subacute multiparametric MRI measurements in patients with ischemic stroke. Journal of Magnetic Resonance Imaging *21*, 495–502.

Ma, H., Zavala, J.A., Teoh, H., Churilov, L., Gunawan, M., Ly, J., Wright, P., Phan, T., Arakawa, S., Davis, S.M., et al. (2009). Fragmentation of the classical magnetic resonance mismatch "penumbral" pattern with time. Stroke *40*, 3752–3757.

Marchal, G., Beaudouin, V., Rioux, P., De la Sayette, V., Le Doze, F., Viader, F., Derlon, J.M., and Baron, J.C. (1996). Prolonged persistence of substantial volumes of potentially viable brain tissue after stroke: a correlative PET-CT study with voxel-based data analysis. Stroke *27*, 599–606.

Marder, V.J., Chute, D.J., Starkman, S., Abolian, A.M., Kidwell, C., Liebeskind, D., Ovbiagele, B., Vinuela, F., Duckwiler, G., Jahan, R., et al. (2006). Analysis of thrombi retrieved from cerebral arteries of patients with acute ischemic stroke. Stroke *37*, 2086–2093.

Marinkovic, S.V., Milisavljevic, M.M., Kovacevic, M.S., and Stevic, Z.D. (1985). Perforating branches of the middle cerebral artery. Microanatomy and clinical significance of their intracerebral segments. Stroke *16*, 1022–1029.

Marks, M.P., Olivot, J.-M., Kemp, S., Lansberg, M.G., Bammer, R., Wechsler, L.R., Albers, G.W., and Thijs, V. (2008). Patients with acute stroke treated with intravenous tPA 3-6 hours after stroke onset: correlations between MR angiography findings and perfusion- and diffusion-weighted imaging in the DEFUSE study. Radiology *249*, 614–623.

McCabe, C., Gallagher, L., Gsell, W., Graham, D., Dominiczak, A.F., and MacRae, I.M. (2009). Differences in the evolution of the ischemic penumbra in stroke-prone spontaneously hypertensive and wistar-kyoto rats. Stroke *40*, 3864–3868.

Menezes, N.M., Ay, H., Wang Zhu, M., Lopez, C.J., Singhal, A.B., Karonen, J.O., Aronen, H.J., Liu, Y., Nuutinen, J., Koroshetz, W.J., et al. (2007). The real estate factor quantifying the impact of infarct location on stroke severity. Stroke *38*, 194–197.

Meng, X., Fisher, M., Shen, Q., Sotak, C.H., and Duong, T.Q. (2004). Characterizing the diffusion/perfusion mismatch in experimental focal cerebral ischemia. ANN Neurol. *55*, 207–212.

Menzies, S.A., Betz, A.L., and Hoff, J.T. (1993). Contributions of ions and albumin to the formation and resolution of ischemic brain edema. J. Neurosurg. *78*, 257–266.

Mergenthaler, P., and Meisel, A. (2012). Do stroke models model stroke? Dis Model Mech. *5*, 718–725.

Minematsu, K., Li, L., Sotak, C.H., Davis, M.A., and Fisher, M. (1992). Reversible focal ischemic injury demonstrated by diffusion-weighted magnetic resonance imaging in rats. Stroke *23*, 1304–1310; discussion 1310–1311.

Mitsias, P.D., Jacobs, M.A., Hammoud, R., Pasnoor, M., Santhakumar, S., Papamitsakis, N.I., Soltanian-Zadeh, H., Lu, M., Chopp, M., and Patel, S.C. (2002). Multiparametric MRI ISODATA ischemic lesion analysis: correlation with the clinical neurological deficit and single-parameter MRI techniques. Stroke *33*, 2839–2844.

Mlynash, M., Lansberg, M.G., Silva, D.A.D., Lee, J., Christensen, S., Straka, M., Campbell, B.C.V., Bammer, R., Olivot, J.-M., Desmond, P., et al. (2011). Refining the definition of the malignant profile insights from the defuse-epithet pooled data set. Stroke *42*, 1270–1275.

Moseley, M.E., Kucharczyk, J., Mintorovitch, J., Cohen, Y., Kurhanewicz, J., Derugin, N., Asgari, H., and Norman, D. (1990). Diffusion-weighted MR imaging of acute stroke: correlation with T_2-weighted and magnetic susceptibility-enhanced MR imaging in cats. AJNR Am J Neuroradiol *11*, 423–429.

Mottet I., Demeure R., Rataud J., Lucas M., Wahl F., Warscotte V., Thiran JP., Goudemant JF., et al. (1997). Effects of riluzole on the evolution of focal cerebral ischemia: a magnetic resonance imaging study. MAGMA *5*, 185–191.

Mouridsen, K., Friston, K., Hjort, N., Gyldensted, L., Østergaard, L., and Kiebel, S. (2006). Bayesian estimation of cerebral perfusion using a physiological model of microvasculature. NeuroImage *33*, 570–579.

Moustafa, R.R., and Baron, J.-C. (2008). Pathophysiology of ischaemic stroke: insights from imaging, and implications for therapy and drug discovery. Brit J Pharmacol. *153*, S44–S54.

Munoz Maniega, S., Bastin, M.E., Armitage, P.A., Farrall, A.J., Carpenter, T.K., Hand, P.J., Cvoro, V., Rivers, C.S., and Wardlaw, J.M. (2004). Temporal evolution of water diffusion parameters is different in grey and white matter in human ischaemic stroke. J Neurol, Neurosurg Psych. *75*, 1714–1718.

Nagakane, Y., Christensen, S., Brekenfeld, C., Ma, H., Churilov, L., Parsons, M.W., Levi, C.R., Butcher, K.S., Peeters, A., Barber, P.A., et al. (2010). EPITHET. Positive result after reanalysis using baseline diffusion-weighted imaging/perfusion-weighted imaging co-registration. Stroke.

Nagesh, V., Welch, K.M., Windham, J.P., Patel, S., Levine, S.R., Hearshen, D., Peck, D., Robbins, K., D'Olhaberriague, L., Soltanian-Zadeh, H., et al. (1998). Time course of ADCw changes in ischemic stroke: beyond the human eye! Stroke *29*, 1778–1782.

Neumann-Haefelin, C., Brinker, G., Uhlenküken, U., Pillekamp, F., Hossmann, K.-A., and Hoehn, M. (2002). Prediction of hemorrhagic transformation after thrombolytic therapy of clot embolism: An MRI investigation in rat brain. Stroke *33*, 1392–1398.

Neumann-Haefelin, T., Kastrup, A., De Crespigny, A., Yenari, M.A., Ringer, T., Sun, G.H., and Moseley, M.E. (2000). Serial MRI after transient focal cerebral ischemia in rats: dynamics of tissue injury, blood-brain barrier damage, and edema formation. Stroke *31*, 1965–1972; discussion 1972–1973.

Nicoli, F., Micheaux, P.L. de, and Girard, N. (2012). Perfusion-weighted imaging–derived collateral flow index is a predictor of MCA M1 recanalization after IV thrombolysis. Am J Neuroradiol. *34*,107-114.

Niiro, M., Simon, R.P., Kadota, K., and Asakura, T. (1996). Proximal branching patterns of middle cerebral artery (MCA) in rats and their influence on the infarct size produced by MCA occlusion. J Neurosc Meth. *64*, 19–23.

Olah, L., Wecker, S., and Hoehn, M. (2000). Secondary deterioration of apparent diffusion coefficient after 1-hour transient focal cerebral ischemia in rats. J Cereb Blood Flow Metab. *20*, 1474–1482.

Olivot, J.M., and Marks, M.P. (2008). Magnetic resonance imaging in the evaluation of acute stroke. Topics in Magnetic Resonance Imaging *19*, 225–230.

Olivot, J.-M., Mlynash, M., Thijs, V.N., Purushotham, A., Kemp, S., Lansberg, M.G., Wechsler, L., Bammer, R., Marks, M.P., and Albers, G.W. (2009a). Relationships between cerebral perfusion and reversibility of acute diffusion lesions in DEFUSE: insights from RADAR. Stroke *40*, 1692–1697.

Olivot, J.-M., Mlynash, M., Thijs, V.N., Kemp, S., Lansberg, M.G., Wechsler, L., Bammer, R., Marks, M.P., and Albers, G.W. (2009b). Optimal Tmax threshold for predicting penumbral tissue in acute stroke. Stroke *40*, 469–475.

Østergaard, L., Jónsdóttir, K.Y., and Mouridsen, K. (2009). Predicting tissue outcome in stroke: new approaches. Curr Opin Neurol. *22*, 54–59.

Østergaard, L. (2004). Cerebral perfusion imaging by bolus tracking. Top Magn Reson Imaging *15*, 3–9.

Østergaard, L., Weisskoff, R.M., Chesler, D.A., Gyldensted, C., and Rosen, B.R. (1996). High resolution measurement of cerebral blood flow using intravascular tracer bolus passages. Part I: Mathematical approach and statistical analysis. Magn Reson Med. *36*, 715–725.

Otsu, N. (1979). A threshold selection method from gray-level histograms. IEEE Trans Syst, Man Cybern. *9*, 62–66.

Overgaard, K., Rasmussen, R.S., and Johansen, F.F. (2010). The site of embolization related to infarct size, oedema and clinical outcome in a rat stroke model - further translational stroke research. Exp Transl Stroke Med. *2*, 17.

Pan, J., Konstas, A.-A., Bateman, B., Ortolano, G.A., and Pile-Spellman, J. (2007). Reperfusion injury following cerebral ischemia: pathophysiology, MR imaging, and potential therapies. Neuroradiology *49*, 93–102.

Patlak, C.S., and Blasberg, R.G. (1985). Graphical evaluation of blood-to-brain transfer constants from multiple-time uptake data. generalizations. J Cereb Blood Flow Metab. *5*, 584–590.

Patlak, C.S., Blasberg, R.G., and Fenstermacher, J.D. (1983). Graphical evaluation of blood-to-brain transfer constants from multiple-time uptake data. J. Cereb. Blood Flow Metab. *3*, 1–7.

Phan, T.G., Fong, A.C., Donnan, G.A., Srikanth, V., and Reutens, D.C. (2009). Digital probabilistic atlas of the border region between the middle and posterior cerebral arteries. Cerebrovasc. Dis. *27*, 529–536.

Pierpaoli, C., Righini, A., Linfante, I., Tao-Cheng, J.H., Alger, J.R., and Chiro, G.D. (1993). Histopathologic correlates of abnormal water diffusion in cerebral ischemia: diffusion-weighted MR imaging and light and electron microscopic study. Radiology *189*, 439–448.

Pierpaoli, C., Alger, J.R., Righini, A., Mattiello, J., Dickerson, R., Pres, D.D., Barnett, A., and Chiro, G.D. (1996). High temporal resolution diffusion mri of global cerebral ischemia and reperfusion. J Cereb Blood Flow Metab. *16*, 892–905.

Pitkonen, M., Abo-Ramadan, U., Marinkovic, I., Pedrono, E., Hasan, K.M., Strbian, D., Durukan, A., and Tatlisumak, T. (2012). Long-term evolution of diffusion tensor indices after temporary experimental ischemic stroke in rats. Brain Res. *1445*, 103–110.

R Development Core (2011). R: A Language and Environment for Statistical Computing. R Foundation for Statistical Computing, Vienna. ISBN 3-900051-07-0

Reese, T., Bochelen, D., Sauter, A., Beckmann, N., and Rudin, M. (1999). Magnetic resonance angiography of the rat cerebrovascular system without the use of contrast agents. NMR Biomed. *12*, 189–196.

Reid, E., Graham, D., Lopez-Gonzalez, M.R., Holmes, W.M., Macrae, I.M., and McCabe, C. (2012). Penumbra detection using PWI/DWI mismatch MRI in a rat stroke model with and without comorbidity: comparison of methods. J Cereb Blood Flow Metab. *32,*1765-1777.

Rose, S.E., Janke, A.L., Griffin, M., Finnigan, S., and Chalk, J.B. (2004). Improved prediction of final infarct volume using bolus delay-corrected perfusion-weighted mri: implications for the ischemic penumbra. Stroke *35*, 2466–2471.

Rosell, A., Foerch, C., Murata, Y., and Lo, E.H. (2008). Mechanisms and markers for hemorrhagic transformation after stroke. Cerebral Hemorrhage, L.-F. Zhou, X.-C. Chen, F.-P. Huang, G. Xi, R.F. Keep, Y. Hua, K. Muraszko, and Y.-C. Lu, eds. (Springer Vienna), pp. 173–178.

Rosen, B.R., Belliveau, J.W., Vevea, J.M., and Brady, T.J. (1990). Perfusion imaging with NMR contrast agents. Magn Reson Med. *14*, 249–265.

Rozanski, M., Ebinger, M., Schmidt, W.U., Hotter, B., Pittl, S., Heuschmann, P.U., Jungehuelsing, J.G., and Fiebach, J.B. (2010). Hyperintense acute reperfusion marker on FLAIR is not associated with early haemorrhagic transformation in the elderly. Eur Radiol. *20*, 2990–2996.

Saarinen, J.T., Sillanpää, N., Rusanen, H., Hakomäki, J., Huhtala, H., Lähteelä, A., Dastidar, P., Soimakallio, S., and Elovaara, I. (2012). The mid-M1 segment of the middle cerebral artery is a cutoff clot location for good outcome in intravenous thrombolysis. Eur J Neurol. *19,*1121-1127.

Sahin, B., Aslan, H., Unal, B., Canan, S., Bilgic, S., Kaplan, S., and Tumkaya, L. (2011). Brain volumes of the lamb, rat and bird do not show hemispheric asymmetry: a stereological study. Imag Anal Stereol. *20*, 9–13.

Schellinger, P.D., and Köhrmann, M. (2008). MRA/DWI mismatch: a novel concept or something one could get easier and cheaper? Stroke *39*, 2423–2424.

Schellinger, P.D., Bryan, R.N., Caplan, L.R., Detre, J.A., Edelman, R.R., Jaigobin, C., Kidwell, C.S., Mohr, J.P., Sloan, M., Sorensen, A.G., et al. (2010). Evidence-based guideline: the role of diffusion and perfusion MRI for the diagnosis of acute ischemic stroke: report of the therapeutics and technology assessment subcommittee of the American academy of neurology. Neurology *75*, 177–185.

Schwamm, L.H., Koroshetz, W.J., Sorensen, A.G., Wang, B., Copen, W.A., Budzik, R., Rordorf, G., Buonanno, F.S., Schaefer, P.W., and Gonzalez, R.G. (1998). Time course of lesion development in patients with acute stroke : serial diffusion- and hemodynamic-weighted magnetic resonance imaging. Stroke *29*, 2268 –2276.

Seitz, R.J., Sondermann, V., Wittsack, H.-J., and Siebler, M. (2009). Lesion patterns in successful and failed thrombolysis in middle cerebral artery stroke. Neuroradiology *51*, 865–871.

Selim, M., Fink, J.N., Kumar, S., Caplan, L.R., Horkan, C., Chen, Y., Linfante, I., and Schlaug, G. (2002). Predictors of hemorrhagic transformation after intravenous recombinant tissue plasminogen activator prognostic value of the initial apparent diffusion coefficient and diffusion-weighted lesion volume. Stroke *33*, 2047–2052.

Sevick, R.J., Kanda, F., Mintorovitch, J., Arieff, A.I., Kucharczyk, J., Tsuruda, J.S., Norman, D., and Moseley, M.E. (1992). Cytotoxic brain edema: assessment with diffusion-weighted MR imaging. Radiology *185*, 687–690.

Shen, Q., and Duong, T.Q. (2008). Quantitative prediction of ischemic stroke tissue fate. NMR Biomed. *21*, 839–848.

Shen, Q., Fisher, M., Sotak, C.H., and Duong, T.Q. (2004a). Effects of reperfusion on ADC and CBF pixel-by-pixel dynamics in stroke: characterizing tissue fates using quantitative diffusion and perfusion imaging. J. Cereb Blood Flow Metab. *24*, 280–290.

Shen, Q., Ren, H., Fisher, M., Bouley, J., and Duong, T.Q. (2004b). Dynamic tracking of acute ischemic tissue fates using improved unsupervised ISODATA analysis of high-resolution quantitative perfusion and diffusion data. J.Cereb.Blood Flow Metab. *24*, 887–897.

Shen, Q., Ren, H., Cheng, H., Fisher, M., and Duong, T.Q. (2005). Functional, perfusion and diffusion MRI of acute focal ischemic brain injury. J Cereb Blood Flow Metab *25*, 1265–1279.

Siemonsen, S., Mouridsen, K., Holst, B., Ries, T., Finsterbusch, J., Thomalla, G., Ostergaard, L., and Fiehler, J. (2009). Quantitative T2 values predict time from symptom onset in acute stroke patients. Stroke *40*, 1612–1616.

Siemonsen, S., Löbel, U., Sedlacik, J., Forkert, N.D., Mouridsen, K., Ostergaard, L., Thomalla, G., and Fiehler, J. (2012). Elevated T2-values in MRI of stroke patients shortly after symptom onset do not predict irreversible tissue infarction. Brain *135*, 1981–1989.

De Silva, D.A., Brekenfeld, C., Ebinger, M., Christensen, S., Barber, P.A., Butcher, K.S., Levi, C.R., Parsons, M.W., Bladin, C.F., Donnan, G.A., et al. (2010). The benefits of intravenous thrombolysis relate to the site of baseline arterial occlusion in the Echoplanar Imaging Thrombolytic Evaluation Trial (EPITHET). Stroke *41*, 295–299.

Simard, J.M., Kent, T.A., Chen, M., Tarasov, K.V., and Gerzanich, V. (2007). Brain oedema in focal ischaemia: molecular pathophysiology and theoretical implications. Lancet Neurol. *6*, 258–268.

Singer, O.C., Humpich, M.C., Fiehler, J., Albers, G.W., Lansberg, M.G., Kastrup, A., Rovira, A., Liebeskind, D.S., Gass, A., Rosso, C., et al. (2008). Risk for symptomatic intracerebral hemorrhage after thrombolysis assessed by diffusion-weighted magnetic resonance imaging. ANN Neurol. *63*, 52–60.

Smith, S.M. (2002). Fast robust automated brain extraction. Hum.Brain Mapp. *17*, 143–155.

Sobesky, J. (2012). Refining the mismatch concept in acute stroke: lessons learned from PET and MRI. J Cereb Blood Flow Metab. *32,*1416-1425.

Sobesky, J., Zaro Weber, O., Lehnhardt, F.-G., Hesselmann, V., Thiel, A., Dohmen, C., Jacobs, A., Neveling, M., and Heiss, W.-D. (2004). Which time-to-peak threshold best identifies penumbral flow? A comparison of perfusion-weighted magnetic resonance imaging and positron emission tomography in acute ischemic stroke. Stroke *35*, 2843–2847.

Sobesky, J., Zaro Weber, O., Lehnhardt, F.-G., Hesselmann, V., Neveling, M., Jacobs, A., and Heiss, W.-D. (2005). Does the mismatch match the penumbra? Magnetic resonance imaging and positron emission tomography in early ischemic stroke. Stroke *36*, 980–985.

Soltanian-Zadeh, H., Pasnoor, M., Hammoud, R., Jacobs, M.A., Patel, S.C., Mitsias, P.D., Knight, R.A., Zheng, Z.G., Lu, M., and Chopp, M. (2003). MRI tissue characterization of experimental cerebral ischemia in rat. J.Magn Reson.Imaging *17*, 398–409.

Soltanian-Zadeh, H., Bagher-Ebadian, H., Ewing, J.R., Mitsias, P.D., Kapke, A., Lu, M., Jiang, Q., Patel, S.C., and Chopp, M. (2007). Multiparametric iterative self-organizing data analysis of ischemic lesions using pre- or post-Gd T1 MRI. Cerebrovasc Dis. *23*, 91–102.

Sonka, M., Hlavac, V., and Boyle, R. (2007). Image Processing, Analysis, and Machine Vision (CL Engineering).

Sorensen, A.G., Wu, O., Copen, W.A., Davis, T.L., Gonzalez, R.G., Koroshetz, W.J., Reese, T.G., Rosen, B.R., Wedeen, V.J., and Weisskoff, R.M. (1999a). Human acute cerebral ischemia: detection of changes in water diffusion anisotropy by using MR imaging. Radiology *212*, 785–792.

Sorensen, A.G., Copen, W.A., Ostergaard, L., Buonanno, F.S., Gonzalez, R.G., Rordorf, G., Rosen, B.R., Schwamm, L.H., Weisskoff, R.M., and Koroshetz, W.J. (1999b). Hyperacute stroke: simultaneous measurement of relative cerebral blood volume, relative cerebral blood flow, and mean tissue transit time. Radiology *210*, 519–527.

Sourbron, S. (2010). Technical aspects of MR perfusion. Eur J Radiol *76*, 304–313.

Sourbron, S.P., and Buckley, D.L. (2012). Tracer kinetic modelling in MRI: estimating perfusion and capillary permeability. Phys Med Biol. *57*, R1–33.

Staring, M., Klein, S., and Pluim, J.P. (2007). A rigidity penalty term for nonrigid registration. Med Phys. *34*, 4098–4108.

Stejskal, E.O., and Tanner, J.E. (1965). Spin Diffusion Measurements: Spin echoes in the presence of a time-dependent field gradient. J Chem Phys. *42*, 288–292.

Sun, P.Z., Zhou, J., Sun, W., Huang, J., and Zijl, P.C.M. van (2007). Detection of the ischemic penumbra using pH-weighted MRI. J Cereb Blood Flow Metab. *27*, 1129–1136.

Tagaya, M., Liu, K.F., Copeland, B., Seiffert, D., Engler, R., Garcia, J.H., and Del Zoppo, G.J. (1997). DNA scission after focal brain ischemia. Temporal differences in two species. Stroke *28*, 1245–1254.

Thomalla, G., Schwark, C., Sobesky, J., Bluhmki, E., Fiebach, J.B., Fiehler, J., Weber, O.Z., Kucinski, T., Juettler, E., Ringleb, P.A., et al. (2006). Outcome and symptomatic bleeding complications of intravenous thrombolysis within 6 hours in mri-selected stroke patients comparison of a german multicenter study with the pooled data of ATLANTIS, ECASS, and NINDS tPA Trials. Stroke *37*, 852–858.

Thomalla, G., Sobesky, J., Köhrmann, M., Fiebach, J.B., Fiehler, J., Weber, O.Z., Kruetzelmann, A., Kucinski, T., Rosenkranz, M., Röther, J., et al. (2007). Two Tales: Hemorrhagic transformation but not parenchymal hemorrhage after thrombolysis is related to severity and duration of ischemia MRI study of acute stroke patients treated with intravenous tissue plasminogen activator within 6 hours. Stroke *38*, 313–318.

Thompson jr., H.K., Starmer, C.F., Whalen, R.E., and McIntosh, H.D. (1964). Indicator transit time considered as a gamma variate. Circ Res. *14*, 502–515.

Tiebosch, I.A.C.W., Crielaard, B.J., Bouts, M.J.R.J., Zwartbol, R., Salas-Perdomo, A., Lammers, T., Planas, A.M., Storm, G., and Dijkhuizen, R.M. (2012). Combined treatment with recombinant tissue plasminogen activator and dexamethasone phosphate-containing liposomes improves neurological outcome and restricts lesion progression after embolic stroke in rats. J. Neurochem. *123 Suppl 2*, 65–74.

Trouillas, P., and Kummer, R. von (2006). Classification and pathogenesis of cerebral hemorrhages after thrombolysis in ischemic stroke. Stroke *37*, 556–561.

Verheul, H.B., Sprenkel, J.W.B. van der, Tulleken, C. a. F., Tamminga, K.S., and Nicolay, K. (1992). Temporal evolution of focal cerebral ischemia in the rat assessed by T2-weighted and diffusion-weighted magnetic resonance imaging. Brain Topogr. *5*, 171–176.

Vonken, E.-J.P.A., Van Osch, M.J.P., Bakker, C.J.G., and Viergever, M.A. (2000). Simultaneous quantitative cerebral perfusion and Gd-DTPA extravasation measurement with dual-echo dynamic susceptibility contrast MRI. Magn Reson Med. *43*, 820–827.

Vora, N.A., Gupta, R., Thomas, A.J., Horowitz, M.B., Tayal, A.H., Hammer, M.D., Uchino, K., Wechsler, L.R., and Jovin, T.G. (2007). Factors predicting hemorrhagic complications after multimodal reperfusion therapy for acute ischemic stroke. Am J Neuroradiol *28*, 1391–1394.

Vora, N.A., Shook, S.J., Schumacher, H.C., Tievsky, A.L., Albers, G.W., Wechsler, L.R., and Gupta, R. (2011). A 5-Item scale to predict stroke outcome after cortical middle cerebral artery territory infarction: validation from results of the diffusion and perfusion imaging Evaluation for Understanding Stroke Evolution (DEFUSE) Study. Stroke *42*, 645–649.

Wang, C.X., Todd, K.G., Yang, Y., Gordon, T., and Shuaib, A. (2001). Patency of cerebral microvessels after focal embolic stroke in the rat. J Cereb Blood Flow Metab. *21*, 413–421.

Wang, X., Tsuji, K., Lee, S.-R., Ning, M., Furie, K.L., Buchan, A.M., and Lo, E.H. (2004). Mechanisms of hemorrhagic transformation after tissue plasminogen activator reperfusion therapy for ischemic stroke. Stroke *35*, 2726–2730.

Warach, S. (2001). Tissue viability thresholds in acute stroke the 4-factor model. Stroke *32*, 2460–2461.

Warach, S., and Latour, L.L. (2004). Evidence of reperfusion injury, exacerbated by thrombolytic therapy, in human focal brain ischemia using a novel imaging marker of early blood–brain barrier disruption. Stroke *35*, 2659–2661.

Warach, S., Chien, D., Li, W., Ronthal, M., and Edelman, R.R. (1992). Fast magnetic resonance diffusion-weighted imaging of acute human stroke. Neurology *42*, 1717–1723.

Warach, S., Gaa, J., Siewert, B., Wielopolski, P., and Edelman, R.R. (1995). Acute human stroke studied by whole brain echo planar diffusion-weighted magnetic resonance imaging. Ann. Neurol. *37*, 231–241.

Wardlaw, J.M. (2010). Neuroimaging in acute ischaemic stroke: Insights into unanswered questions of pathophysiology. Journal of Internal Medicine *267*, 172–190.

Wardlaw, J.M., Murray, V., Berge, E., Del Zoppo, G., Sandercock, P., Lindley, R.L., and Cohen, G. (2012). Recombinant tissue plasminogen activator for acute ischaemic stroke: an updated systematic review and meta-analysis. The Lancet *379*, 2364–2372.

Weber, R., Wegener, S., Ramos-Cabrer, P., Wiedermann, D., and Hoehn, M. (2005). MRI detection of macrophage activity after experimental stroke in rats: New indicators for late appearance of vascular degradation? Magn Reson Med. *54*, 59–66.

Wegener, S., Gottschalk, B., Jovanovic, V., Knab, R., Fiebach, J.B., Schellinger, P.D., Kucinski, T., Jungehülsing, G.J., Brunecker, P., Müller, B., et al. (2004). Transient ischemic attacks before ischemic stroke: preconditioning the human brain? A multicenter magnetic resonance imaging study. Stroke *35*, 616–621.

Wegener, S., Weber, R., Ramos-Cabrer, P., Uhlenkueken, U., Sprenger, C., Wiedermann, D., Villringer, A., and Hoehn, M. (2006). Temporal profile of T2-weighted MRI distinguishes between pannecrosis and selective neuronal death after transient focal cerebral ischemia in the rat. J Cereb Blood Flow Metab. *26*, 38–47.

Welch, K.M.A., Windham, J., Knight, R.A., Nagesh, V., Hugg, J.W., Jacobs, M., Peck, D., Booker, P., Dereski, M.O., and Levine, S.R. (1995). A model to predict the histopathology of human stroke using diffusion and t2-weighted magnetic resonance imaging. Stroke *26*, 1983–1989.

Willats, L., Connelly, A., Christensen, S., Donnan, G.A., Davis, S.M., and Calamante, F. (2012). The role of bolus delay and dispersion in predictor models for stroke. Stroke *43*, 1025–1031.

Williams, D.S., Detre, J.A., Leigh, J.S., and Koretsky, A.P. (1992). Magnetic resonance imaging of perfusion using spin inversion of arterial water. Proc. Natl. Acad. Sci. *89*, 212–216.

Wintermark, M., Albers, G.W., Alexandrov, A.V., Alger, J.R., Bammer, R., Baron, J.-C., Davis, S., Demaerschalk, B.M., Derdeyn, C.P., Donnan, G.A., et al. (2008). Acute stroke imaging research roadmap. Stroke *39*, 1621–1628.

Wood, S.N. (2006). Generalized additive models: an introduction with R (Chapman & Hall/CRC).

Van der Worp, H.B., Howells, D.W., Sena, E.S., Porritt, M.J., Rewell, S., O'Collins, V., and Macleod, M.R. (2010). Can animal models of disease reliably inform human studies? PLoS Med. *7*, e1000245.

Wu, O., Koroshetz, W.J., Ostergaard, L., Buonanno, F.S., Copen, W.A., Gonzalez, R.G., Rordorf, G., Rosen, B.R., Schwamm, L.H., Weisskoff, R.M., et al. (2001). Predicting tissue outcome in acute human cerebral ischemia using combined diffusion- and perfusion-weighted MR imaging. Stroke *32*, 933–942.

Wu, O., Østergaard, L., Weisskoff, R.M., Benner, T., Rosen, B.R., and Sorensen, A.G. (2003). Tracer arrival timing-insensitive technique for estimating flow in MR perfusion-weighted imaging using singular value decomposition with a block-circulant deconvolution matrix. Magn Reson Med. *50*, 164–174.

Wu, O., Christensen, S., Hjort, N., Dijkhuizen, R.M., Kucinski, T., Fiehler, J., Thomalla, G., Röther, J., and Østergaard, L. (2006). Characterizing physiological heterogeneity of infarction risk in acute human ischaemic stroke using MRI. Brain *129*, 2384–2393.

Wu, O., Sumii, T., Asahi, M., Sasamata, M., Ostergaard, L., Rosen, B.R., Lo, E.H., and Dijkhuizen, R.M. (2007). Infarct prediction and treatment assessment with MRI-based algorithms in experimental stroke models. J Cereb Blood Flow Metab. *27*, 196–204.

Wu, O., Dijkhuizen, R.M., and Sorensen, A.G. (2010). Multiparametric Magnetic Resonance Imaging of Brain Disorders. Top Magn Reson Imag *21*, 129–138.

Wu, O., Schwamm, L.H., and Sorensen, A.G. (2011). Imaging stroke patients with unclear onset times. Neuroimaging Clin N Am. *21*, 327–344, xi.

Wu, O., Benner, T., Roccatagliata, L., Zhu, M., Schaefer, P.W., Sorensen, A.G., and Singhal, A.B. (2012). Evaluating effects of normobaric oxygen therapy in acute stroke with MRI-based predictive models. Med Gas Res. *2*, 5.

Yang, G.Y., and Betz, A.L. (1994). Reperfusion-induced injury to the blood-brain barrier after middle cerebral artery occlusion in rats. Stroke *25*, 1658–1664.

Zaro-Weber, O., Moeller-Hartmann, W., Heiss, W.-D., and Sobesky, J. (2010). Maps of time to maximum and time to peak for mismatch definition in clinical stroke studies validated with positron emission tomography. Stroke *41*, 2817–2821.

Zhang, R.L., Chopp, M., Chen, H., and Garcia, J.H. (1994). Temporal profile of ischemic tissue damage, neutrophil response, and vascular plugging following permanent and transient (2H) middle cerebral artery occlusion in the rat. J Neurol Sci. *125*, 3–10.

Zhang, R.L., Chopp, M., Zhang, Z.G., Jiang, Q., and Ewing, J.R. (1997). A rat model of focal embolic cerebral ischemia. Brain Res. *766*, 83–92.

Zhou, J., Payen, J.-F., Wilson, D.A., Traystman, R.J., and Van Zijl, P.C.M. (2003). Using the amide proton signals of intracellular proteins and peptides to detect pH effects in MRI. Nat Med. *9*, 1085–1090.

Van der Zijden, J.P., Van der Toorn, A., Van der Marel, K., and Dijkhuizen, R.M. (2008). Longitudinal in vivo MRI of alterations in perilesional tissue after transient ischemic stroke in rats. Exp Neurol. *212*, 207–212.

Zoppo, G.J. del, Schmid-Schönbein, G.W., Mori, E., Copeland, B.R., and Chang, C.M. (1991). Polymorphonuclear leukocytes occlude capillaries following middle cerebral artery occlusion and reperfusion in baboons. Stroke *22*, 1276–1283.

Zoppo, G.J.D., Kummer, R.V., and Hamann, G.F. (1998). Ischaemic damage of brain microvessels: inherent risks for thrombolytic treatment in stroke. J Neurol Neurosurg Psych. *65*, 1–9.

Appendices

Summary

Ischemic stroke is a devastating disease that originates from a sudden disruption of blood flow to certain areas of the brain. A complex cascade of pathophysiological processes is triggered by this disruption that may, either directly or secondary to the ischemic insult, lead to various levels of tissue injury. For some tissue possible damage may be averted by intervention, whereas tissue injury may be accelerated for other tissue. Although recent advancements in acute stroke treatment have considerably increased the likelihood of favorable outcome, many patients are still denied a potentially beneficial treatment. Available clot-dissolving treatments are currently restricted by timing guidelines that do not permit treatment beyond 3-4.5 hours after stroke onset, since the potential benefits are outweighed by the potential risks. Yet, more and more recent studies report on patients for which benefit extended well beyond this time-window. Evidently, improved and individualized prediction of tissue injury progression - elucidating potential target areas for intervention or those areas where intervention augments tissue injury - may guide therapeutic decision-making as well as further development of new therapeutic strategies.

The thesis 'Prediction of tissue outcome after experimental stroke using MRI-based algorithms' deals with individualized tissue progression monitoring and tissue outcome prediction using multiparametric magnetic resonance imaging (MRI). Specifically the studies in this thesis aimed to elucidate the potential of voxel-based statistical models for improved prediction of tissue outcome after stroke.

A short introduction in the complex pathophysiological processes involved in tissue injury progression after stroke is presented in the first part of ***Chapter 1***. This part introduces the important concept of the 'ischemic penumbra', which is the area characterized by moderately reduced blood flow that may remain viable for prolonged periods of time. Viability is however limited and with absence of intervention this penumbra will become part of the irreversibly damaged ischemic 'core'. Therefore the penumbra is considered a potential target for therapeutic intervention. This section also emphasizes the possibility of delayed ischemic injury and the importance of blood-brain barrier integrity. The *second part* of this chapter highlights magnetic resonance imaging (MRI) as a versatile tool in the assessment of various stages of tissue damage due to cerebral ischemia. By means of MRI numerous aspects of the tissue - including its structural, hemodynamic, and functional status - can be derived. The *third part* deals with several MRI-based methods for the prediction of tissue outcome after stroke. This part introduces simple, volume-based prediction methods like the perfusion-diffusion mismatch or angiography-diffusion mismatch, but also more advanced multiparametric, voxel-wise methods. Finally, this chapter describes various animal models of

stroke that facilitate longitudinal monitoring of tissue injury progression in a well-controllable and representative setting.
In ***Chapter 2*** we aimed to identify unique spatiotemporal magnetic resonance imaging (MRI) patterns in macaque brain at acute, subacute, and chronic stages after experimental stroke. To that aim T_2 and diffusion changes after permanent or transient middle cerebral artery (MCA) occlusion were evaluated with a modified ISODATA algorithm. This algorithm aims to find groups of similar data to subsequently group them as a separate cluster. Five distinct evolutionary patterns were distinguished that were substantially different from the normal tissue pattern. These patterns were furthermore dependent on the duration of ischemia and varying degrees of tissue injury, as histologically validated. Two signatures identified areas of progressive injury marked by severe necrosis. Another signature identified less severe but pronounced neuronal and axonal degeneration. The other signatures depicted tissue remodeling with vascular proliferation and astrogliosis. These results imply that volumetric analysis of tissue progression obscures heterogeneous development of tissue with different histopathological features. It furthermore demonstrates the potential of aggregating temporal and spatial information on a voxel-wise basis for the generation of tissue signatures with specific histopathological outcome.

In ***Chapter 3***, the relationship between flow obstruction in different segments of the Circle of Willis and the pattern of acute ischemic lesions in normotensive and hypertensive rats were assessed with diffusion and perfusion imaging. Furthermore, this relationship was used to determine the probability of subsequent beneficial reperfusion. Hypertensive rats displayed significantly larger cortical perfusion lesions than normotensive rats for similar patterns of occlusion of the circle of Willis. Proximal MCA occlusions in conjunction with internal carotid artery occlusions displayed largest acute diffusion and perfusion lesions. Follow-up imaging, of a subset of the available animals, revealed that an angiography-diffusion mismatch was more specific in selecting those animals that benefitted from reperfusion than the perfusion-diffusion mismatch. However, the angiography-diffusion mismatch also excluded animals that actually experienced benefit from reperfusion. These results imply that despite the potential of the MR angiography-diffusion mismatch to aid in identifying tissue amenability to reperfusion, it does not provide direct information on local perfusion or collateral flow, information that may further support estimation of local ischemic severity.

In ***Chapter 4*** various voxel-wise prediction algorithms were tested to determine their ability of identifying potentially salvageable tissue. To that aim five predictive algorithms: a generalized linear model (GLM), generalized additive model (GAM), support vector machine (SVM), adaptive boosting (ADA), and a random forest (RF), were employed to determine their efficacy of depicting the tissue at risk of infarction.

Furthermore these algorithms were used to determine their ability to differentiate potentially salvageable tissue from irreversibly damaged tissue. Acute and follow-up T_2, diffusion, and perfusion imaging (PWI) were conducted on animals subjected to right-sided MCA occlusion with or without subsequent reperfusion. All algorithms predicted the extent of infarction equally well. However the infarct probability distribution differed between the algorithms. The infarct probability difference between irreversibly injured tissue and tissue with a potentially salvageable injury was largest for predictions made by a generalized linear model. This resulted in the highest accuracy for infarction risk-based identification of tissue that could recover upon reperfusion. This multiparametric prediction study revealed that not all predictive algorithms were able to predict tissue with a disparate outcome, despite equally accurate predictions of the extent of infarction.

The potential benefits of thrombolysis are offset to an increased risk of hemorrhage. ***Chapter 5*** aimed at elucidating the ability of voxel-wise prediction algorithms to calculate the risk of secondary bleeding (i.e. hemorrhagic transformation) after ischemic stroke. To that aim, multiple MR imaging methods (T_2, T_2*, DWI, PWI, and blood-brain barrier integrity imaging) were employed in spontaneously hypertensive rats. These rats were subjected to right-sided embolic MCA-occlusion with and without subsequent thrombolytic treatment. The integrated predictions using GLM or RF-based prediction algorithms were more accurate than diffusion, and perfusion-based thresholding. Particularly RF-based predictions including additional spatial features resulted in highest accuracy. However, the actual overlap of the predicted hemorrhagic areas and the areas that actually hemorrhaged was lower compared to the infarct-based predictions. This suggests that multiparametric prediction methods enable early identification of post-ischemic tissue at risk of hemorrhagic transformation. Yet, it also suggests that in our studies the actual hemorrhagic development is not only dependent on early ischemic damage but furthermore depends on complex factors that may arise beyond the timepoint of acute MRI assessment.

Results from preceding chapters are evaluated in Chapter 6 against different multiparametric predictive approaches and their diagnostic and prognostic capabilities. The perfusion-diffusion mismatch as a tool for identifying tissue amenable for thrombolytic therapy is discussed. The perfusion-diffusion mismatch may function as a sensitive marker for identifying subjects amenable for thrombolytic treatment. However, its application as a tool for specifically identifying the ischemic penumbra is challenged by its lack of clear standardization consensus. The advantages of the MR angiography-diffusion mismatch are weighted against its drawbacks. Consequently it is advised that complementary use of perfusion, diffusion, and angiography may gain improved insights of the underlying vasculopathy thus better informing on the consequences

of treatment decisions. This chapter also discusses the multiparametric predictive algorithms and emphasized that their utility goes beyond the prediction of the extent of infarction. It is also discussed that particularly improving training data with spatial as well as non-imaging markers may contribute to ameliorated predictions. Conclusively, speculations are made on the future role of multiparametric algorithms in both pre-clinical and clinical stroke research. Evidently, voxel-wise integration of a multitude of (MR imaging-based) biomarkers, representing complex and heterogeneous disease mechanisms, offers unique opportunities to differentiate and track heterogeneous tissue progression without the need for defining restricted viability thresholds. Further advancements, including developments in new MR imaging biomarkers as well as predictive algorithms, offer exciting prospects for incorporating multiparametric algorithms in (pre-)clinical stroke treatment studies and point toward appealing opportunities in improved personalized health-care in the near future.

Samenvatting

Ischemische beroerte is een verwoestende ziekte die voortkomt uit een plotselinge verstoring van de bloedtoevoer naar bepaalde hersengebieden. Zowel direct na als in een latere fase na de verstoring wordt een complexe cascade van pathofysiologische processen geactiveerd die kan leiden tot verschillende niveaus van weefselbeschadiging. Voor bepaald hersenweefsel kan interventie weefselschade afwenden, terwijl voor andere weefsels ontwikkeling van weefselbeschadiging kan worden versneld. Hoewel recente ontwikkelingen in beroertebehandelingen voor wat betreft het verloop van een beroerte aanzienlijke successen hebben geboekt, wordt nog veel patiënten een potentieel gunstige behandeling ontzegt. Beschikbare behandelingen zijn gebonden aan een strict tijdsinterval van niet meer dan 4.5 uur na het optreden van de beroerte, waarna de potentiele risico's zwaarder gaan wegen dan het mogelijk te behalen voordeel. Echter, meer en meer recente studies rapporteren dat bij bepaalde patiëntgroepen behandeling ruim na dit tijdsinterval nog steeds bijdraagt aan een voorspoedig herstel. Logischerwijs kunnen verbeterde en geïndividualiseerde voorspellingen van weefselbeschadigingsprogressie bijdragen tot een betere therapeutische besluitvorming en verdere ontwikkeling van nieuwe therapeutische strategieën ondersteunen.

Het proefschrift 'Voorspelling van hersenschade na een experimentele beroerte met op MRI gebaseerde algoritmen' bestudeert geïndividualiseerde weefselprogressie monitoring en hersenschade voorspelling met behulp van multiparametrische magnetische spin-resonantie beeldvormingstechnieken. De studies in dit proefschrift zijn met name gericht op het verhelderen van de toepasbaarheid van op MRI gebaseerde statistische modellen om zo bij te dragen aan een verbeterde voorspelling van potentiële hersenschade na een beroerte.

Een korte introductie in de complexe pathofysiologische processen die betrokken zijn bij de progressie van weefselbeschadiging na een beroerte wordt gepresenteerd in het eerste deel van ***Hoofdstuk 1***. Dit deel introduceert het belangrijke concept van de 'ischemische penumbra', het gebied gekenmerkt door een gematigd verminderde bloedtoevoer en waarin de levensvatbaarheid van het weefsel gedurende een beperkte tijdsperiode behouden blijft. Met het uitblijven van interventie zal dit gebied langzaam deel gaan uitmaken van het onherstelbaar beschadigde ischemische gebied. Daarom wordt dit gebied gezien als een potentieel doelwit voor therapeutische interventie. Verder benadrukt dit hoofdstuk het belang van vertraagde ischemische schade en de rol van de integriteit van de bloed-hersenbarrière daarin. Het tweede deel van dit hoofdstuk belicht 'Magnetic Resonance Imaging' (MRI) als een veelzijdige techniek voor de beoordeling van de verschillende stadia van cerebrale ischemie. Door middel van MRI kunnen talrijke aspecten van het weefsel – inclusief de structurele,

hemodynamische en functionele status – worden afgeleid. Het derde deel gaat over een aantal op MRI gebaseerde methoden voor het voorspellen van weefselschade na een beroerte. Dit deel introduceert simpele methoden zoals de perfusie-diffusie mismatch of de angiografie-diffusie mismatch, maar ook meer geavanceerde, op voxel gebaseerde, multiparametrische methoden. Tot slot worden in dit hoofdstuk ook verschillende diermodellen besproken die het mogelijk maken om de ontwikkeling van longitudinale weefselschadeontwikkeling op een goed controleerbare en representatieve wijze te bestuderen.

In ***Hoofdstuk 2*** was het doel om unieke spatiotemporele MRI-patronen in makaak hersenen op acute, subacute en chronische tijdspunten na een experimentele beroerte te identificeren. Daarvoor werden T_2 en diffusie-gewogen veranderingen na een permanente of een tijdelijke afsluiting van de middelste cerebrale arterie (MCA) geëvalueerd met een aangepast ISODATA-algoritme. Dit algoritme zoekt overeenkomstige gebieden in de data om deze vervolgens in aparte data clusters te groeperen. Vijf verschillende evolutionaire patronen werden onderscheiden die wezenlijk verschilden van het normale weefselpatroon. Deze patronen waren sterk afhankelijk van de duur van ischemie. Verder toonde validatie met histologie verschillende mate van weefselbeschadiging aan. Twee patronen identificeerden gebieden van progressief letsel gekenmerkt door ernstig necrose. Een ander patroon werd getypeerd door minder ernstige schade, maar neuronale en axonale degeneratie waren ook in dat patroon nog aanwezig. De andere patronen representeerden vasculaire proliferatie en astrogliose. Deze resultaten impliceren dat volumetrische analyse van weefselprogressie heterogene weefselontwikkeling met verschillende histopathologische kenmerken kunnen verbloemen. Het toont verder de potentie van het op een voxel-wijze aggregeren van temporele en ruimtelijke informatie voor het genereren van weefselpatronen met specifieke histopathologische kenmerken.

In ***Hoofdstuk 3*** werd het verband tussen de stromingsobstructie van diverse segmenten van de cirkel van Willis en het patroon van acute ischemische laesie ontwikkeling in zowel normotensieve als hypertensieve ratten bepaald aan de hand van diffusie en perfusie beeldvorming. Verder werd dit verband ook gebruikt voor het bepalen opvolgend voordeel van het weer herstellen van de doorbloeding. Hypertensieve ratten ontwikkelden aanzienlijk grotere corticale perfusie laesies dan normotensieve ratten voor vergelijkbare afgesloten segmenten van de cirkel van Willis. Proximale MCA-occlusie in combinatie met interne carotide occlusies resulteerden in de grootste acute diffusie en perfusie laesies. Opvolgende beeldvorming van een subgroep van de dieren toonde aan dat een angiografie-diffusie mismatch meer specifiek was in het selecteren van dieren die profiteerden van reperfusie dan een perfusie-diffusie mismatch. Echter, de angiografie-diffusie

mismatch excludeerde ook dieren die daadwerkelijk profiteerden van reperfusie. Dus ondanks het potentieel van de angiografie-diffusie mismatch om te assisteren bij het identificeren van weefsel dat vatbaar is voor reperfusie, geeft het geen directe informatie over de lokale perfusie of collaterale stroomgebieden, informatie die een schatting van de ernst van lokale ischemie verder kan ondersteunen.

In ***Hoofdstuk 4*** werden verschillende op voxel gebaseerde voorspellingsalgoritmen getest op hun vermogen voor het identificeren van weefsel dat mogelijk kan hestellen na reperfusie. Vijf voorspellende algoritmen: een generalized linear model (GLM), generalized additive model (GAM), support vector machine (SVM), adaptive boosting (ADA), en een random forest (RF), werden toegepast om hun effectiviteit in het voorspellen van herseninfarct te bepalen. Verder werden de algoritmen getoetst op hun vermogen om potentieel herstelbaar weefsel van onherstelbaar beschadigd weefsel te onderscheiden. Acute en opvolgende T_2, diffusie-gewogen (DWI) en perfusie-gewogen beeldvorming (PWI) werden uitgevoerd op dieren die werden onderworpen aan een rechtszijdige MCA-occlusie met of zonder daaropvolgend herstel van de bloedtoevoer. Alle algoritmen voorspelden de omvang van het infarct even goed. Maar de infarct-probabiliteits distributies verschilden aanzienlijk tussen de algoritmen. Het infarct-probabiliteitsverschil tussen onherstelbaar aangedaan weefsel en weefsel met een potentieel omkeerbare aandoening was het grootst voor de voorspellingen gebaseerd op een GLM. Dit resulteerde in de hoogste nauwkeurigheid voor op infarct risico gebaseerde identificatie van weefsel dat zich kon herstellen na reperfusie. Deze multiparametrische voorspellingsstudie toonde aan dat niet alle voorspellingsalgoritmen in staat waren om een op voxel gebaseerde differentiatie tussen de verschillende mate van weefselschade te ondersteunen, ondanks dat ze nauwkeurig de omvang van het infarct voorspelden.

De potentiële voordelen van trombolyse worden afgewogen tegen een verhoogd risico op bloedingen. ***Hoofdstuk 5*** richtte zich derhalve op het vermogen van op voxel gebaseerde voorspellingsalgoritmen om het risico van de ontwikkeling van een secundaire bloeding (m.a.w. hemorragische transformatie) na een ischemische beroerte te berekenen. In dit hoofdstuk werden meerdere MRI-methoden (T_2, T_2 *, DWI, PWI en bloed-hersenbarrière integriteits beeldvorming) gebruikt om hemorragische transformatie te voorspellen bij spontaan hypertensieve ratten. Deze ratten werden onderworpen aan een rechtszijdige embolische MCA-occlusie om vervolgens wel of geen thrombolysebehandeling te ontvangen. De geïntegreerde bloedingsvoorspellingen van de op GLM of RF gebaseerde voorspellingsalgoritmen waren nauwkeuriger dan de op diffusie- en perfusie-gebaseerde drempelwaardebepalingen. Met name de op RF gebaseerde voorspellingen met aanvullende ruimtelijke karakteristieken resulteerden in de hoogste nauwkeurigheid. De feitelijke overlap van de voorspelde hemorragische

gebieden en de gebieden die daadwerkelijk bloedingen vertoonden daarentegen waren lager dan de op infarct gebaseerde voorspellingen. Dit suggereert dat een multiparametrische voorspellingsmethode een vroege identificatie van post-ischemisch weefsel met verhoogd risico op hemorragische transformatie mogelijk maakt. Echter, dit suggereert ook dat de daadwerkelijke hemorragische ontwikkeling niet alleen afhankelijk is van vroege, ischemische schade, maar ook afhangt van complexe factoren die kunnen plaatsvinden na het tijdspunt van MRI-karakterisatie.

De bevindingen van de voorgaande hoofdstukken worden in ***Hoofdstuk 6*** geëvalueerd vanuit het oogpunt van verschillende multiparametrische op MRI gebaseerde voorspellende benaderingen en hun diagnostische en prognostische mogelijkheden. De perfusie-diffusie mismatch die dienst kan doen als een hulpmiddel voor het identificeren van weefsel vatbaar voor trombolytische therapie wordt besproken. De perfusie-diffusie mismatch kan functioneren als een gevoelige marker voor het identificeren van die patiënten die mogelijk positief reageren op een trombolytische behandeling. Echter, de toepassing als een hulpmiddel voor de specifieke aanduiding van de ischemische penumbra wordt bekritiseerd door het ontbreken van een duidelijke consensus in standardisatie. De voordelen van de MR angiografie-diffusie mismatch worden afgewogen tegen de nadelen van waaruit wordt gesuggereerd dat het gelijktijdig gebruik van de perfusie, diffusie, en angiografie kan leiden tot verbeterd inzicht in de onderliggende vasculopathie. Deze informatie kan bijdragen tot een verbeterd inzicht in de gevolgen van therapeutische beslissingen. In dit hoofdstuk wordt ook ingegaan op de multiparametrische voorspellingsalgoritmen. Hierin wordt benadrukt dat het nut van deze voorspellingsalgoritmes verder gaat dan de voorspelling van de omvang van het infarct. Ook wordt besproken dat met name aanvullende niet op MRI gebaseerde data, zoals ruimtelijke en niet-beeldvormende kenmerken, kunnen bijdragen tot verbeterde voorspellingen. Afsluitend wordt er gespeculeerd over de toekomstige rol van multiparametrische algoritmes in zowel pre-klinisch als klinisch beroerteonderzoek. Hierbij biedt de op voxel gebaseerde integratie van een groot aantal (op MRI gebaseerde) biomarkers – die complexe en heterogene ziektemechanismen representeren – unieke kansen voor het differentiëren en volgen van heterogeen weefsel progressie zonder het definiëren van beperkende drempelwaardes voor levensvatbaarheid. Verdere ontwikkelingen, met inbegrip van ontwikkelingen van nieuwe op MRI gebaseerde biomarkers en nieuwe voorspellende algoritmen, bieden interessante perspectieven voor het verder uitbreiden van (pre-)klinische behandelstudies met deze multiparametrische methoden en wijzen in de richting van bijzondere mogelijkheden voor studies ter verbetering van gepersonalizeerde gezondheidszorg in de nabije toekomst.

Papers in international journals

Zijden van der JP, Bouts MJRJ, Wu O, Roeling TAP, Bleys RLAW, Toorn van der A, Dijkhuizen RM. (2008) Manganese-enhanced MRI of brain plasticity in relation to functional recovery after experimental stroke. *J Cereb Blood Flow Metab*. 28, 832-840.

Tiebosch IACW, Dijkhuizen RM, Cobelens, PM, Bouts MJRJ, Zwartbol R, Meide van der PH, Bergh van den W. (2012) Effect of interferon-β on neuroinflammation, brain injury and neurological outcome after experimental subarachnoid hemorrhage. *Neurocrit Care*. (epublish)

Tiebosch IACW, Crielaard BJ, Bouts MJRJ, Zwartbol R, Salas-Perdomo A, Lammers T, Planas AM, Storm G, Dijkhuizen RM. (2012) Combined treatment with recombinant tissue plasminogen activator and dexamethasone phosphate-containing liposomes improves neurological outcome and restricts lesion progression after embolic stroke in rats. *J Neurochem.* Nov;123 Suppl 2:65-7.

Bouts MJRJ, Tiebosch IACW, Toorn van der A, Viergever MA, Wu O, Dijkhuizen RM. (2013) Early identification of Potentially Salvageable Tissue with MRI-based Predictive Algorithms after Experimental Ischemic Stroke. *J Cereb Blood Flow Metab.* in press.

Tiebosch IACW, Bergh van den W, Bouts MJRJ, Zwarbol R, Toorn van der A, Dijkhuizen RM. (2013) Progression of brain lesions in relation to hyperperfusion from subacute to chronic stages after experimental subarachnoid hemorrhage: a multiparametric MRI study. *Cerebrovasc Dis.* in press.

Tiebosch IACW, Bouts MJRJ, Toorn van der A, Zwartbol R, Rijerkerk A, Vries de HE, Meide van der PH, Dijkhuizen RM. Interferon-β fails to prevent hemorrhagic transformation after thrombolytic treatment of experimental thromboembolic stroke. *submitted.*

Bouts MJRJ**,** Westmoreland SV, Crespigny de AJ, Liu Y, Vangel M, Dijkhuizen RM, Wu O, D'Arceuil HE. Distinct spatiotemporal patterns of changes after stroke in non-human primates using MRI-based cerebral tissue classification. *submitted.*

Bouts MJRJ, Tiebosch IACW, Rudrapadna U, Toorn van der A, Wu O, Dijkhuizen RM. Prediction of Post-stroke Hemorrhagic Transformation using MRI-based Algorithms. *submitted.*

Bouts MJRJ**,** Tiebosch IACW, Toorn, van der A., Hendrikse J, Wu O, Dijkhuizen RM. Lesion development and reperfusion benefit in relation to vascular occlusion patterns after embolic stroke in rats. *submitted.*

Abstracts in conference proceedings (first author only)

Bouts MJRJ, Wu O, Dijkhuizen RM, de Crespigny AJ, D'Arceuil HE (2009) Temporal Tissue Assessment in Non-Human Primate Cerebral Ischemia Using Diffusion-Weighted MR Imaging and ISODATA Cluster Analysis. *Proc Intl Soc Mag Reson Med,* (1499), Honolulu,HI, USA, April 18-24.

Bouts MJRJ, Zijden JP, Otte WM, Dijkhuizen RM (2009) Fuzzy clustering-based segmentation of manganese-enhanced neuronal network areas on MR images. *Proc Intl Soc Mag Reson Med*, (655), Honolulu, HI ,USA, April 18-24.

Bouts MJRJ, Tiebosch IACW, Zwartbol R, Wu O, Dijkhuizen RM. (2010) Effects of treatment on brain tissue classification with serial MRI-based ISODATA cluster analysis in an experimental subarachnoid hemorrhage model. *Proc Intl Soc Mag Reson Med*, (3132), Stockholm, Sweden, May 1-7.

Bouts MJRJ, Tiebosch IACW, Zwartbol R, Hoogveld E, Wu O, Dijkhuizen RM. (2011) Early prediction of salvageable tissue with multiparametric MRI-based algorithms after experimental ischemic stroke. *Proc Intl Soc Mag Reson Med,* (2141), Montreal, Canada, May 7-13.

Bouts, MJRJ, Tiebosch, IACW, van der Toorn A, Hendrikse J, Dijkhuizen RM (2012), Relationship between MRA-derived pattern of artery occlusion and MRI-based tissue diffusion and perfusion lesion in a rat embolic stroke model. *Proc Intl Soc Mag Reson Med*, (866), Melbourne, Australia, May 5-11.

Podium presentations

Bouts MJRJ, Zijden JP, Otte WM, Dijkhuizen RM (2009) Fuzzy clustering-based segmentation of manganese-enhanced neuronal network areas on MR images *Proc Intl Soc Mag Reson Med.* (655), Honolulu, HI ,USA, April 18-24.

Bouts MJRJ, Tiebosch IACW, Zwartbol R, Wu O, Dijkhuizen RM (2010) Effects of treatment on brain tissue classification with serial MRI-based ISODATA cluster analysis in an experimental subarachnoid hemorrhage model, *2nd Annual Intl Soc Mag Reson Med Benelux meeting*. (119), Utrecht, The Netherlands, January 18.

Bouts MJRJ, Tiebosch IACW, Zwartbol R, Hoogveld E, Wu O, Dijkhuizen RM. (2011) Early prediction of salvageable tissue with multiparametric MRI-based algorithms after experimental ischemic stroke, *3rd Annual Intl Soc Mag Reson Med Benelux meeting.* (33), Hoeven, The Netherlands, January 19.

Dankwoord

Het schrijven van een proefschrift is iets wat niet zomaar tot stand komt. Het is een gezamenlijke krachtsinspanning waarvoor ik een behoorlijk aantal mensen veel dank verschuldigd ben! Velen hebben bijgedragen aan de totstandkoming van dit proefschrift en ik ben hen ook zeer dankbaar, maar een aantal mensen wil ik in het bijzonder bedanken voor hun tomeloze inzet, kennis, ervaring, en vooral ook geduld!

Allereerst wil ik graag mijn co-promotor Dr. Rick Dijkhuizen bedanken. Beste Rick, ik ben blij dat jij mijn begeleider was. Ik vind het meer dan bewonderenswaardig hoe jij een druk gezinsleven, het begeleiden van een groot aantal PhD studenten, het schrijven van vele subsidies, en jouw passie voor sport feilloos weet te combineren. Je bleef altijd kritisch en zorgvuldig. Stukken die door mij werden geschreven werden steevast rood terug ontvangen, ook al had je sommige stukken zelf geschreven. Jouw doorzettingsvermogen en streven naar perfectie, wist je zelfs zover door te voeren dat je daarbij letterlijk de details niet meer kon zien. Maar ik ben er blij om, omdat ondanks dat je niet helemaal thuis was in de statistische modellen, toch iedere keer weer een studie naar een hoger niveau wist te tillen. Competitie heb jij tot een ware kunst verheven. Of het nou op het lab was, de UMC-estafette of in de kroeg jij wist overal een competitie-element in te vinden. Vooral het feit dat iemand met een lichtelijke smetvrees zonder na te denken een groot aantal bierviltjes van de bar verzameld om ze vervolgens in zijn mond te stoppen toont een echte sportersmentaliteit! Rick, bedankt voor het vertrouwen dat je me hebt gegeven, en mijn mentor wilde zijn. Ik heb heel veel geleerd en ik hoop in de toekomst nog vaak van jouw kennis en ervaring gebruik te mogen maken!
Ook mijn promotor, Prof. dr. ir. Viergever, wil ik bedanken. Beste Max**,** jij was degene die het aandurfde om mij aan te nemen. Of het nu ging om een referentie-brief, een korte vraag of een biannual progress meeting waarin dikwijls niet alleen de voortgang van mezelf werd besproken, ik kon altijd bij je aankloppen. Bedankt daarvoor!
I consider myself extra fortunate to have received such great support from abroad. Dear Ona, ever since Rick established our first meeting, I greatly valued your opinions, insights, and dedication to your work. It did not matter whether it was day or night you were always available for guidance and counseling even when it meant that you had to stay a few days longer after a conference! Thanks Ona! You can reserve my spot in the broom cupboard again as I'm looking forward to start working with you in Boston again!

Werk is niets zonder je directe lotgenoten. Dankzij jullie is het werken op het invivonmr-lab een onvergetelijk en uiteindelijk succesvol avontuur geworden. Met name wil ik bedanken:

Ivo (I-to-the-vo)! Als beeldverwerker ben je soms aangewezen op het gebruik van andermans data. Ondanks dat het soms moeilijk was een eenduidig verhaal uit de data te produceren, mocht ik mezelf gelukkig prijzen dat ik van jouw data gebruik mocht maken. Je stond altijd klaar voor een antwoord op een vraag, helpende hand, of een kort zangmomentje waarin steevast 'Moulin-Rouge' werd gepersifleerd. Bovenal jouw boekhoudige skills zouden een accountant niet misstaan. De administratie was altijd prima op orde en ik heb er dan ook vaak dankbaar gebruik van mogen maken. Verrassend blijft toch dat ik een aanzienlijk gedeelte van mijn tijd heb besteedt met het wachten op jouw steevast vertraagde reactie, maar dat ik op Hawaii toch wel moeite had om jou bij te benen. Ivo bedankt en ik hoop dat we nog vele avonden bouillon-fonduen in het verschiet zullen hebben!

Kalo Mahalo! Er zijn weinig mensen die ik zou willen typeren als een tovenaar, maar jij bent er een van. De snelheid en souplesse waarmee jij een toetsenbord hanteert is ongeëvenaard! Daarbovenop komen de vele hoogstaande scriptjes, programmaatjes en wetenschappelijke poëzie die binnen no-time op het beeldscherm staan. Ik vind het bijzonder knap dat iemand met geen directe scheikundige of biologische achtergrond zeer geavanceerde ontwikkelingsstudies op zulk hoog niveau weet uit te voeren. Verder was jij een van de weinige mensen, die mij met een (al dan niet spontane) borrel van mijn werkplek wist lost te weken om vervolgens al discussiërend tot nieuwe inzichten te komen die me bijzonder verder geholpen hebben in mijn onderzoek. Nu is het zaak om dat boekje af te ronden en snel een andere plek te zoeken, voordat je helemaal vastroest op de derde verdieping van het GDL!

Wim, mijn pogingen om jou bij te benen heb ik al snel gestaakt. Jouw tomeloze inzet, nieuwsgierigheid en snelheid waarop jij zeer complexe modelleringen meester maakt zijn ongekend. De moed zakte me soms in de schoenen wanneer ik bezig was met uitwerken van een model, waarvoor jij de volgende ochtend al een uitwerking klaar had. Ondanks dat we nooit een project echt samen gedaan hebben, heb ik veel aan je gehad. Ook je fantastische gevoel voor humor zorgde menig keer voor hilarische momenten. Al is het alleen maar omdat steeds wanneer er een belangrijke mail ontvangen wordt, er eerst gekeken wordt of deze niet toevallig door Chris Kleier gemaakt is. Ik hoop dat we in de nabije toekomst nog vaak samen met elkaar te maken zullen hebben.

Geralda, als deelgenoot van het hoekje met de grootste bureaus op de tweede verdieping hebben we menig uur besteed aan het behandelen van de lokale ergernissen, frustraties en roddels. Ideeën om van het hoekje een afgezonderd kantoor te maken zijn niet verder gekomen dan dat hoekje. Desalniettemin zal ik onze gesprekken gaan missen. Een troost kan ik je in ieder geval bieden vanaf nu kun je ongestoord genieten van je kopje thee met honing!

Lisette, of het nu een babbel, een luide aanvulling op je nies, of gewoon een met haar bezaaide stoel was, waar je ook was jouw aanwezigheid ging in ieder geval nooit onopgemerkt voorbij! Jouw eindeloos vertrouwen en geloof in een goede afloop was

jaloersmakend! Het waarderen en uitgebreid genieten van de micro-succesjes is iets wat je me toch een keertje moet leren. En het was terecht je hebt een mooi stukje werk afgeleverd. Succes met je nieuwe baan!

Umesh the mathematical wonder from India. You were always more than willing to help when my own skills were running short to solve the problem at hand. I really valued our discussions on whatever topic was available at that moment. Especially those Saturdays or Sundays when the lab was only occupied by us. I wish you all the best and hopefully I get the chance to ones again enjoy on of your delicious meals when we will meet across the Atlantic. I'm convinced you will finish your PhD with a 'boekje' that makes many jealous.

Pavel your unconventional working hours made sure that I did not have to spend my time alone when working overtime. Still I suspect that you are fully capable of speaking Dutch, but pretend you're not so that you can spy on us. All the best with finishing your PhD!

Wouter, onze directe samenwerking was niet omvangrijk, maar toch was het fijn om af en toe tegen iemand aan te lullen, je aan het werk te zetten of gewoon in de zeik te nemen. Ook ons avontuur op de klimwand zal ik niet snel vergeten, al is het alleen maar omdat ik vervolgens maandenlang in de lappenmand heb gelegen.

Peter, als wetenschapper ken ik weinig mensen die zo aanstekelijk enthousiast kunnen zijn over een nieuwbakken idee als jij. Het was altijd fijn om samen aan nieuwe ideeën te werken ook al vonden die helaas niet altijd hun weg naar het papier. Ook als 'Sven' wist je vaak genoeg voor memorabele momenten te zorgen.

Erwin, jouw rustige kijk op wetenschap deed me iedere keer weer beseffen dat er meer is dan werk alleen. Het bordje 'reservé' staat weer klaar voor de volgende conferentie waar we elkaar hopelijk aan de bar weer tegenkomen!

'Weet je wat het is' Gerard, jouw rustgevende wijze van probleemaanpak zorgde er meermaals voor dat we niet reddeloos verloren onze tijd aan het verdoen waren.

Ook jouw hulp, Annette, in het opzetten van de experimenten, het draaiende houden van de apparatuur, waren onontbeerlijk. Maar ook het organiseren van de 'baby-borrels' zijn meer dan gewaardeerd.

Maurits, het blijft ongelofelijk hoe jij dingen vanuit een bijna onmogelijke situatie voor elkaar krijgt. Of het nou op Hawaii is waar jij op een overvolle camping het beste plekje weet uit te zoeken om te kamperen (om er dan vervolgens niet te gaan slapen) of jouw kunst om steevast te laat te komen zonder dat iemand het echt onacceptabel vindt! Ik blijf het bewonderingswaardig vinden.

Jet, onze samenwerking betekende meteen ook mijn eerste publicatie, bedankt dat ik aan je project mocht meewerken om zo kennis te maken met beroerte-onderzoek.

Pim, als nieuwste collega heb je al aardig je draai weten te vinden in ons lab en mocht het toch allemaal niet lukken (wat me onwaarschijnlijk lijkt), ik zou je zo als acteur aannemen!

Verder wil ik natuurlijk niet mijn oud-collega's als Raoul, René, Kim, Steven, Arend en de vele andere studenten die ons lab hebben bezocht vergeten te bedanken. Maar ook de collega's buiten het lab of dat nu direct naast de deur is in het cardiolab zoals Eissa, Marcel, Kees, Sandra, Bernard, de overige medewerkers van het GDL of 'aan de overkant' bij het ISI. Mensen als Marjan, Renée, Jacqueline, Koen, Wilbert, Alexander, Bram, Josien, Jaco, Adriënne, Pieter, Marijn, Robin, Roel, Sjoerd V, Sjoerd v G, Job, Thessa, Harriët, Chantal, Hendrik, Gerrit, Vincent, Hugo, Mitko, Floris, Sascha, Yolanda, Miekee, Ewoud, Jeroen, Woutjan, Martijn, Sara, Maartje en de vele anderen (oud)-collega's bedankt voor de gesprekken over zinnige en onzinnige dingen al dan niet onder het genot van een heerlijk (soms zelfs zelfgebrouwen) biertje of kopje koffie!

Furthermore words of thanks to Susan, Helen, and Alex for their efforts in the monkey study. The many skype conference-calls were certainly not in vain! Ook Jeroen bedankt voor de overleggen en input over de toepassing van MRA in beroerte-voorspelling vanuit een klinisch perspectief! Ik vond het erg informatief en inspiratievol!

In de sporadische tijd dat ik in de buitenwereld kwam, zijn er gelukkig altijd mensen die zorgen voor de broodnodige afleiding. Natuurlijk ben ik veel dank verschuldigd aan mijn vrienden die ik vaak teleur heb moeten stellen met het feit dat ik weer eens zo nodig moest werken. In het bijzonder Erik, Walter en Erik Jan**.** Of het nu in het binnen- of in het buitenland was, de vele uren volleybal, discussies over sense en nonsens van allerlei dingen onder het genot van een (speciaal) biertje, wandelingen, stedentripjes, etc, ze vormden een welkome en zeer gewaardeerde afleiding! Ik hoop dan ook dat we dit nog vaak zullen herhalen!

Zonder familie ben je nergens! Bedankt voor jullie interesse en medeleven.
Vooral pap en mam! Bedankt dat jullie mij altijd ondersteund hebben. Ondanks dat ik soms andere paden bewandel dan jullie gehoopt hadden, zijn jullie er altijd en prijs ik me gelukkig met jullie onvoorwaardelijke steun! Ralf, Mandy en de kids het is fijn om te weten dat je altijd met open armen ontvangen wordt. Ralf, ook bedankt dat je mijn paranimf wil zijn! Oma, de rots in de branding! Maar bovenal Cindy**.** Het moet niet makkelijk zijn om mij als vriend te hebben. Maar jouw medeleven, steun, kritische kijk en vooral ook geduld zijn ongeëvenaard! Jij bent uniek in elk opzicht en dat maakt je zeer bijzonder! Het spijt me dat mijn ambities ons soms in de weg staan, maar ik weet zeker dat we samen een fanstastische tijd tegemoet gaan! Bedankt voor alles wat je voor me doet! En weet je, het boekje is nu echt af!

Mark

Curriculum vitae

Mark Bouts was born on January 13th, 1982 in Geleen. In 2000 he obtained his VWO Degree at the scholengemeenschap College Sittard (now Trevianum) in Sittard. He then studied Computer Science at the Hogeschool Zuyd in Heerlen. After obtaining his BSc. degree in 2004, he continued for his MSc. Degree at the 'Embedded Systems' programme the of the Technical University Eindhoven (TU/e). Yet after some period, he discovered that his interests were more with medical imaging. Therefore in 2005 he switched and continued his education at the 'Biomedical Image Sciences' programme of the Utrecht University. During this period he started his internship at the Biomedical Imaging and Spectroscopy group of the Image Sciences Institute / University Medical Center Utrecht. Under the supervision of Dr. Rick Dijkhuizen he worked on MRI-based segmentation of manganese accumulation in rat brain. During this internship he furthermore took the opportunity to gain research experience abroad and went to the Athinoula A. Martinos Center for Biomedical Imaging, Massachusetts General Hospital/ Massachusetts Institute of Technology/Harvard Medical School (Charlestown/Boston, MA, USA) to work 5 months as a research trainee under the supervision of Dr. Ona Wu. In 2008 he obtained his MSc Degree and continued to work in the group of Dr. Dijkhuizen as a PhD candidate. In this period he worked on MRI-based predictive algorithms, predicting tissue outcome after cerebral stroke, from which the results are described in this thesis. As of summer 2013 he will start as a research fellow at the Athinoula A. Martinos Center for Biomedical Imaging, Massachusetts General Hospital/ Massachusetts Institute of Technology/Harvard Medical School (Charlestown/Boston, MA, USA) under the supervision of Dr. Ona Wu.